공학박사 학위논문

Energy Conversion of Visible Light and Interfacial Charge Transfer Processes on Semiconductor-Based Photocatalytic Nanomaterials

반도체 기반 광촉매 나노물질을 이용한 가시광 에너지 전환 및 계면에서의 전하전달과정

2016 년 2 월

서울대학교 대학원

화학생물공학부

유 성 주

Abstract

Energy Conversion of Visible Light and Interfacial Charge Transfer Processes on Semiconductor-Based Photocatalytic Nanomaterials

Sungju Yu

School of Chemical and Biological Engineering

The Graduate School

Seoul National University

The broad energy distribution of solar spectrum is one of the intrinsic factors limiting the efficiency of photocatalytic systems. Artificial photosynthesis using a Z-schematic mechanism of green plants is regarded as one of the most attractive technologies for efficiently converting energy of visible light into other energy sources. An all-solid-state Z-schematic system, $Au@CdS/TiO_{1.96}C_{0.04}$, has been reported for the efficient H_2 generation from water under visible-light irradiation. However, the vectorial charge-carrier flow at the interface was not fully investigated from the standpoint of kinetics and mechanism. In this study, spectroscopic tools were developed for interrogating their properties. Electron pathways were constructed on the basis of steady-state photoluminescence (PL) spectral data, and the rate constants for charge transfer were calculated from time-resolved PL spectra. The PL results revealed that Au core played an important role in capturing the photoexcited electrons in the conduction band (CB) of $TiO_{1.96}C_{0.04}$ and

accelerating the electron transfer to the valence band (VB) of CdS, leading to an efficient quenching of the holes left in the VB of CdS shell. The minimum energy pathways for H_2 production on the surfaces of $TiO_{1.96}C_{0.04}$(101) and CdS(101) were elucidated through first-principle calculations, indicating that the CdS shell has a lower energy barrier (2.81 eV) for the surface reaction than that (3.34 eV) of $TiO_{1.96}C_{0.04}$. Consequently, Au@CdS/$TiO_{1.96}C_{0.04}$ showed a vectorial electron transfer of $TiO_{1.96}C_{0.04}$ → Au → CdS in the form of the letter Z, which allowed the photoexcited electrons to be shuttled to a higher energy level, thereby producing substantial level of H_2 on the CdS(101) surface.

Interestingly, although the Z-schematic system generates photoexited electrons with thermodynamically strong redox characteristics, the core-shell nanomaterial produces little photocurrent in photoelectronchemical (PEC) system as compared to the amount of H_2 generataion. The reason for low photocurrent can be understood from the results of the previous fundamental research. The photoexcited electrons accumulated in the CB of CdS shell have to reach the indium-tin oxide (ITO) circuit for photocurrent generation. However, there is no any pathway to allow the electrons to be transferred to the ITO circuit. Therefore, a significant fraction of the electrons are recombined at the interparticles. Perovskite $SrTiO_3$ nanoparticles (NPs) were used as a high performance electron filter instead of the PS II material, $TiO_{1.96}C_{0.04}$, thereby entirely reversing the Z-schematic charge transfer direction. The nanocomposte enabled the efficient production of H_2 as well as electron harvest within a range of visible light. The findings showed that the ultrafast decay of hot electrons across Au nanoparticles can be significantly reduced by strong coupling with CdS quantum dots and by a Schottky junction with perovskite $SrTiO_3$ nanoparticles. The designed plasmonic nanostructure created a hot-electron-assisted energy cascade for the favorable electron pathway involving CdS → Au → $SrTiO_3$, as demonstrated through

steady-state and time-resolved PL spectroscopies. This results provide a new approach for overcoming the low efficiency typically associated with plasmonic nanostructures.

Of the light energy delivered by the sun to the surface of the earth, ~95% is in the visible and infrared region. However, it is difficult to utilize a significant fraction of solar photons with wavelengths longer than 500 nm for working photocatalysts and photovoltaics. This is because the photon energy is not sufficiently potent to activate desired reactions through electronic excitation processes of semiconductors or molecules. The loss of this otherwise-wasted portion of sunlight can be ameliorated by shifting two or more low-energy photons into higher-energy ones. This novel process, which is referred to as photon upconversion showing an anti-Stokes type emission, is known to one of the promising routes for amplifying frequencies of sub-band-gap light ($E < E_g$). Here I show a fluorescence resonance energy transfer (FRET)-assisted upconversion process across three components for efficiently utilizing sub-band-gap light. In the process, a highly luminescent rhodamine B (RhB) makes a FRET pair with naked carbon nanodots (NC-dots) of 3.4 nm, which are not passivated by any insulating molecules but show excitation-wavelength dependent upconversion behavior. The FRET effect enhances the upconverted light intensity of NC-dots. These upconverted photons are subsequently used to sensitize Ag_3PO_4 particles and thus generate 18 times higher photocurrent at $\lambda_{ex} > 500$ nm than before adding the RhB molecules. The reason for increase in photocurrent is fundamentally unveiled by steady-state and time-resolved PL spectroscopies. The findings provide a new approach for the utilization of light energy in the visible and infrared region.

Keywords: solar energy conversion, photocatalysis, nanomaterials, visible light, electron transfer, hydrogen
Student Number: 2010-24097

Contents

List of Tables

List of Figures

Chapter 1. Introduction

1.1 Hydrogen Economy

The use of fossil fuels in the modern industrial development has raised severe energy and environmental issues all over the world. The combustion of carbon-based energy sources produces around 21.3 billion tonnes of CO_2 per year. It is estimated that about half of the evolved CO_2 are eliminated by natural processes. As a result, there is a net increase of 10.65 billion tonnes of atmospheric CO_2 per year [1]. Anthropogenic CO_2 is one of the primary greenhouse gases that contributes to global warming, and causes climate change and serious destruction in ecosystem. A global movement towards the development of renewable energy resources is therefore actively under way to reduce the emission of greenhouse gases.

Hydrogen, H_2 is a potential alternative to fossil fuels for achieving a sustainable society because it has the highest energy content per unit of weight of any other fuels and is known to be the cleanest energy source among others. Moreover, H_2 fuel can be conveniently converted into electricity through fuel cell system, and then the electricity is used as a motive power to work a multitude of electronics and vehicles. However, it is mainly extracted from hydrocarbons by steam reforming in the same way as a car engine (**Figure 1.1**) [2]. Although the reforming process achieves about 90% efficiency for H_2 production, the produced H_2 has a lower energy content than

the original fuel. In addition, the detour process ironically emits the greenhouse gases such as CO and CO_2 during H_2 generation.

Green H_2 fuel can be produced from water using zero emission renewable energy sources. In fact, the sun delivers about 121,800 terawatts of light energy to Earth's surface (**Figure 1.2**) [3]. The total solar energy absorbed by Earth's atmosphere, oceans and land masses for one hour is more than consumed energy in all the world for a whole year. This outstanding potential of solar power has made great strides to convert the solar energy into chemical and electronical energies. One of the most promising solutions to energy and environmental crises is artificial photosynthesis, which is inspired by the photosynthetic apparatus of plants [4–8]. The artificial photosynthesis technology for H_2 generation from water can lead to next generation energy system through a hybid with fuel cells, subsequently reducing carbon emissions and dependency on fossil fuels.

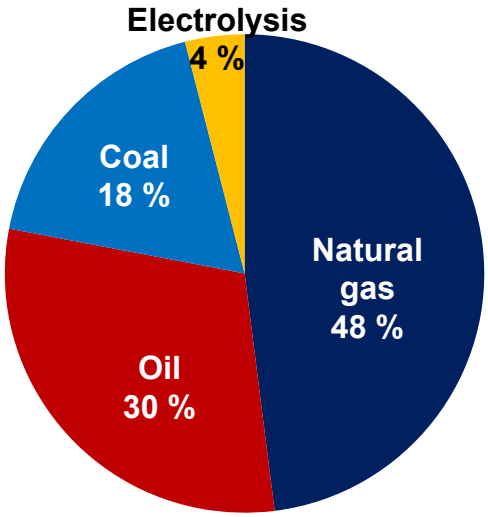

Figure 1.1 H_2 production from different sources.

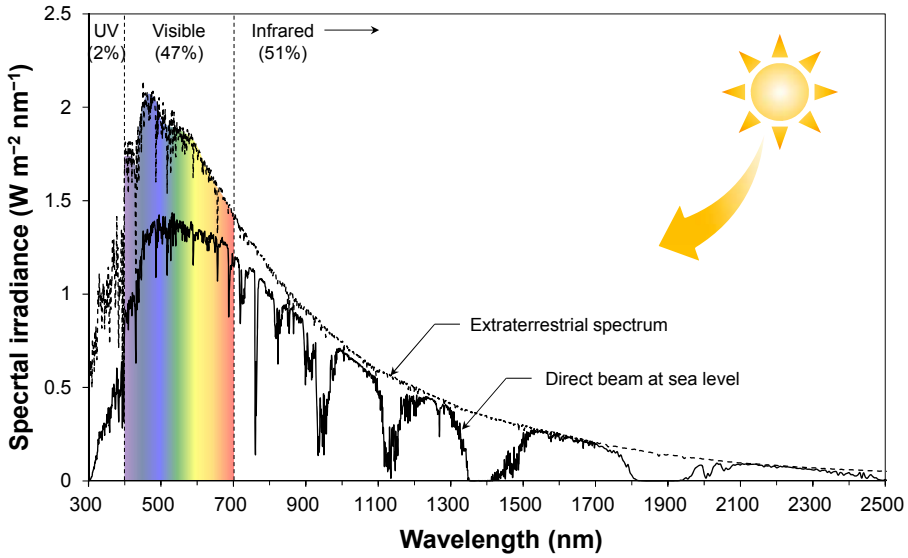

Figure 1.2 Solar spectrum above atmosphere and at surface.

1.2 Basic Principles of Artificial Photosynthesis

In light-dependent reaction, green plants ultimately reduce the $NADP^+$ and H^+ to NADPH, and oxidize H_2O to O_2, H^+, and electrons through Z-schematic process, which entails a two-step photoexcitation in the light-harvesting antenna complexes (**Figure 1.3**). The electrons in the highest occupied molecular orbital (HOMO) of photosystem (PS) II are excited to its lowest unoccupied molecular orbital (LUMO) upon absorbing photons. The photoexcited electrons in LUMO of PS II are then shuttled to HOMO of PS I through an electron transport chain. The electrons are excited to its LUMO once more as soon as they arrived at HOMO of PS I, and subsequently are used for reduction reaction. The holes left in the HOMO of PS II are consumed by oxidizing H_2O. Therefore, the holes and electrons accumulated at the PS I and PS II have a thermodynamically high potential to oxidize and reduce, respectively.

For efficiently mimicking the natural photosynthesis, there are several points to be duly considered as follows: (1) Photocatalytic materials should have a narrow bandgap energy (1.23 eV < E_g < 3.0 eV) enough to utilize abundant visible light, (2) The CB position of the materials should be more negative than a reduction potential of an oxidant, and VB position must be more positive than an oxidation potential of a reductant, (3) Photoexcited electron–hole pairs should be efficiently separated in order to suppress charge recombination. Renewable H_2 can be produced from artificial photosynthesis technique without any carbon emission (**Figure 1.4**). Furthermore, high value-

added products can be also synthesized by coupling of the carbon-free H_2 and other areas of catalysis. For example, hydrogenation of CO_2 with clean H_2 produces methanol for use as a fuel and a stockfeed in a wide range of petrochemical area [9]. For these reasons, artificial photosynthesis plays a crucial role in a sustainable society for future generations. The quantum efficiency (QE) of photosynthetic systems, which is important to practical utilization depends on the photon absorption and the recombination rate of electron–hole pairs. The handicap of wide-bandgap semiconductors have been overcome by use of the incident photons via chemical modifications [10–13] and metal/non-metal-ion doping [14–19]. The wide-bandgap can be further offset by anchoring a photosensitizer such as narrow-bandgap quantum dots [20–22] or dye molecules [23] onto the host semiconductor. The losses of electron–hole pairs are suppressed by a variety of approaches, including deposition of co-catalysts [24,25], the formation of a heterojunction structure [26,27]. Nanostructuring the photoactive materials can also reduce the travel distance of electron and holes before reaching active sites on its surface [28,29]. Since the issue of charge transfer across the semiconductor interface is a key factor in enhancing photocatalytic activity, kinetic and mechanistic insights into the charge transfer processes are essential and important for a fundamental understanding of such a system and the practical applications of artificial photosynthesis.

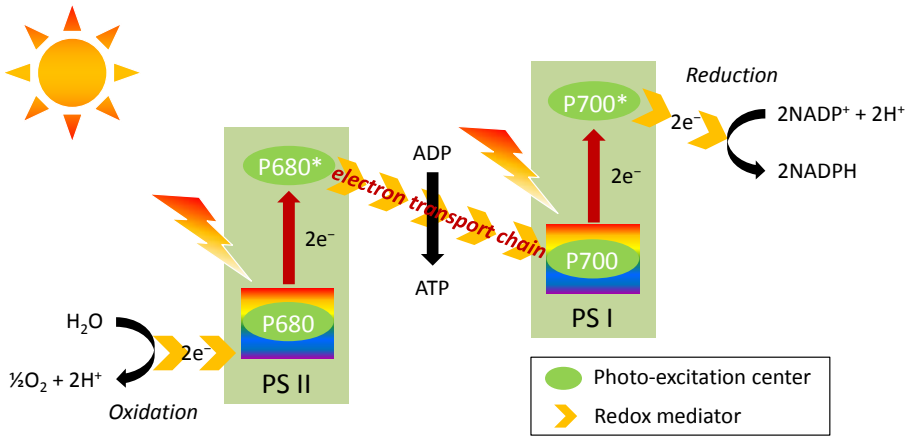

Figure 1.3 Natural process of photosynthesis in green plants: Z-scheme.

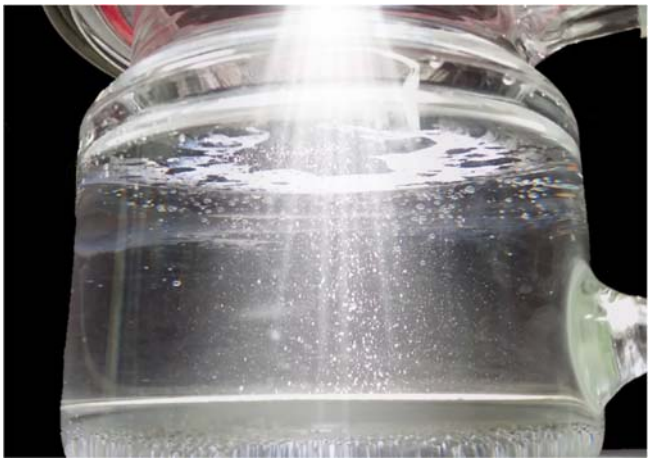

Figure 1.4 A photograph taken during the photocatalytic H_2 generation from water.

1.3 Objectives

This research is focused on the basic science and engineering of electron/energy-transfer phenomena occurred at the surface and interface of nanoparticles for the efficient energy conversion of visible light. First, a visible-light-responsive photocatalyst is designed by mimicking the natural photosynthesis for the photocatalytic H_2 generation. In particular, spectroscopic tools are developed for interrogating their properties and Z-schematic electron transfer. Based on the fundamental understanding, the Z-schematic charge-transfer direction are entirely reversed in order to efficiently generate H_2 as well as photocurrent. The designed nanostructure with three distinct components enables a hot-electron-assisted energy cascade for electron transfer, thereby efficiently reducing the ultrafast decay of the hot electrons. The charge transfer process and kinetics are demonstrated by steady-state and time-resolved PL spectroscopies. Finally, frequencies of a significantly wasted portion of the sunlight are amplified through FRET-assisted upconversion process. The reason for increase in photocurrent is also unveiled by using spectroscopic tools. Consequently, the photocatalytic nanomaterials and the various charge transfer processes introduced in this thesis will be informative for the design of photocatalysts as well as of photoelectrochemical devices, such as photovoltaics and water-splitting devices.

Chapter 2. Kinetic and Mechanistic Insights into the All-Solid-State Z-Schematic System

2.1 Introduction

Hydrogen, H_2, is a potential alternative to fossil fuels for achieving a sustainable society. Approximately 95% of emission-free H_2 has been being produced by steam-methane reforming process which involves the side production of carbon dioxide and carbon monoxide, ironically contributing to global warming [2]. One of the most promising technologies for environmentally producing carbon-free H_2 is artificial photosynthesis mimicking the natural process of photosynthesis as follows [4–8]. The electrons in the VB of PS II are excited to its CB under irradiation by solar light. The photoexcited electrons are transferred to the VB of PS I through an electron mediator where the transferred electrons recombine with the holes left in the VB of PS I. The photoexcited electrons and holes accumulate in the CB of PS I and the VB of PS II, respectively. Consequently, they have thermodynamically strong redox characteristics to allow solar light to be efficiently converted into chemical energy. This charge-transfer mechanism is so-called Z-scheme.

I recently reported that two visible-light responsive photocatalysts, $TiO_{1.96}C_{0.04}$ and CdS, when combined with Au nanoparticles, generate H_2 from water via the artificial Z-scheme mechanism [8]. The photocatalytic

system utilized the CdS and $TiO_{1.96}C_{0.04}$ as the components of PS I and PS II in green plants, respectively. Au nanoparticles acted as an electron mediator between $TiO_{1.96}C_{0.04}$ and CdS. The Au@CdS/$TiO_{1.96}C_{0.04}$ system achieved the efficient H_2 production when irradiated with visible light. However, the vectorial charge-carrier flow at the interface was not fully investigated from the standpoint of kinetics and mechanism. It is noteworthy that only a few kinetic and mechanistic studies have been conducted with the goal of comprehending the complex charge-transfer processes in semiconductor-metal-semiconductor systems [30]. In particular, since the issue of charge transfer across the semiconductor interface is a key factor in enhancing photocatalytic activity, kinetic and mechanistic insights into an all-solid-state Z-schematic system are essential and important for a fundamental understanding of such a system and the practical applications of artificial photosynthesis.

In this study, the Z-schematic charge-transfer kinetics of Au@CdS/$TiO_{1.96}C_{0.04}$ was demonstrated by measuring the decay time of an indicator dye through steady-state PL and time-resolved PL spectroscopy, one of the ultrafast laser techniques that are used to probe interfacial charge-transfer in photocatalysis [31−35]. Electron pathways were constructed on the basis of the results of steady-state PL spectroscopy, so as to understand kinetics of the charge-transfer processes. Differential equations were derived for use as an effective tool for modelling and understanding the target system. Finally, the rate constants for interfacial charge transfer were calculated by correlating the transport model equation with the kinetic parameters extracted

from time-resolved PL spectra. Furthermore, the minimum energy pathways for associative desorption of H_2 on the surfaces of $TiO_{1.96}C_{0.04}$(101) and CdS(101) were elucidated through the climbing image-nudged elastic band (CI-NEB) method.

2.2 Experimental

2.2.1 Preparation of Au@CdS/$TiO_{1.96}C_{0.04}$ Nanostructure

$TiO_{1.96}C_{0.04}$ nanoparticles were prepared by a gel-hydrothermal method. A 60 mL aliquot of titanium isopropoxide (≥ 99%, Samchun) was completely mixed with 54 mL of anhydrous triethanolamine (≥ 98%, Sigma-Aldrich), and 286 mL of deionized (DI) water was then added to the mixture. A 30 mL aliquot of aqueous solution of oleic acid (0.02 M, Samchun) was then mixed with the 30 mL of the prepared solution. The pH of the resulting solution was controlled to pH 8 by the dropwise addition of dilute nitric acid (≥ 60%, Samchun). The resulting mixture was placed in a Teflon-lined autoclave and heated at 100 °C for 12 h to form a $Ti(OH)_4$ gel, which was then heated at 250 °C for 48 h. The resulting brown precipitate was isolated by centrifugation, washed several times with DI water, and then dried at 60 °C overnight. The organic residue remaining on the surface of the $TiO_{1.96}C_{0.04}$ nanoparticles was completely removed by annealing at 320 °C for 8 h under an atmosphere of air. Anatase TiO_2 nanoparticles were prepared by the procedure described above, except that a calcination temperature of 450 °C was used. Au nanoparticles were deposited on the surface of the $TiO_{1.96}C_{0.04}$ by direct reduction. $TiO_{1.96}C_{0.04}$ powder (1.0 g), was dispersed in 200 mL of DI water. $HAuCl_4 \cdot 4H_2O$ (≥ 99.9%, Sigma-Aldrich) was then added to the suspension, resulting in the deposition of 2 wt% Au nanoparticles. After stirring for 30 min, 30 mL of an aqueous solution of $NaBH_4$ (0.02 M) was

slowly added to the aqueous suspension. A purple-colored Au/$TiO_{1.96}C_{0.04}$ powder was obtained after stirring for 3 h and isolated by centrifugation. A Au@CdS core-shell was formed by the photoexcitation of the $TiO_{1.96}C_{0.04}$. Sulfur (2 mmol) and $Cd(ClO_4)_2 \cdot 6H_2O$ (8 mmol) were added to 200 mL of an ethanol suspension containing Au/$TiO_{1.96}C_{0.04}$ nanoparticles. The suspension was exposed to UV light for 12 h using a Xe arc lamp (300 W, Oriel) as the light source. Finally, a dark green Au@CdS/$TiO_{1.96}C_{0.04}$ powder was obtained by centrifugation, which was washed several times with DI water, and dried at 60 °C overnight. The CdS content was determined to be 4 wt% by ICP-AES. A heterojunction CdS/$TiO_{1.96}C_{0.04}$ was prepared by an ion-exchange method. $Cd(ClO_4)_2 \cdot 6H_2O$ was added to a $TiO_{1.96}C_{0.04}$ suspension, resulting in the deposition of 4 wt% CdS. After stirring for 30 min, 20 mL of an aqueous solution of Na_2S (0.02 M) was slowly added to the suspension. A yellow CdS/$TiO_{1.96}C_{0.04}$ powder was obtained after stirring for 3 h, which was isolated by centrifugation.

2.2.2 Catalyst Characterization

The morphology and 2D elemental mapping of the product were investigated by high-angle annular dark-field scanning transmission electron microscopy (HAADF-STEM, JEM-2100F, 200 kV) equipped with the energy dispersive spectroscopy (EDS). The microstructures were examined by X-ray diffraction (XRD, D/max-2500/PC, Rigaku) with Cu Kα radiation (λ = 0.154 nm) as the incident beam at 50 kV and 100 mA. Optical absorbance spectra

were obtained by ultraviolet-visible diffuse reflectance spectroscopy (UV-DRS, V670-Jasco) with $BaSO_4$ as a reference. O 1s spectra of bare TiO_2 and $TiO_{1.96}C_{0.04}$ nanoparticles were obtained by X-ray photoelectron spectroscopy (XPS, Thermo) where the binding energy was corrected with reference to the C 1s peak of 284.5 eV for each sample. The amount of Au or CdS in the prepared samples was determined by inductively coupled plasma-atomic emission spectroscopy (ICP-AES, ICPS-7500, Shimadzu).

2.2.3 Photoluminescence Spectroscopies

The steady-state PL was measured with a PerkinElmer LS55 spectrophotometer (PerkinElmer Ltd., Beaconsfield, UK) equipped with a Xe lamp. The measurements were replicated a total of three times and average values were reported. Time-resolved PL spectra were obtained using a time-correlated single photon counting (TCSPC) setup (FluoTime 200, Picoquant GmbH) with a PicoHarp 300. The excitation source was a 405 nm pulsed diode laser (LDH-P-C-405, Picoquant GmbH) with a repetition rate up to 80 MHz. The signals were collected at the excitonic emission of rhodamine B (RhB, Sigma, for fluorescence, λ_{em} = 580 nm). The temperature was maintained at 20 °C by circulating water through an external temperature controlled device during the TRPL measurements. The measured data from the PicoHarp 300 were analyzed by the FluorFit software.

2.2.4 Computational Details

Density functional theory (DFT) calculations were carried out with the Vienna ab initio simulation package (VASP) [36], using the generalized gradient approximation Perdew-Burke-Ernzerhof (GGA-PBE) exchange-correlation functional [37]. Projector augmented wave (PAW) method as implemented in the VASP was employed [38]. Plane-wave cutoff energy of 400 eV was used for the calculations including CdS and $TiO_{1.96}C_{0.04}$. A 3 × 3 × 1 Monkhorst-Pack *k*-point mesh was used to sample the Brillouin zone. All the structural optimizations were performed until the atomic forces were less than 0.03 eV $Å^{-1}$. The electronic self-consistent field tolerance was set to 1×10^{-4} eV. Based on the anatase TiO_2 ($I4_1/amd$, JCPDS 21-1272) with 24 Ti atoms and 48 O atoms in a 10.45 × 7.72 × 20.00 $Å^3$ supercell, $TiO_{1.96}C_{0.04}$(101) slab was modeled at which one O atom on the surface was substituted with C atom according to the experimental results that lattice oxygen of anatase TiO_2 was successfully replaced by carbon dopant (**Figure 2.1a**). CdS slab was constructed by cutting the bulk greenockite structure ($P6_3mc$, JCPDS 41-1049) for (101) surface to be exposed, based on the experimental crystallographic results in this study. The constructed slab contained total 54 atoms, which consists of 27 atoms for each Cd and S in a 11.83 × 12.41 × 18.08 $Å^3$ supercell (**Figure 2.1b**). The angle between two basal plane vectors which are perpendicular to *z*-axis is about 105°. The surface of each slab was allowed to be relaxed, and the supercells included the vacuum layer which is thick enough to prevent the slab-slab interactions. The CI-NEB method was used to find the minimum energy paths for associative desorption of hydrogen [39,40].

Structural optimizations of initial and final states were performed after systematically screening the possible adsorption states. To set a series of images for the NEB calculation, three images were introduced by linear interpolation of initial and final states with a few modifications to prevent improbable paths. In the following step, partial optimization was performed at the edge of energy barrier to see if another energy barrier emerges. In the NEB calculations, the optimization continued until the maximum atomic forces became less than 0.06 eV $Å^{-1}$.

2.2.5 Photocatalytic Activities

Photocatalytic H_2 production was performed in a gas-closed top window (quartz glass) Pyrex cell with 0.15 g of photocatalyst suspended in 100 mL aqueous solution of 0.05 M Na_2S and 0.1 M Na_2SO_3. The reaction cell was irradiated with a 300 W Xe lamp (Oriel) combined with a 420 nm cut-off filter. The reaction temperature was maintained by circulating a coolant connected to a water-jacketed reservoir at 15 °C. The amount of produced H_2 was quantified by online gas chromatography (Acme6100-Young Lin) using a thermal conductivity detector (TCD).

2.3 Results and Discussion

2.3.1. Catalyst Characterization

The preparation of a visible-light-responsive photocatalyst to mimic the natural photosynthesis was previously reported [8]. The photocatalytic system was composed of three components, Au@CdS core-shell on the $TiO_{1.96}C_{0.04}$. Briefly, the $TiO_{1.96}C_{0.04}$ nanoparticles synthesized by a gel-hydrothermal method in the presence of oleic acid as a carbon source. Au nanoparticles were deposited on the surface of the $TiO_{1.96}C_{0.04}$ by the direct reduction of $AuCl_4^-$ anions to Au^0 using $NaBH_4$ as the reducing agent. A CdS shell was selectively formed around the Au core by the photodeposition of an ethanol suspension containing Au/$TiO_{1.96}C_{0.04}$, sulphur molecules, and Cd^{2+} cations. **Figure 2.2a** shows a HAADF-STEM image of the as-prepared Au@CdS/$TiO_{1.96}C_{0.04}$ nanoparticles, in which the thickness of the CdS shells was in the range of 4 to 5 nm around the Au cores with diameter of 4 to 6 nm. **Figures 2.2b−d** display the results of 2D atomic mapping obtained for a selected area in the inset of **Figure 2.2a**, which confirms that a Au@CdS core-shell was successfully formed on the surface of $TiO_{1.96}C_{0.04}$. The HR-TEM image shown in **Figure 2.2e** clearly reveals two distinct types of lattice fringes, which are assigned to $TiO_{1.96}C_{0.04}$(101) and CdS(101).

The fact that carbon was substitutionally incorporated by replacing lattice oxygen in the TiO_2 framework was determined by XRD, TPO, XANES, and EXAFS in the previous study [41]. Furthermore, **Figure 2.3a** shows that the

carbon dopant has a direct influence on the binding energy (BE) of the O 1s of TiO_2. Peak 1 centered at 529.7 eV is assigned to regular lattice oxygen, and the BE was maintained, even after carbon doping. Peaks 2 and 3 correspond to carbonate in the TiO_2, which is from carbon contamination and adsorbed molecular H_2O as the sample is exposed to air [42,43]. The two peaks were slightly shifted to lower BE due to the formation of oxygen vacancies [42,43]. The BE shift also verified that the carbon dopants were successfully incorporated into the TiO_2 framework. The crystalline structure of the prepared samples was confirmed from XRD patterns (**Figure 2.3b**). $TiO_{1.96}C_{0.04}$ nanoparticles had an anatase structure in the absence of any other crystalline phase created by the carbon dopants. A typical diffraction peak corresponding to Au nanoparticles was not observed due to its low concentration (2 wt%), as well as the relatively strong diffraction intensity of the anatase structure. Wurtzite diffraction peaks (dotted lines) of 4 wt% CdS were weakly observed in XRD patterns of Au@CdS/$TiO_{1.96}C_{0.04}$. Notably, the strongest characteristic peaks of $TiO_{1.96}C_{0.04}$ and CdS represented that they mainly exposed (101) surfaces on the each nanoparticles. The absorbance of each sample was characterized by UV-DRS (**Figure 2.3c**). One shoulder in area 1 was attributed to $TiO_{1.96}C_{0.04}$, and the other shoulder in area 2 corresponded to the presence of CdS shells. In particular, Au@CdS/$TiO_{1.96}C_{0.04}$ nanostructure produced a broad peak centered at 600 nm due to the surface plasmon of the Au cores. The plasmon band showed a broadening and red shift of 55 nm as compared to Au/$TiO_{1.96}C_{0.04}$, suggesting that the Au core and the CdS shell are involved in strong electronic

interactions [35,44]. Photocatalytic H_2 production was performed at a wavelength longer than 420 nm (**Figure 2.3d**). The photocatalytic activity of Au@CdS/$TiO_{1.96}C_{0.04}$ was compared with that of bare $TiO_{1.96}C_{0.04}$ and CdS-sensitized $TiO_{1.96}C_{0.04}$ (CdS/$TiO_{1.96}C_{0.04}$) in which all of the samples contained almost the same concentrations of Au and CdS, as determined by ICP-AES. As the particle size and interfacial properties of CdS play a critical role in the photocatalytic actitivy [45−47], CdS/$TiO_{1.96}C_{0.04}$ heterostructure was carefully prepared by slowly adding the dilute Na_2S solution into the aqueous suspension of $TiO_{1.96}C_{0.04}$ and Cd^{2+} cations for high dispersion of CdS nanoparticles. **Figure 2.4** shows the morphology and size of CdS nanoparticles dispersed on the $TiO_{1.96}C_{0.04}$. Although the CdS nanoparticles were slightly aggregated on a portion of $TiO_{1.96}C_{0.04}$ surface, they have a uniform size of 5−8 nm and spherical shape. The bare $TiO_{1.96}C_{0.04}$ nanoparticles generated negligible amounts of H_2 gas due to the rapid charge recombination of the single photocatalyst and relatively low CB minimum (−0.1 V vs NHE) [48]. The CdS/$TiO_{1.96}C_{0.04}$ photocatalyst produced 1.2 μmol h^{-1} of H_2, and the H_2 production resulted from the enhanced charge separation with the formation of a heterojunction structure. The charge separation in the heterojunction structures has been studied by various researchers [49−51]. Since both the CB minimum (−1.0 V vs NHE) and VB maximum (+1.3 V vs NHE) of CdS are located at more negative potentials than the CB minimum (−0.1 V vs NHE) and VB maximum (+2.5 V vs NHE) of $TiO_{1.96}C_{0.04}$ [27,48], the photoexcited electrons in the CB of the CdS can transfer to the CB of the $TiO_{1.96}C_{0.04}$ whereas the photoexcited holes in the VB of $TiO_{1.96}C_{0.04}$ can

migrate to the VB of CdS. Interestingly, the Au@CdS/$TiO_{1.96}C_{0.04}$ photocatalyst produced 6 times more H_2 (7.5 μmol h^{-1}) than the CdS/$TiO_{1.96}C_{0.04}$. This is the result of vectorial charge transfer induced by the simultaneous excitation of $TiO_{1.96}C_{0.04}$ and CdS with the participation of Au as an electron mediator. Furthermore, the charge carriers of Au@CdS/$TiO_{1.96}C_{0.04}$ nanostructure flow in the reverse direction of the charge transfer in the case of CdS/$TiO_{1.96}C_{0.04}$ heterojunction structure. That is, the photoexcited electrons and holes tend to accumulate in the CB of CdS and the VB of $TiO_{1.96}C_{0.04}$, respectively. It is thermodynamically plausible that H_2 is produced more easily on the surface of CdS via the Z-schematic electron-transfer pathway compared to the electron-transfer pathway of heterojunction. However, the kinetic and mechanistic aspects of such a junction type are not fully understood.

2.3.2. Surface-Reaction Energetics

I carried out DFT calculations to find minimum energy pathways for associative desorption of H_2 using the NEB method. Firstly, the DFT method used in this study was compared with the representative literature about the hydrogen interaction with the anatase TiO_2(101) surface. As shown in **Figure 2.5**, the calculated H_2 desorption energy (1.49 eV) on the anatase TiO_2(101) agrees well with the one, 1.39 eV, previously reported by A. Selloni et al. [52]. **Figure 2.6a** indicates the calculated reaction pathways for H_2 production on the surfaces of CdS(101) and $TiO_{1.96}C_{0.04}$(101), and the

corresponding snapshots are shown in **Figures 2.6b,c**. The reaction processes for H_2 generation were composed of following three steps: (1) Two isolated hydrogen atoms gradually became close through the inter-atomic hopping on the surface, and this atomic migration step did not affect the activation barrier during the entire reaction. (2) The neighboring hydrogen atoms combined to form a H_2 molecule when they were close enough to interact, and this molecularization step was largely endothermic. (3) The formed H_2 molecule was rearranged to settle into the most stable adsorption state, and this molecular migration step required a small amount of energy. I also compared the energy barriers for H_2 production on the CdS(101) and $TiO_{1.96}C_{0.04}$(101). The energy barriers for the H_2 desorption on CdS(101) and $TiO_{1.96}C_{0.04}$(101) were 2.81 eV and 3.34 eV, respectively. The energy difference between the maximum state and the final state represents the energy required for the rearrangement of hydrogen atoms. These energy differences were 0.09 eV and 0.31 eV on CdS(101) and $TiO_{1.96}C_{0.04}$(101). It should be noted that a H_2 molecule on CdS(101) needed little energy for the rearrangement during the molecular migration. Consequently, the energy difference before and after the associative desorption of H_2 can be the energy requirement for H_2 production on the CdS(101). The required energy on the $TiO_{1.96}C_{0.04}$(101) was higher than that on CdS(101), indicating that the $TiO_{1.96}C_{0.04}$(101) needed more energy for H_2 production than CdS(101) during the molecularization step. These results explain that H_2 molecules prefer being formed on the CdS surface by Z-schematic charge transfer

rather than on the $TiO_{1.96}C_{0.04}$ surface by heterojunction assisted charge transfer.

2.3.3 Electron-Transfer Kinetics

Steady-state and time-resolved PL measurements were carried out in order to investigate the charge-transfer processes of Au@CdS/$TiO_{1.96}C_{0.04}$ nanostructure. In these experiments, 1 μM RhB was used as a tracer dye, in order to observe the charge transfer at the solid-state interface. The photoexcited electrons of RhB can be transferred to the CB of $TiO_{1.96}C_{0.04}$ and CdS shell, leading to a quenching of the PL emission of RhB because the LUMO potential (−1.1 V vs NHE) of RhB is higher than the CB minimum of $TiO_{1.96}C_{0.04}$ and CdS [35]. **Figure 2.7a** shows the steady-state PL spectra of aqueous solutions of RhB in the presence of $TiO_{1.96}C_{0.04}$, Au/$TiO_{1.96}C_{0.04}$, CdS/$TiO_{1.96}C_{0.04}$, Au@CdS/$TiO_{1.96}C_{0.04}$, and CdS as a function of emission wavelength with excitation at 405 nm. The spectra exhibited a peak emission at 580 nm, which is assigned to a radiative recombination of RhB and a weak emission for $TiO_{1.96}C_{0.04}$. The CdS has no PL emission at the excitation wavelength (**Figure 2.7b**). The colloidal $TiO_{1.96}C_{0.04}$ in the RhB solution caused a depression in the peak emission of RhB due to the charge transfer from the excited RhB to the CB of $TiO_{1.96}C_{0.04}$ nanoparticles. However, the PL intensity in the range of 500 to 550 nm was higher than that of pure RhB. This can be attributed to the PL emission of $TiO_{1.96}C_{0.04}$, which originates from the oxygen vacancies associated with Ti^{3+} in anatase TiO_2 [53,54]. The PL

emission of RhB was obviously quenched after the Au nanoparticles had been deposited on the surface of $TiO_{1.96}C_{0.04}$, indicating that the photoexcited electrons of RhB were transferred to the CB of $TiO_{1.96}C_{0.04}$ as well as to the Fermi level of the Au nanoparticles. Furthermore, since the Au nanoparticles absorb at a wavelength of 580 nm, $Au/TiO_{1.96}C_{0.04}$ in the absence of RhB could quench up to 50% of the PL emission of $TiO_{1.96}C_{0.04}$. The deposition of CdS on the surface of $TiO_{1.96}C_{0.04}$ resulted in a measurable suppression of the PL intensity of RhB, and, in the absence of RhB, $CdS/TiO_{1.96}C_{0.04}$ depressed the PL emission of $TiO_{1.96}C_{0.04}$ due to the enhanced charge separation caused by the heterojunction structure. The PL depression of RhB by $CdS/TiO_{1.96}C_{0.04}$ was superior to that for $Au/TiO_{1.96}C_{0.04}$ at an excitation wavelength of 405 nm, since the CdS was strongly excited at this excitation wavelength. The PL emission of CdS in the absence of RhB can be seen in **Figures 2.8a**. The CdS hardly emits PL regardless of the excitation wavelength. Therefore, the PL emission of RhB cannot be enhanced by the PL emission of CdS. The colloidal CdS in RhB solution caused a depression in the peak emission of RhB due to the charge transfer from the excited RhB to the CB of CdS nanoparticles as shown in **Figures 2.8b**. Furthermore, an obvious depression in the PL intensity of RhB was noted with a deposition of CdS nanoparticles on the surface of $TiO_{1.96}C_{0.04}$ when the excitation wavelength was shorter than 480 nm. The depression was due to the strong excitation of CdS, which facilitated a charge transfer from the CB of CdS to the CB of $TiO_{1.96}C_{0.04}$. As a result, the photoexcited electrons of RhB were transferred to the CB of CdS faster than to Au nanoparticles of $Au/TiO_{1.96}C_{0.04}$ at the excitation wavelength

(λ_{ex} < 480 nm). However, the PL depression of RhB by Au/$TiO_{1.96}C_{0.04}$ was superior to the CdS/$TiO_{1.96}C_{0.04}$ at the excitation wavelength (λ_{ex} > 480 nm) due to the localized surface plasmon resonance of the Au nanoparticles. This phenomenon was also observed in the CdS suspended in RhB solution. Although the CdS showed an excellent depression at the excitation wavelength (λ_{ex} < 480 nm), the PL depression of RhB by the weak excitation of CdS was inferior to that for Au/$TiO_{1.96}C_{0.04}$ at the excitation wavelength (λ_{ex} > 480 nm). Notably, the PL quenching of RhB by Au@CdS/$TiO_{1.96}C_{0.04}$ was more pronounced than that of Au/$TiO_{1.96}C_{0.04}$ and CdS/$TiO_{1.96}C_{0.04}$ at the excitation wavelength. This enhanced quenching was due to the simultaneous excitation of $TiO_{1.96}C_{0.04}$ and CdS shell in the presence of a Au core. The large work function of the Au core permits the excited electrons in the CB of $TiO_{1.96}C_{0.04}$ to be captured and then quickly delivers the electrons to the VB of the CdS shell, thereby resulting in an improved charge separation. In the absence of RhB, the quenched PL emission of $TiO_{1.96}C_{0.04}$ by Au@CdS/$TiO_{1.96}C_{0.04}$ is greater than that by Au/$TiO_{1.96}C_{0.04}$ and CdS/$TiO_{1.96}C_{0.04}$ over the entire range of the emission wavelength.

Time-resolved PL measurements were performed to further investigate the interfacial charge-transfer kinetics of the Au@CdS/$TiO_{1.96}C_{0.04}$ nanostructure where 405 nm laser pulses were used to excite the RhB with $TiO_{1.96}C_{0.04}$ and CdS. PL decay traces were collected at a wavelength of 580 nm which consists of the peak emission for RhB and the weak emission for $TiO_{1.96}C_{0.04}$. **Figure 2.9** shows the time-resolved PL spectra of the RhB in the presence of $TiO_{1.96}C_{0.04}$, Au/$TiO_{1.96}C_{0.04}$, CdS/$TiO_{1.96}C_{0.04}$, Au@CdS/$TiO_{1.96}C_{0.04}$, and CdS.

The resulting fluorescence was fitted to the following multi-exponential model where the intensity is assumed to be the sum of the individual single exponential decays [55],

$$I(t) = \sum_{i=1}^{n} A_i e^{-t/\tau_i} \quad (2\text{-}1)$$

in this expression A_i and τ_i indicate the amplitude and the decay time of the i component, respectively, and n is the number of individual fluorescence. As shown in **Figure 2.10**, decay pathways of the excited electrons in the the LUMO of RhB and the CB of $TiO_{1.96}C_{0.04}$ were constructed in an attempt to understand the kinetics of the process, based on steady-state PL spectroscopy data. The arrows representing the excitation processes of $TiO_{1.96}C_{0.04}$ and CdS were omitted in the charge-transfer models. In the schematic processes, R, T, A, and C denote RhB, $TiO_{1.96}C_{0.04}$, Au, and CdS, respectively. $N_R(t)$ and $N_T(t)$ refer to the time-dependent electron populations in the the LUMO of RhB and the CB of $TiO_{1.96}C_{0.04}$, respectively. All of the fitted parameters are summarized in **Table 2-1**. The value of χ^2 was used to judge the goodness-of-fit. Since the CdS has no PL emission at the excitation wavelength, the intensity decay of pure RhB and the RhB in the presence of CdS was found to be a single exponential function (n = 1). However, the decay traces for RhB containing $TiO_{1.96}C_{0.04}$ could be fit to a bi-exponential function (n = 2) since both RhB and $TiO_{1.96}C_{0.04}$ showed the PL emission at 580 nm. The obtained time-resolved PL spectra can be the sum of PL_R (PL of RhB) and PL_T (PL of $TiO_{1.96}C_{0.04}$). Therefore, the pre-exponential factors A_i can be considered to be the relative contributions of PL_R and PL_S to the obtained time-resolved PL

spectra. Furthermore, τ_1 in the first exponential term and τ_2 in the second exponential term describe the decay times of N_R and N_T, respectively. Here, differential equations were developed as a charge-transfer model to calculate the rate constants, and these equations are summarized in **Table 2.2**. The rate constants in each case were calculated by comparing the exponents of the developed differential equations developed as a charge-transfer model with τ_i extracted from the fitted results of time-resolved PL spectra, and the resulting constants are summarized in **Table 2.3**. For example, the recombination rate constant of pure RhB, k_R, was expressed by a reciprocal of τ_1 (1.696 ns), and its value was found to be approximately 5.90×10^8 s^{-1} [11,35]. The RhB in the presence of $TiO_{1.96}C_{0.04}$ displayed a component of τ_1 (1.683 ns) and τ_2 (6.876 ns). The short decay time can be a reciprocal of $k_R + k_{R\rightarrow T}$ where $k_{R\rightarrow T}$ was a rate constant for the interfacial charge transfer from the LUMO of RhB to the CB of $TiO_{1.96}C_{0.04}$, since the τ_1 was assigned to the decay of the N_R. Therefore, the value of $k_{R\rightarrow T}$ can be calculated by subtracting a reciprocal of τ_1 (1.683 ns) and k_R, and the resulting rate constant was found to be 0.04×10^8 s^{-1}. The long decay time was responsible for the dynamic quenching of $TiO_{1.96}C_{0.04}$. The recombination rate constant for $TiO_{1.96}C_{0.04}$, k_T, was represented by a reciprocal of τ_2 (6.876 ns). It was estimated to be 1.45×10^8 s^{-1}. The fluorescence decay of RhB in the presence of $TiO_{1.96}C_{0.04}$ was enhanced greater by depositing Au nanoparticles on the $TiO_{1.96}C_{0.04}$, since the photoexcited electrons of RhB were transferred to the CB of $TiO_{1.96}C_{0.04}$ as well as to the Fermi level of Au nanoparticles, $k_{R\rightarrow A}$ (0.04×10^8 s^{-1}). Furthermore, the deposition of Au nanoparticles on the surface of $TiO_{1.96}C_{0.04}$

causes the excited electrons in the CB of $TiO_{1.96}C_{0.04}$ to be entrapped in the Fermi level of Au. This rate constant, $k_{T\rightarrow A}$, was found to be 0.93×10^8 s^{-1}. An obvious depression in the PL intensity of RhB was noted with a deposition of CdS nanoparticles on the surface of $TiO_{1.96}C_{0.04}$ since the photoexcited electrons of RhB transfer to the CB of $TiO_{1.96}C_{0.04}$ and CdS. The excited electrons in the CB of CdS are assumed to be sequentially transferred to the CB of $TiO_{1.96}C_{0.04}$ since CdS emitted only negligible PL. Its corresponding rate constant was denoted by $k_{R\rightarrow C\rightarrow T}$ (0.21×10^8 s^{-1}), which was faster than the $k_{R\rightarrow T}$ (0.04×10^8 s^{-1}) and the electron transfer from the LUMO of RhB to the CB of CdS, $k_{R\rightarrow C}$ (0.06×10^8 s^{-1}) due to the heterojunction of $TiO_{1.96}C_{0.04}$ and CdS. The decay of excited electrons in the CB of $TiO_{1.96}C_{0.04}$ to the VB of CdS showed a rate constant, $k_{T\rightarrow C}$, of 1.24×10^8 s^{-1}. When the Au@CdS/$TiO_{1.96}C_{0.04}$ nanostructure was suspended in RhB, the photoexcited electrons of RhB were transferred to the CB of the CdS shell as well as $TiO_{1.96}C_{0.04}$. Because the Au core interacts strongly with the CdS shell, the electrons which were transferred from the excited RhB to the CB of CdS shell tended to be injected into the Fermi level of Au core. The electrons injected into Au core can be recombined with the existing holes in the VB of CdS shell where the rate constant, $k_{R\rightarrow C\rightarrow A\rightarrow C}$, was determined to be 0.33×10^8 s^{-1}. The other electrons, transferred from the excited RhB to the CB of $TiO_{1.96}C_{0.04}$, were injected into the Au core. The injected electrons are likely to decay to the VB of CdS shell, whose rate constant, $k_{T\rightarrow A\rightarrow C}$, was 3.03×10^8 s^{-1}. This process showed the fastest electron transfer, leading to an efficient quenching of the holes left in the VB of CdS shell. The calculation result that the $k_{T\rightarrow A\rightarrow C}$

was much faster than the $k_{R\rightarrow C\rightarrow A\rightarrow C}$ verifies the Z-schematic charge transfer of Au@CdS/$TiO_{1.96}C_{0.04}$. Furthermore, the presence of a Au core in the Au@CdS/$TiO_{1.96}C_{0.04}$ nanostructure remarkably facilitated the interfacial charge transfer of $TiO_{1.96}C_{0.04}$ and CdS as compared to CdS/$TiO_{1.96}C_{0.04}$. These observations explain why the Z-schematic charge transfer of Au@CdS/$TiO_{1.96}C_{0.04}$ results in a high level of H_2 production in the visible-light region, as evidenced by the kinetics of the process.

2.4 Conclusion

Z-schematic charge-transfer kinetics at the solid-state interface of Au@CdS/$TiO_{1.96}C_{0.04}$ was demonstrated through the steady-state and time-resolved PL spectroscopies using the RhB as a tracer dye. The electron-transfer processes of photocatalysts were constructed on the basis of the steady-state PL specta. The rate constants for electron transfer were obtained by correlating the kinetic parameters extracted from the time-resolved PL spectra using the developed differential equations. The PL results revealed that the presence of a Au core, sandwiched between the $TiO_{1.96}C_{0.04}$ and the CdS shell, enabled the excited electrons to be flowed in the reverse direction of the charge-transfer of CdS/$TiO_{1.96}C_{0.04}$ heterojunction structure and also accelerated the interfacial charge transfer from $TiO_{1.96}C_{0.04}$ to CdS shell. As a result, the holes left in the VB of CdS were efficiently quenched by the electrons injected from the CB of $TiO_{1.96}C_{0.04}$ through the Au core, contributing to the accumulation of electrons in the CB of CdS shell. The electrons, arrived in the excited state of CdS shell by Z-scheme, possess a strong reducing power due to the high CB minimum (−1.0 V vs NHE) and quickly react with H^+ adsorbed at the surface due to the lower energy barrier for the H_2 production as compared to the $TiO_{1.96}C_{0.04}$ surface, thereby enhancing H_2 production in the range of visible light. This study provides an explanation for why the Z-scheme mechanism of Au@CdS/$TiO_{1.96}C_{0.04}$ is superior to the heterojunction mechanism of CdS/$TiO_{1.96}C_{0.04}$ for H_2 production.

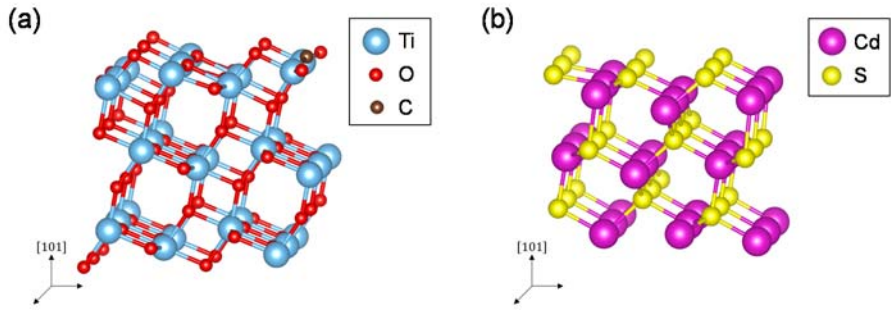

Figure 2.1 (a) $TiO_{1.96}C_{0.04}$(101) slab with 24 Ti atoms and 48 O atoms in a 10.45 × 7.72 × 20.00 $Å^3$ supercell, and (b) CdS(101) slab with 27 Cd atoms and 27 S atoms in a 11.83 × 12.41 × 18.08 $Å^3$ supercell for DFT calculations.

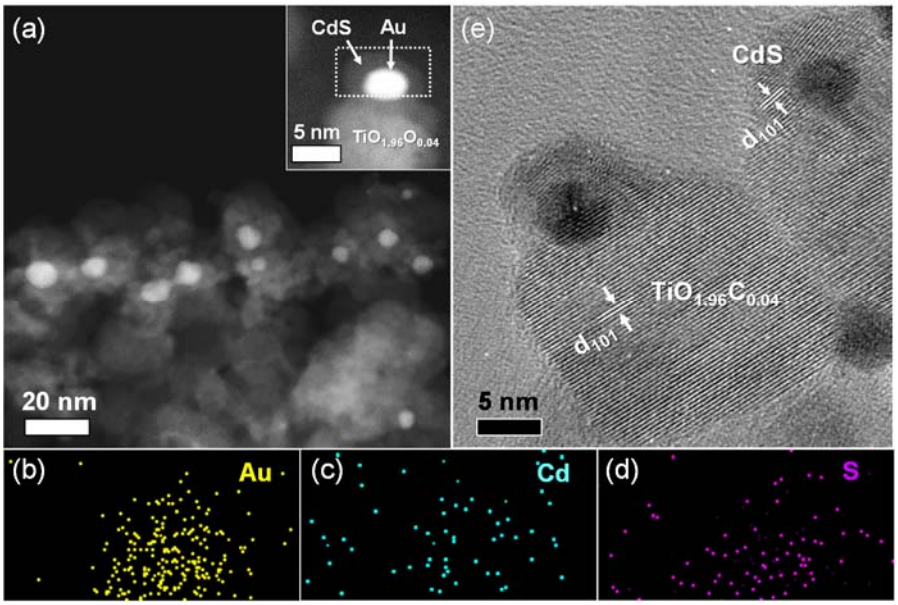

Figure 2.2 Morphology and composition of a Au@CdS/$TiO_{1.96}C_{0.04}$ nanocomposite using microscopy techniques. (a) HAADF-STEM image of the Au@CdS core-shell distributed on the surface of $TiO_{1.96}C_{0.04}$ nanoparticle at which inset shows the area selected for the STEM-EDS analysis. (b−d) 2D atomic mapping of the core-shell structure selected in the inset of (a); Au, Cd, and S. (e) HR-TEM image showing the lattice fringes of the $TiO_{1.96}C_{0.04}$(101) and CdS(101) planes.

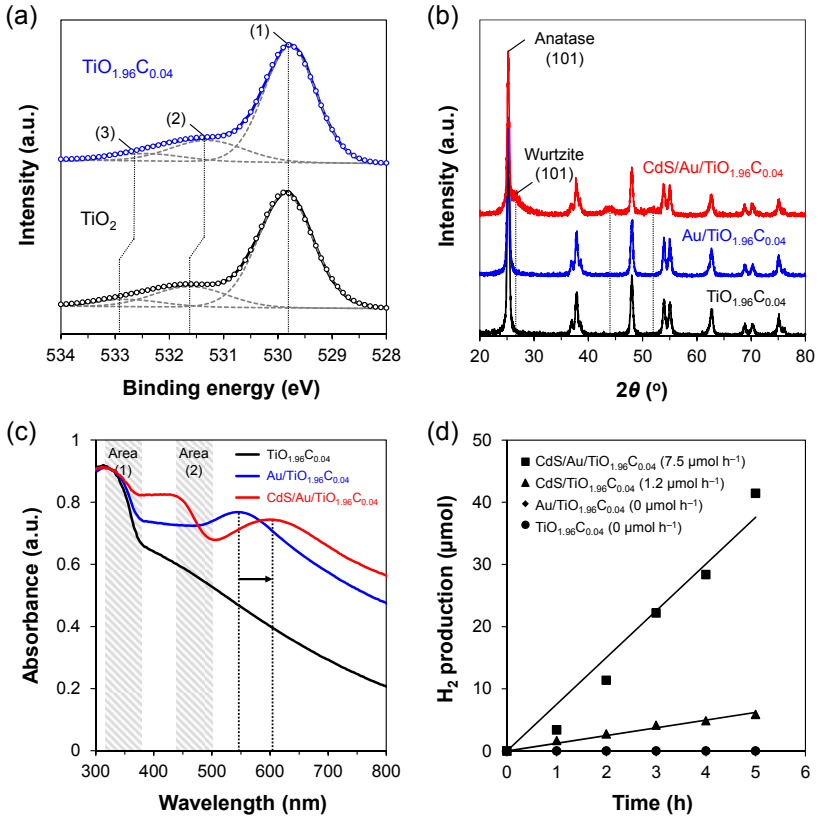

Figure 2.3 (a) O 1s XPS spectra of bare TiO_2 and $TiO_{1.96}C_{0.04}$ where peak 1 was attributed to the regular lattice oxygen and peak 2 and 3 correspond to carbonate in the TiO_2. (b) XRD patterns of $TiO_{1.96}C_{0.04}$, $Au/TiO_{1.96}C_{0.04}$, $Au@CdS/TiO_{1.96}C_{0.04}$ nanocomposites where the vertical dotted lines indicated the crystalline structure of wurtzite-structured CdS. (c) UV-vis absorbance spectra of the prepared samples where two shoulders in area 1 and area 2 were ascribed to the $TiO_{1.96}C_{0.04}$ and CdS, respectively. The vertical dotted line represented a plasmon band of Au nanoparticles. (d) Photocatalytic H_2 production as a function of time under visible-light irradiation ($\lambda \geq 420$ nm).

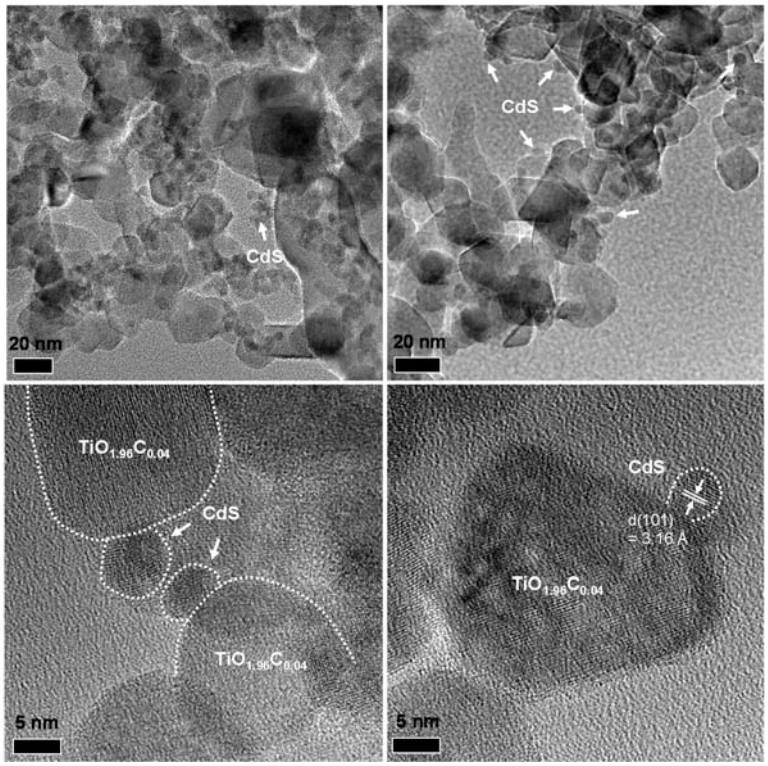

Figure 2.4 TEM images of CdS/$TiO_{1.96}C_{0.04}$ heterostructure.

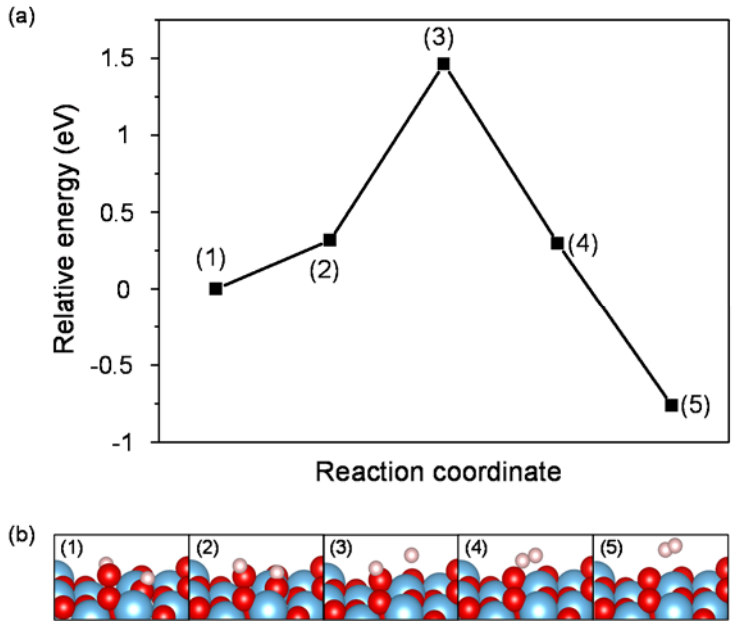

Figure 2.5 (a) DFT calculations of the minimum energy path for H_2 production on the anatase TiO_2(101) slab with 24 Ti atoms and 48 O atoms in a 10.45 × 7.72 × 20.00 $Å^3$ supercell. (b) The corresponding snapshots in the each step where ivory small spheres show the atomic hydrogen; sky-blue and red spheres represent Ti and O atoms, respectively. DFT calculations revealed a high energy barrier (3.34 eV) for the H_2 desorption over the anatase $TiO_{1.96}C_{0.04}$(101) as compared to that (1.49 eV) of the anatase TiO_2(101). Carbon doping into TiO_2 framework may have negative effect on the water splitting activity due to the defect induced band-structure changes [56]. In this study, O 1s XPS spectra showed that the carbon dopants formed the oxygen vacancies in the TiO_2 lattice.

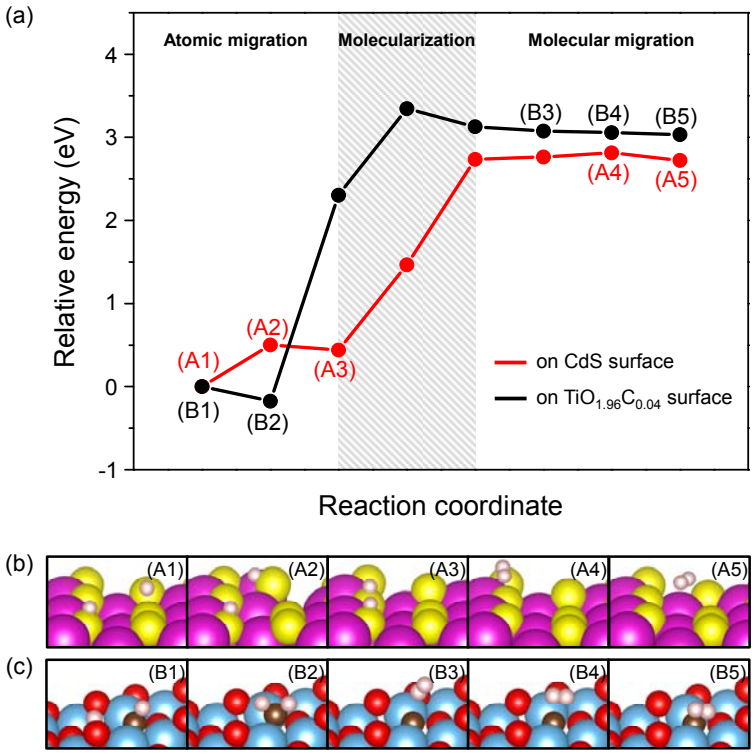

Figure 2.6 (a) DFT-calculated most favorable reaction pathways for H_2 production on the CdS(101) and $TiO_{1.96}C_{0.04}$(101). The corresponding snapshots in the each step on the (b) CdS(101) and (c) $TiO_{1.96}C_{0.04}$(101) where ivory small spheres show the atomic hydrogen; puplish red and yellow spheres represent Cd and S atoms; sky-blue, red, and dark brown spheres represent Ti, O, and C atoms, respectively.

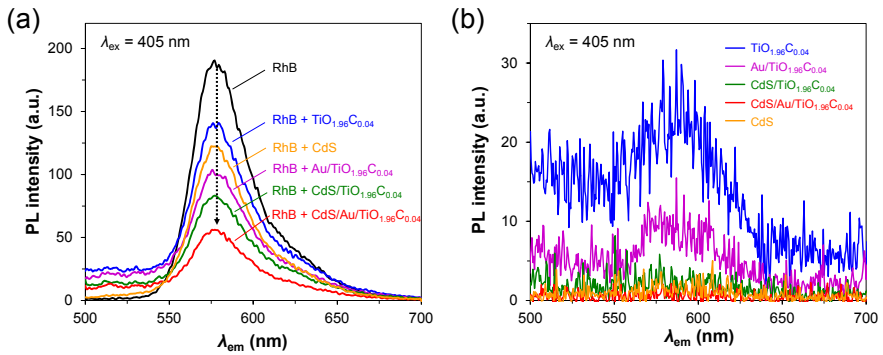

Figure 2.7 Steady-state PL spectra of (a) 1 μM RhB aqueous solutions in the presence of each sample and (b) the prepared samples in the absence of RhB solution as a function of the emission wavelength, λ_{em}, where the excitation wavelength, λ_{ex}, is 405 nm.

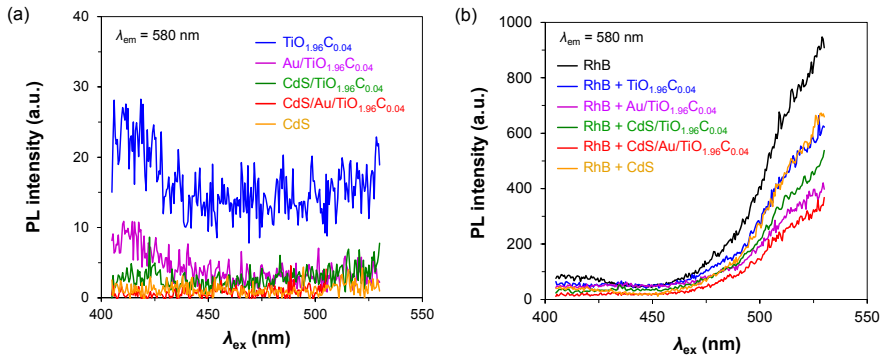

Figure 2.8 Steady-state PL spectra of (a) the prepared samples in the absence of RhB solution and (b) an aqueous solution of 1 μM RhB in the presence of each sample as a function of excitation wavelength, λ_{ex}, where the emission wavelength, λ_{em}, is 580 nm.

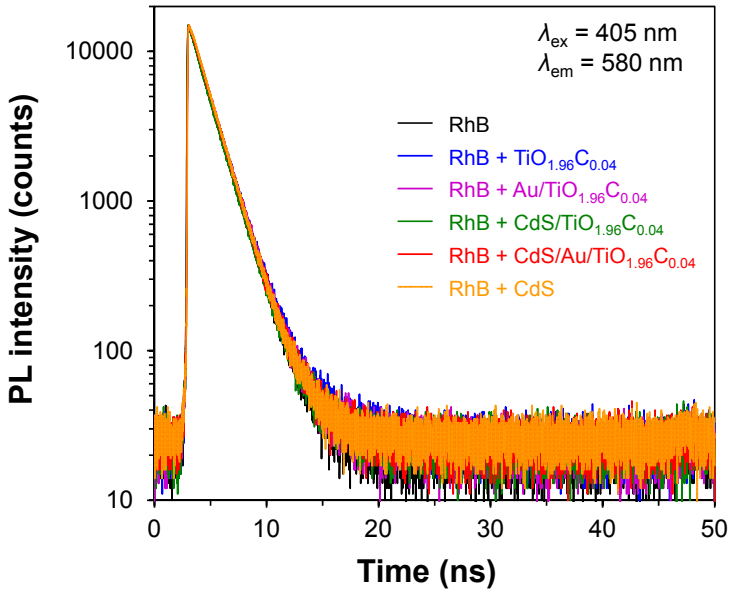

Figure 2.9 Time-resolved PL spectra of 1 μM RhB in the presence of each sample with 405 nm excitation where the emission wavelength is 580 nm.

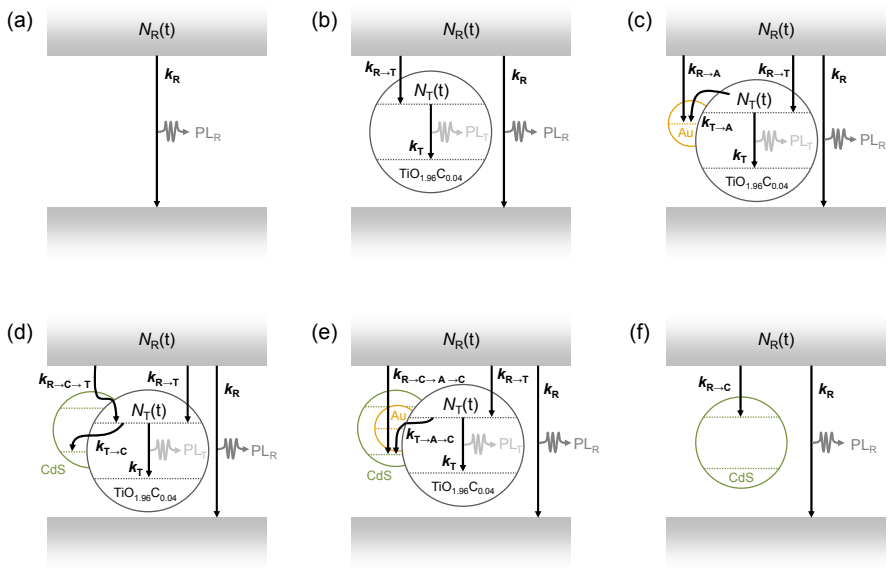

Figure 2.10 Decay pathways of the excited electrons in the the LUMO of RhB and the CB of $TiO_{1.96}C_{0.04}$ when the excitation wavelength is 405 nm. The RhB solution contains (a) none, (b) $TiO_{1.96}C_{0.04}$, (c) Au/$TiO_{1.96}C_{0.04}$, (d) CdS/$TiO_{1.96}C_{0.04}$, (e) Au@CdS/$TiO_{1.96}C_{0.04}$, and (f) CdS where R, T, A, and C denote RhB, $TiO_{1.96}C_{0.04}$, Au, and CdS, respectively. $N_R(t)$ and $N_T(t)$ refer to the time-dependent electron populations in the LUMO of RhB and the CB of $TiO_{1.96}C_{0.04}$, respectively. k represents the rate constant for the charge transfer or charge recombination corresponding to its subscript. The arrows representing the excitation processes of $TiO_{1.96}C_{0.04}$ and CdS were omitted in the charge transfer models.

Table 2.1 Kinetic parameters extracted from the fitted results of time-resolved PL spectra of 1 μM RhB in the presence of each sample with excitation at 405 nm.[a]

Entry	A_1	τ_1 (ns)	A_2	τ_2 (ns)	χ^2
RhB	13426.2	1.696	-	-	1.000
RhB + $TiO_{1.96}C_{0.04}$	12194.5	1.683	69.4	6.876	1.006
RhB + Au/$TiO_{1.96}C_{0.04}$	13184.8	1.671	135.9	4.209	1.028
RhB + CdS/$TiO_{1.96}C_{0.04}$	12198.7	1.625	230.3	3.717	1.043
RhB + Au@CdS/$TiO_{1.96}C_{0.04}$	10717.6	1.596	1626.6	2.231	1.007
RhB + CdS	12542.1	1.678	-	-	1.003

[a] The parameters were calculated using the FluoFit software program.

Table 2.2 Charge-transfer models of each entry when the excitation wavelength is 405 nm.

Entry	Balance equations for $N_R(t)$	Balance equations for $N_T(t)$
RhB (see Figure 2.10a)	$\frac{dN_R}{dt} = -k_R N_R$ $N_R = N_{R0} e^{-k_R t}$	-
RhB + $TiO_{1.96}C_{0.04}$ (see Figure 2.10b)	$\frac{dN_R}{dt} = -(k_R + k_{R\to T}) N_R$ $N_R = N_{R0} e^{-(k_R + k_{R\to T})t}$	$\frac{dN_T}{dt} = k_{R\to T} N_R - k_T N_T$ $N_T = C_1 e^{-(k_R + k_{R\to T})t} + C_2 e^{-k_T t}$ [a]
RhB + Au/$TiO_{1.96}C_{0.04}$ (see Figure 2.10c)	$\frac{dN_R}{dt} = -(k_R + k_{R\to T} + k_{R\to A}) N_R$ $N_R = N_{R0} e^{-(k_R + k_{R\to T} + k_{R\to A})t}$	$\frac{dN_T}{dt} = k_{R\to T} N_R - (k_T + k_{T\to A}) N_T$ $N_T = C_3 e^{-(k_R + k_{R\to T} + k_{R\to A})t} + C_4 e^{-(k_T + k_{T\to A})t}$ [b]
RhB + CdS/$TiO_{1.96}C_{0.04}$ (see Figure 2.10d)	$\frac{dN_R}{dt} = -(k_R + k_{R\to T} + k_{R\to C\to T}) N_R$ $N_R = N_{R0} e^{-(k_R + k_{R\to T} + k_{R\to C\to T})t}$	$\frac{dN_T}{dt} = (k_{R\to T} + k_{R\to C\to T}) N_R - (k_T + k_{T\to C}) N_T$ $N_T = C_5 e^{-(k_R + k_{R\to T} + k_{R\to C\to T})t} + C_6 e^{-(k_T + k_{T\to C})t}$ [c]
RhB + Au@CdS/$TiO_{1.96}C_{0.04}$ (see Figure 2.10e)	$\frac{dN_R}{dt} = -(k_R + k_{R\to T} + k_{R\to C\to A}) N_R$ $N_R = N_{R0} e^{-(k_R + k_{R\to T} + k_{R\to C\to A})t}$	$\frac{dN_T}{dt} = k_{R\to T} N_R - (k_T + k_{T\to A\to C}) N_T$ $N_T = C_7 e^{-(k_R + k_{R\to T} + k_{R\to C\to A})t} + C_8 e^{-(k_T + k_{T\to A\to C})t}$ [d]
RhB + CdS (see Figure 2.10f)	$\frac{dN_R}{dt} = -(k_R + k_{R\to C}) N_R$ $N_R = N_{R0} e^{-(k_R + k_{R\to C})t}$	-

[a] $C_1 = \frac{k_{R\to T}}{k_T - (k_R + k_{R\to T})} \cdot N_{R0}$ and $C_2 = N_{T0} - C_1$ where N_{R0} and N_{T0} is constant.

[b] $C_3 = \frac{k_{R\to T}}{(k_T + k_{T\to A}) - (k_R + k_{R\to T} + k_{R\to A})} \cdot N_{R0}$ and $C_4 = N_{T0} - C_3$

[c] $C_5 = \frac{k_{R\to T} + k_{R\to C\to T}}{(k_T + k_{T\to C}) - (k_R + k_{R\to T} + k_{R\to C\to T})} \cdot N_{R0}$ and $C_6 = N_{T0} - C_5$

[d] $C_7 = \frac{k_{R\to T}}{(k_T + k_{T\to A\to C}) - (k_R + k_{R\to T} + k_{R\to C\to A})} \cdot N_{R0}$ and $C_8 = N_{T0} - C_7$

Table 2.3 Calculated rate constants for an excitation wavelength of 405 nm.

Entry	Rate constants ($\times 10^8$ s^{-1})
k_R	5.90
$k_{R\rightarrow T}$	0.04
$k_{R\rightarrow A}$	0.04
$k_{R\rightarrow C\rightarrow T}$	0.21
$k_{R\rightarrow C\rightarrow A\rightarrow C}$	0.33
$k_{R\rightarrow C}$	0.06
k_T	1.45
$k_{T\rightarrow A}$	0.93
$k_{T\rightarrow C}$	1.24
$k_{T\rightarrow A\rightarrow C}$	3.03

Chapter 3. Hot-Electron-Transfer Enhancement for the Efficient Energy Conversion of Visible Light

3.1 Introduction

Plasmonic nanostructures have been recently proposed to enhance solar conversion efficiency [57–61]. One of the remarkable features of plasmon-induced photocatalysis is the localized surface plasmon resonance (LSPR), which arises from the collective oscillation of free electrons at the metallic interface or in small metallic nanostructures [62–64]. The phenomenon confers several distinct advantages to photocatalytic processes. First, plasmonic metal nanoparticle (NP) acts as photosensitizer in metal/semiconductor junctions and shows a strong absorption at specific wavelengths in the visible region. Second, the metallic NPs effectively act as an antenna, which is useful in semiconductors with a short minority carrier diffusion length. The results of femtosecond pump−probe experiments suggest that the hot electrons in Au NPs have an elastic mean free path of ~10 nm [65,66]. However, hot electron transfer to an adjacent semiconductor still remains a challenge because the hot electrons decay rapidly to lower energy levels through ultrafast electron–electron and electron–phonon scattering on a time scale of a few to some hundreds of femtoseconds [64,67]. The first

demonstration of a plasmon-induced hot electron transfer process in metal-semiconductor nanostructures by Wu et al. revealed that plasmon excitation of Au caused the injection of hot electrons into the CB of CdS with an average quantum yield of ~2.75(±0.07)% [44]. The low quantum yield was found out to be the result of multiple competing pathways for energy dissipation in the hot electron injection process.

In this study, a combinative nanoparticulate system composed of $SrTiO_3$ as a high-performance electron filter and a Au@CdS core-shell as a plasmonic photosensitizer was found to enhance hot electron transfer. The ultrafast decay of the resulting hot electrons was efficiently reduced by the strong coupling of Au and CdS. In addition, a Schottky junction of Au and $SrTiO_3$ facilitated the charge transfer to the CB of $SrTiO_3$ and, in turn, perovskite $SrTiO_3$ enabled a favorable transfer of charge carriers to active sites for H_2 production. The findings also indicated the existence of a favorable electron pathway, CdS → Au → $SrTiO_3$, as evidenced by steady-state and time-resolved photoluminescence spectroscopies. This novel plasmonic nanostructure provides a new and effective strategy for the efficient energy conversion of visible light.

3.2 Experimental

3.2.1 Sample Preparation

$SrTiO_3$ (1.0 g, < 100 nm, Sigma-Aldrich) nanopowder was dispersed in DI water (200 mL) by sonication for 30 min. The $SrTiO_3$ suspension was adjusted to pH 4 by adding diluted HCl (35–37%, Samchun) solution. $HAuCl_4 \cdot 4H_2O$ (≥ 99.9%, Sigma-Aldrich) was added to the suspension, resulting in the deposition of 1 wt% of Au nanoparticles on $SrTiO_3$. After stirring for 30 min, 30 mL of 0.02 M $NaBH_4$ aqueous solution was slowly added to the aqueous dispersion to reduce the Au^{3+} ions. A purple $Au/SrTiO_3$ powder was obtained after stirring for 3 h, followed by centrifugation.

Au@CdS core-shell structures were formed on $SrTiO_3$ by photodeposition. Sulfur (2 mmol) and $Cd(ClO_4)_2 \cdot 6H_2O$ (8 mmol) were added to an ethanol suspension (200 mL) containing $Au/SrTiO_3$. The suspension was irradiated by UV light for 12 h, giving a colour change from purple to green, indicating the formation of CdS shells on Au cores. A 300 W Xe arc lamp (Oriel) was used as the light source for UV-light irradiation. Finally, green $Au@CdS/SrTiO_3$ was obtained after centrifugation.

Pt nanoparticles were selectively deposited on $Au@CdS/SrTiO_3$ by either direct reduction or photodeposition. To deposit Pt nanoparticles on $SrTiO_3$ ($Au@CdS/Pt/SrTiO_3$), $H_2PtCl_6 \cdot 6H_2O$ (≥ 99.9%, Sigma-Aldrich) was added to bare $SrTiO_3$ suspension at pH 4, resulting in the deposition of 1 wt% Pt nanoparticles before the Au deposition on $SrTiO_3$. To deposit the Pt

nanoparticles on CdS shells (Pt/Au@CdS/$SrTiO_3$), $H_2PtCl_6 \cdot 6H_2O$ was added to the methanol suspension containing of Au@CdS/$SrTiO_3$ and the resulting suspension was subsequently irradiated by UV light for 12 h.

A heterojunction of CdS/$SrTiO_3$, used as a control sample, was prepared by the ion-exchange method. $Cd(ClO_4)_2 \cdot 6H_2O$ was added to $SrTiO_3$ suspension resulting in the deposition of 4 wt% of CdS. After stirring for 30 min, 20 mL of 0.02 M Na_2S aqueous solution was slowly added to the aqueous dispersion. CdS/$SrTiO_3$ was obtained after stirring for 3 h followed by centrifugation. To obtain Au/CdS/$SrTiO_3$, the $SrTiO_3$ suspension was adjusted to pH 4 by adding diluted HCl solution. $HAuCl_4 \cdot 4H_2O$ was added to the suspension resulting in the deposition of 1 wt% Au nanoparticles on the $SrTiO_3$, followed by 4 wt% CdS deposition using the ion-exchange method. The concentrations of Au and CdS in the control samples were commensurate with those of Au@CdS/$SrTiO_3$, as determined by ICP-AES (Shimadzu ICPS-7500).

3.2.2. Sample Characterization

The morphology and microstructure were investigated by HRTEM (JEM 3010-JEOL, 300 kV) and XRD (D/max-2500/PC-Rigaku) using Cu Kα radiation (λ = 0.154 nm). Atomic-distribution mapping was obtained by using HAADF-STEM (JEM-2100F, 200 kV), the equipment for which was fitted for performing EDS. The optical absorbance spectra were obtained by UV-DRS (V670-Jasco), using $BaSO_4$ as reference. The dark-field images

and scattering spectra were obtained by using a dark-field microspectroscopy system consisting of a Axio Observer Z1 inverted microscope (Carl Zeiss, Germany) equipped with a dark-field condenser (numerical aperture = 0.8−1.4), a true-colour digital camera and a 1024 pixel × 256 pixel cooled spectrograph CCD camera (Andor Technology PLC, UK) and a 100 W halogen lamp that was used as the light source. A two-way adapter with a selectable output was connected to the camera port of the microscope. This allows the sample image to be reflected to either a colour digital camera or a line-imaging spectrometer. A grating with 300 grooves mm^{-1} (for wide wavelength ranges) was used in the spectrophotometer (Monora320i, Dongwoo Optron Co., Korea). A programmable shutter was mounted internally to an adjustable entrance slit whose width could be manually adjusted to the size of a scattering spot of a single nanoparticle and allows for keeping a single nanoparticle in the region of interest. The spectrometer allows the simultaneous measurement of a maximum of 256 independent spectra in the visible wavelength range through the microscope's field of view.

3.2.3 Photoluminescence Spectroscopy

The steady-state PL was measured with a PerkinElmer LS55 spectrophotometer (PerkinElmer Ltd., Beaconsfield, UK) equipped with a Xe lamp. The measurements were replicated three times in total to obtain average values. Time-resolved PL measurements decay curves were obtained via time-

correlated single photon counting methods using Fluo-Time 200 instrument (Picoquant, Germany). Excitation sources used a 405 nm and a 500 nm pulsed diode laser (pulse energy = 10 pJ; FWHM < 54 ps) with the repetition rate of 80 MHz. The signals were collected at the excitonic emission of 1 μM rhodamine B (RhB, Sigma, for fluorescence, λ_{em}= 580 nm). The temperature of quartz cuvette was maintained at 20 °C by circulating water through an external temperature control device during the time-resolved PL measurements.

3.2.4 Photoelectrochemical Performance Characterization

Chronoamperometric measurements were performed on a computer-controlled potentiostat (ZIVE SP2, WonATech) using a two-electrode cell. Powder-typed photocatalysts were immobilized on ITO glass using a doctor blade (1 cm × 1 cm). A Pt plate was used as counter electrode in an aqueous solution of 0.05 M Na_2S and 0.1 M Na_2SO_3 under visible-light irradiation ($\lambda \geq$ 400 nm). Electrochemical impedance spectroscopy (EIS) experiments were conducted with an applied potential of 0 V under an ac perturbation signal of 5 mV over the frequency range of 1 MHz to 50 mHz. The impedance spectra were analysed using the commercial software ZMAN 2.2. The temperature in the PEC system was maintained at 15 °C by circulating a coolant through an external temperature-control device during the PEC experiments.

3.2.5 Electromagnetic Simulations

The electromagnetic field distribution of Au@CdS/$SrTiO_3$ under irradiation of light at a wavelength of 400 nm and 550 nm was calculated using the DDA method employing the DDSCAT 7.3.0 code [68], which was developed by Drain and Flatau [69]. The structural model for the DDA calculations contained a $SrTiO_3$ nanosphere, an Au core, and a CdS shell. The inter-dipole separation was set at ca. 1 nm for the target nanostructure, which generated 65,745 dipoles for the DDA calculations. The dielectric constants of $SrTiO_3$, Au, and CdS were obtained from the literature [70,71].

3.2.6 Photocatalytic Activities

The photocatalytic activities of the prepared samples were evaluated by the H_2 production rates under visible light irradiation by a 300 W Xe lamp with a 400 nm cut-off filter. The photocatalyst (0.15 g) was suspended in an aqueous solution of 0.05 M Na_2S and 0.1 M Na_2SO_3 (100 mL). The photocatalytic activities of $SrTiO_3$ and Au/$SrTiO_3$ were further measured in an aqueous solution of 20 vol.% methanol. The reaction temperature was maintained at 15 °C by circulating water through an external temperature-control device. The amount of produced H_2 was quantified using gas chromatography (YL6100 GC, Young Lin) equipped with a TCD. A glass filter (cut-off < 400, 420, 435, 455, 495, 550, 590, and 630 nm) was used for the irradiation at various specific wavelengths of visible light during the experiments. The apparent QE for H_2 generation was calculated using the following equation,

$$\mathrm{QE}\ (\%) = \frac{n \times N(\mathrm{H_2})}{N(\mathrm{photons})} \times 100 \tag{3-1}$$

where the electron factor, n, of the reaction ($2H^+ + 2e^- \rightarrow H_2$) is 2, and $N(H_2)$ is the number of generated H_2 molecules per hour (H_2 generation rate) which can be extracted from the slope of H_2 production as a function of time. N(photons) is the number of absorbed photons during the H_2 generation and is to be calculated by taking the light intensity, I, through an optical power meter (Nova, Ophir). The measured I in the wavelength range of 400 to 800 nm was 0.146 W where all photons are assumed to be absorbed in the photocatalyst and then produce a viable electron–hole pair. The spectral distribution of the 300W Xe lamp (6258 model of Newport corporation) without any filter is almost featureless in the whole visible range [72]. The photon energy, E, at a certain wavelength can be calculated according to Planck-Einstein relation,

$$E = \frac{hc}{\lambda} \tag{3-2}$$

where h is the Plank's constant (6.626×10^{-34} J s), c is the speed of light (2.998×10^8 m s^{-1}), and λ is the wavelength of light. The energy of one mole of photons can be calculated by multiplying the photon energy by the Avogadro constant, N_A (6.022×10^{23} mol^{-1}). The result is that the irradiated light with the average wavelength, 600 nm, has energy of 1.993×10^5 J mol^{-1}. Therefore, N(photons) is given by,

$$N(photons) = \frac{I}{E} \tag{3-3}$$

The value was found to be 2.637×10^{-3} Einstein h^{-1}.

3.3 Results and Discussion

3.3.1 Morphological and Compositional Investigations

Figure 3.1a shows the scheme for the synthesis of a Au@CdS core-shell deposited on the surface of a $SrTiO_3$ NP (Au@CdS/$SrTiO_3$). The detailed experimental procedures are given in the Experimental section. Briefly, the positively charged surface state of $SrTiO_3$ assists in the adsorption of $AuCl_4^-$ anions in a pH-controlled environment. Au NPs are deposited on the surface of the $SrTiO_3$ using $NaBH_4$, a strong reducing agent. Au@CdS core-shell structures are formed in an ethanol suspension containing Au/$SrTiO_3$, sulfur, and Cd^{2+} cations. Excess sulfur molecules with an affinity for Au are adsorbed on the surface of the Au NPs. When the resulting suspension is irradiated with UV light, the sulfur molecules adsorbed on the Au NPs are reduced to S^{2-} anions, which instantly react with Cd^{2+} cations to form CdS shells around the Au NPs. Although the Au@CdS core-shell structure has been proposed by our previous research and Tada et al. for a solid state Z-scheme under visible light or UV irradiation [4,8], the preparation method described in this study was altered so as to achieve the optimal response of the Au NPs to the visible light by the LSPR effect. For example, the method resulted in Au NPs with a controlled size and the deposited Pt NPs functioned as a co-catalyst on the surface of the $SrTiO_3$. In addition, the Au@CdS/$SrTiO_3$ nanostructure entirely reversed the Z-schematic charge-transfer direction and even changed the main active site for H_2 generation

from CdS to $SrTiO_3$. Notably, whereas two semiconductors consisting of the Z-schematic system should generate electron–hole pairs, $SrTiO_3$ in the Au@CdS/$SrTiO_3$ nanostructure do not generate electrons during the H_2 generation but acted as an electron filter for the efficient hot electron transfer.

The high-angle annular dark-field scanning transmission electron microscopy (HAADF-STEM) image shown in **Figure 3.1b** shows that the as-synthesized Au@CdS/$SrTiO_3$ contain a few Au cores with a diameter of 11.5±4.7 nm (see **Figures 3.2a–e**) that are deposited on the surface of the $SrTiO_3$ NPs (< 100 nm) and CdS shells with a thickness in the range of 3 to 5 nm around the Au cores. **Figure 3.1c** displays the energy-dispersive X-ray spectroscopy (EDS) results of a core-shell structure selected in **Figure 3.1b**, which confirmed that the material is composed of a Au core and a CdS shell on the surface of a $SrTiO_3$ NP. The high-resolution transmission electron microscopy (HRTEM) image shown in **Figure 3.1d** was taken at the interface region of the $SrTiO_3$ and Au@CdS core-shell and clearly reveals three distinct types of lattice fringes, which are assigned to $SrTiO_3$ (JCPDS #01-1018), Au (JCPDS #01-1172), and CdS (JCPDS #41-1049), respectively. The interface between the $SrTiO_3$ and Au core is believed to be important for the injection of hot electrons from Au to the CB of $SrTiO_3$ upon LSPR excitation.

3.3.2 Photocatalytic Activities

Photocatalytic H_2 production was performed under irradiation with visible light ($\lambda \geq 400$ nm) in an aqueous suspension (**Figure 3.3**). The photocatalytic activities of bare $SrTiO_3$, Au/$SrTiO_3$, CdS/$SrTiO_3$, and Au/CdS/$SrTiO_3$ were compared with that of Au@CdS/$SrTiO_3$ in which all the samples have almost the same concentrations of Au (1 wt%) and CdS (4 wt%), as determined by ICP-AES. The H_2 production of bare $SrTiO_3$ is negligible because the catalyst can only be excited by UV light. About 0.4 μmol h^{-1} (quantum efficiency, QE = 0.03%) of H_2 molecules were produced by the Au/$SrTiO_3$ catalyst, despite the poor sensitivity of $SrTiO_3$ to visible light. The performance of Au/$SrTiO_3$ can be attributed to the injection of plasmon-induced hot electrons into the CB of $SrTiO_3$. CdS/$SrTiO_3$ produced H_2 at a rate of 2.5 μmol h^{-1} (QE = 0.19%). As is well-known, CdS-sensitized semiconductor composites (e.g., CdS/TiO_2) can generate large amounts of H_2 due to the enhanced charge separation by the heterojunction structure [49–51]. If a part of Au NPs may not be covered with CdS, they can play a role of co-catalyst for H_2 production. The Au/CdS/$SrTiO_3$ photocatalyst for which Au and CdS NPs were individually isolated on the surface of $SrTiO_3$, was examined for the sake of comparison. The photocatalyst produced H_2 at a rate of 5.0 μmol h^{-1} (QE = 0.38%) which was twice as fast as the CdS/$SrTiO_3$. This is because the photoexcited electrons in the CB of CdS are shuttled to the CB of $SrTiO_3$, and then they are entrapped by Au NPs which accelerated the H_2 production. Interestingly, Au@CdS/$SrTiO_3$ showed an impressive photosynthetic H_2 production rate of 29.1 μmol h^{-1} (QE = 2.21%). This can be attributed to the synergistic effect of (1) plasmonic

photosensitization of the Au@CdS core-shell, (2) the formation of a Schottky junction between the Au core and $SrTiO_3$, and (3) perovskite $SrTiO_3$ with a high CB with respect to the water-reduction potential. The spatial distribution of the electric field strength at the nanoparticulate system was calculated by the discrete dipole approximation (DDA) method. The incident light was assumed to propagate along the *x*-axis. When the Au@CdS/$SrTiO_3$ nanostructure was irradiated with monochromatic light at a wavelength of 400 nm, the intensity of the electric field near the CdS shell was much higher than that at the Au core as well as the interface of the Au core and $SrTiO_3$ (**Figure 3.4a**). **Figure 3.4b** shows that the electric field in the *z*-dimension was strongly localized at the interface between the Au core and the $SrTiO_3$ under irradiation by monochromatic light at a wavelength of 550 nm due to the LSPR of the Au core, whereas the electric field was relatively weak at the CdS shell and the interface of Au core/CdS shell. The enhanced near-field amplitudes which resulted from the LSPR of the Au core and the excitation of CdS shell increased the rate of formation of electron–hole pairs near the interface of the $SrTiO_3$ and Au core. Therefore, H_2 production was improved at a wavelength longer than 400 nm. The second prominent feature of the Au@CdS/$SrTiO_3$ nanostructure was the formation of a Schottky junction between the Au core with a large work function of 5.1 eV and *n*-type $SrTiO_3$. When a Schottky junction is formed, the bands of $SrTiO_3$ are bent upward with respect to the energy level in the bulk $SrTiO_3$ because the positive charge in the space-charge region negatively shifts the band energies of $SrTiO_3$ with increasing distance from the surface. The

direction of the electric field is such that excess electrons injected into the space-charge region would move toward the bulk of $SrTiO_3$, which promotes the separation of electron–hole pairs. Although the Au core can also form a Schottky junction with an *n*-type CdS shell, the space-charge region with a typical width of 5 to 200 nm cannot fully develop within the thin CdS layer at the interface [73,74]. Even if a space-charge region was present at the interface between the CdS shell and the Au core, the contact potential would be reduced by the absorption of visible light. As a result, photoexcited electrons in the CB of the CdS shell can easily diffuse into the Au core. Finally, perovskite $SrTiO_3$ favors the chemical reactions of photoexcited electrons with H^+ adsorbed at the surface of the $SrTiO_3$ due to the CB minimum of ~0.8 eV, which is higher than the water-reduction potential [75,76]. The activity of $SrTiO_3$ nanoparticles for H_2 production was compared with that of anatase TiO_2 nanoparticles (**Figure 3.5**). Au@CdS/$SrTiO_3$ produced 2 times more H_2 gas than the 14.8 μmol h^{-1} (QE = 1.12%) for Au@CdS/TiO_2 which was prepared by the same method using anatase-structured TiO_2 nanoparticles (< 100 nm). Since $SrTiO_3$ nanoparticles acted as a high-performance electron filter, the Au@CdS/$SrTiO_3$ nanostructures increased the amount of produced H_2 gas to as considerable extent from water under irradiation by visible light.

In order to investigate the electron-transfer processes, we prepared control samples of Pt/Au@CdS/$SrTiO_3$ and Au@CdS/Pt/$SrTiO_3$ nanocomposites. Pt/Au@CdS/$SrTiO_3$ was a photocatalyst for which 1 wt% Pt NPs were deposited on the CdS shell by the Z-scheme mechanism of Au@CdS/$SrTiO_3$

under UV light (**Figures 3.6a–c**). Au@CdS/Pt/$SrTiO_3$ was a photocatalyst for which 1 wt% Pt NPs were deposited on the surface of the $SrTiO_3$ by the direct reduction method using $NaBH_4$ before the formation of Au@CdS core-shell on $SrTiO_3$ (**Figures 3.7a,b**). The amount of H_2 produced using Pt/Au@CdS/$SrTiO_3$ and Au@CdS/Pt/$SrTiO_3$ were 129.4 (QE = 9.81%) and 163.6 μmol h^{-1} (QE = 12.41%), respectively. The experimental results implied that most of the photoexcited electrons originating from the Au@CdS core-shell structures flowed to the surface of $SrTiO_3$ through a cascade of energy states.

3.3.3 Electron-Transfer Processes

I carried out steady-state PL measurements in order to investigate the electron-transfer processes of Au@CdS/$SrTiO_3$ nanostructure. In these experiments, RhB was used as an indicator dye to monitor the interfacial charge transfer. The PL emission of RhB can be quenched by $SrTiO_3$ as well as CdS, since the LUMO level of RhB (–1.1 V vs NHE) is higher than the CB minimum of $SrTiO_3$ (–0.8 V vs NHE) and CdS (–1.0 V vs NHE). The peak emission wavelength of RhB was at 580 nm, which is constant regardless of the excitation wavelength (**Figure 3.8a**). The PL emission of $SrTiO_3$ in the absence of RhB can be seen in **Figure 3.8b**, and the PL was considered to result from the recombination of electrons and holes in a self-trapped exciton state [77–79]. **Figure 3.8c** shows steady-state PL spectra of the prepared samples suspended in an aqueous solution of RhB as a function

of excitation wavelength. The $SrTiO_3$ suspended in the RhB solution showed a higher PL emission than pure RhB at excitation wavelengths of 405 to 480 nm. This can be attributed to the overlapping emission of $SrTiO_3$ and RhB. A depression in the PL emission of RhB in the presence of $SrTiO_3$ was observed for excitation wavelengths longer than 480 nm. In the excitation range the RhB showed a strong emission, but the emission of $SrTiO_3$ was relatively weak. Au nanoparticles on the surface of $SrTiO_3$ showed a noticeable quenching in the PL emission of RhB, considering the PL emission of Au/$SrTiO_3$ itself, indicating that the photoexcited electrons from RhB were transferred to the CB of $SrTiO_3$ as well as to the Fermi level of Au nanoparticles. In particular, the fluorescence emission of RhB was suppressed to a greater extent when the Au/$SrTiO_3$ was irradiated by an excitation wavelength longer than 500 nm. The suppression can be attributed to the LSPR excitation of Au nanoparticles, leading to the hot electron transfer to the CB of $SrTiO_3$ as well as a charge transfer from the excited RhB to the Fermi level of Au. The electrons in the interband electron–hole pairs in the Au have insufficient energy for injection into the CB of $SrTiO_3$ due to its lower Fermi level than the CB minimum of $SrTiO_3$. However, hot electrons can be injected into the CB of $SrTiO_3$, as has been reported by Wu et al., who reported that the electronic energy level in the intraband electron–hole pairs was 2.10 eV above the Fermi level of Au [44]. An obvious depression in the PL intensity of RhB was also noted with a deposition of CdS nanoparticles on the surface of $SrTiO_3$ when the excitation wavelength was shorter than 480 nm. The depression was due to the excitation of CdS,

which facilitated a charge transfer from the CB of CdS to the CB of $SrTiO_3$. As a result, the photoexcited electrons of RhB were transferred to the CB of CdS faster than to Au nanoparticles of $Au/SrTiO_3$ at the excitation wavelength (λ_{ex} < 480 nm). However, the PL depression of RhB by $Au/SrTiO_3$ was superior to the $CdS/SrTiO_3$ at the excitation wavelength (λ_{ex} > 480 nm). This phenomenon was also observed in the CdS suspended in RhB solution. Although the CdS showed an excellent depression at the excitation wavelength (λ_{ex} < 480 nm), the PL depression of RhB by CdS was inferior to that for $Au/SrTiO_3$ at the excitation wavelength (λ_{ex} > 480 nm). In the case of $CdS/SrTiO_3$ in the absence of RhB, the PL emission of $SrTiO_3$ increased gradually with an increase in excitation wavelength due to the weak excitation of CdS. $Au@CdS/SrTiO_3$ suspended in RhB solution showed a synergistic effect on PL depression of RhB. The photoexcited electrons of RhB were quenched by the excitation of the CdS shell at the excitation wavelength (λ_{ex} < 480 nm), and quenching by $Au@CdS/SrTiO_3$ was more pronounced than that of $Au/SrTiO_3$ and $CdS/SrTiO_3$ at the excitation wavelength (λ_{ex} > 480 nm) due to the simultaneous excitation of the Au core and CdS shell. The electrons in the CB of CdS shell could be injected into the Fermi level of the Au core, which is strongly coupled to the CdS shell (see Optical Properties section), and the electrons injected into Au core quenched the positive charges remaining in the Au core upon LSPR excitation. $Au@CdS/SrTiO_3$ in the absence of RhB also depressed the PL emission of $SrTiO_3$ more than that of $Au/SrTiO_3$ and $CdS/SrTiO_3$ over the entire range of excitation wavelength (405 nm < λ_{ex} < 530 nm).

Figures 3.9a,b show the time-resolved PL spectra of the prepared samples suspended in an aqueous solution of RhB (indicator dye to monitor the interfacial charge transfer) with excitation wavelengths of 405 nm (for the excitation of CdS) and at 500 nm (for the simultaneous excitation of CdS and Au), respectively. The resulting fluorescence was analyzed and fitted to a multi-exponential model. In the model equation, the intensity is assumed to decay as a sum of individual single exponential decays which is described as

$$I(t) = \sum_{i=1}^{n} A_i e^{-t/\tau_i} \quad (3\text{-}4)$$

where τ_i is the decay time, A_i represents the amplitude of the components at t = 0, and n is the number of decay times. The quality of fitting was assessed by the reduced χ^2 value. All of the fitting parameters are summarized in **Tables 3.1 and 3.2**. Electron pathways were constructed with differential equations, in an attempt to understand the kinetics of the process based on the results of steady-state PL spectroscopy data (**Tables 3.3 and 3.4**). In the schematic process, R, S, A, and C denote RhB, $SrTiO_3$, Au, and CdS, respectively. In addition, $N_R(t)$ and $N_S(t)$ refer to the time-dependent electron populations in the lowest unoccupied molecular orbital (LUMO) of RhB and CB of $SrTiO_3$, respectively. The fluorescence decay of RhB and RhB in the presence of CdS can be expressed as a single-exponential function, since CdS hardly emits the PL at the excitation wavelength. However, the decay traces of RhB in the presence of $SrTiO_3$, Au/$SrTiO_3$, CdS/$SrTiO_3$, and Au@CdS/$SrTiO_3$ can be expressed as a bi-exponential function since both RhB and $SrTiO_3$ emit the PL at 580 nm. The obtained time-resolved spectra

represent the sum of the PL_1 of RhB (N_R) and PL_2 of $SrTiO_3$ (N_S). Therefore, the pre-exponential factors A_i indicate the relative contribution of N_R and N_S on the obtained time-resolved PL spectra. τ_1 and τ_2 in the exponential term describe the decay of the electron population in the photoexcited RhB and the CB of $SrTiO_3$, respectively. The decay rate of the electron population in RhB and the CB of $SrTiO_3$ could be experimentally assessed by fitting the time-resolved PL curve with equation 3-4. **Table 3.5** summarizes the electron-transfer rate constants at the different excitation wavelengths. The rate constants were calculated by comparing the exponents, k, in the differential equations with the values for τ_i extracted from the fitted results of time-resolved PL spectra. The fluorescence of pure RhB at the excitation wavelength (λ_{ex} = 405 nm) showed a single-exponential decay with an emission lifetime of 1.711 ns which was constant at the long excitation wavelength (λ_{ex} = 500 nm), and its recombination rate constant based on the expression $k_R = 1/\tau_1$(RhB), was approximately 5.84×10^8 s^{-1}. The addition of $SrTiO_3$ led to faster fluorescence decay of RhB, which could be described by the bi-exponential model. The interfacial charge transfer from the excited RhB to the CB of $SrTiO_3$ decreased the lifetime, τ_1, of RhB. Its rate constants for the charge transfer, $k_{R\rightarrow S}$, were 0.38×10^8 s^{-1} at λ_{ex} = 405 nm and 0.32×10^8 s^{-1} at λ_{ex} = 500 nm. In addition, the recombination rate constants for $SrTiO_3$ could be obtained from the second lifetime, τ_2, that was affected by the fluorescence decay of $SrTiO_3$. The corresponding rate constants, k_S, were determined to be 2.80×10^8 s^{-1} at λ_{ex} = 405 nm and 2.90×10^8 s^{-1} at λ_{ex} = 500 nm. Au/$SrTiO_3$ suspended in RhB facilitated the fluorescence decay of RhB,

since the photoexcited electrons from RhB were further transferred to the Fermi level of Au NPs, $k_{R\rightarrow A}$, approximately 0.42×10^8 s^{-1} at λ_{ex} = 405 nm. In particular, the rate increased to 1.17×10^8 s^{-1} for an excitation wavelength of 500 nm. The increase can be attributed to the LSPR excitation of Au NPs, leading to the sequential hot electron transfer to the CB of $SrTiO_3$. Since Au and CdS did not emit the PL, most of the electrons injected into Au or CdS from the RhB were assumed to be transferred to the CB of $SrTiO_3$. For this reason I designated $k_{R\rightarrow A}$ to $k_{R\rightarrow A\rightarrow S}$ at λ_{ex} = 500 nm. However, the deposition of Au NPs caused the electrons in the CB of $SrTiO_3$ to recombine at the Fermi level of Au. Its rate constants, $k_{S\rightarrow A}$, were 0.04×10^8 s^{-1} at λ_{ex} = 405 nm and 0.10×10^8 s^{-1} at λ_{ex} = 500 nm. CdS/$SrTiO_3$ suspended in RhB also promoted the fluorescence decay of RhB since the photoexcited electrons from RhB are sequentially transferred to the CB of CdS and $SrTiO_3$, $k_{R\rightarrow C\rightarrow S}$. The $k_{R\rightarrow C\rightarrow S}$ (0.85×10^8 s^{-1}) at λ_{ex} = 500 nm was slower than that (1.01×10^8 s^{-1}) at λ_{ex} = 405 nm due to the weak excitation of CdS, and the decay of electrons in the CB of $SrTiO_3$ to the VB of CdS, $k_{S\rightarrow C}$, were 1.28×10^8 s^{-1} at λ_{ex} = 405 nm and 0.04×10^8 s^{-1} at λ_{ex} = 500 nm. When the Au@CdS/$SrTiO_3$ was suspended in RhB, the photoexcited electrons of RhB could be transferred to the CB of $SrTiO_3$ and the CdS shell. The electrons in the CB of CdS shell could be injected into the Au core strongly coupled to CdS shell. Then, the electrons injected into Au core are likely to decay to the VB of CdS at λ_{ex} = 405 nm, $k_{R\rightarrow C\rightarrow A\rightarrow C}$ (1.10×10^8 s^{-1}) or quench the positive remaining charges at the Au core upon LSPR excitation at λ_{ex} = 500 nm. At λ_{ex} = 500 nm, the separated hot electrons of the Au core could be

sequentially transferred to the CB of $SrTiO_3$, and its rate constant was denoted by $k_{R\rightarrow C\rightarrow A\rightarrow S}$. The rate constant ($1.94 \times 10^8$ s^{-1}) was even higher than the $k_{R\rightarrow A\rightarrow S}$ (1.17×10^8 s^{-1}) of Au/$SrTiO_3$ at λ_{ex} = 500 nm. These observations explain the hot electron transfer enhancement of Au@CdS/$SrTiO_3$.

Regarding the above results, I propose the following electron-transfer processes in Au@CdS/$SrTiO_3$ nanostructure under irradiation by visible light (**Figure 3.9c**). The excitation of LSPR in the Au core transiently produces electron–hole pairs with hot electrons at empty states above the Fermi level of the Au core. When a certain number of hot electrons arrive at the interface of the Au core and $SrTiO_3$, a fraction of the hot electrons is injected into the CB of $SrTiO_3$ [80–82]. The hot electrons then diffuse to the surface of the $SrTiO_3$ and are subsequently entrapped by Pt NPs which provide active sites for H_2 production and enhance the charge separation. Meanwhile, a significant fraction of residual holes at the Au core are removed by the electrons injected from the CdS shell, and the sacrificial ions quench the holes at the CdS shell.

3.3.4 Optical Properties

Au@CdS/$SrTiO_3$ exhibited a significant enhancement in the absorption of visible light compared to bare $SrTiO_3$, which had a wide bandgap of 3.3 eV (**Figure 3.10a**). There were two shoulders and a broad peak in the absorption spectra. One shoulder, observed in Region A, is assigned to bare $SrTiO_3$. The

other shoulder in Region B is the result of the presence of the CdS shell whose bandgap was approximately 2.3 eV. The broad peak centered at 590 nm results from the LSPR of the Au cores, and the LSPR band was significantly broadened and red-shifted by ca. 60 nm as compared to that (530 nm) for $Au/SrTiO_3$. The broadening and red shift suggest the existence of strong electronic interactions between Au core and CdS shell with a high refractive index [44,83]. A $Au/CdS/SrTiO_3$ sample was examined to demonstrate the strong electronic interactions. The LSPR band of $Au/CdS/SrTiO_3$ was red-shifted by less than ca. 20 nm, indicating that the electronic coupling of Au core and CdS shell in $Au@CdS/SrTiO_3$ was much stronger than that of $Au/CdS/SrTiO_3$ (**Figure 3.10b**).

A shift in the plasmon resonances based on the difference in the shapes of the nanostructures was also demonstrated by dark-field scattering. In a typical experiment, a particle was irradiated by white light and the Rayleigh-scattered light from an individual particle was collected by a dark-field microscope in the transmission mode. Insets of **Figure 3.10c** show typical dark-field images and the corresponding scattering spectra of Au nanoparticles in exclusion of the scattering by $SrTiO_3$. The Au nanoparticles of $Au/SrTiO_3$ showed a plasmon resonance with a scattering peak centered at 575 nm and appear as a green color in the dark-field image. After the the CdS shell is formed around the Au core, the scattering peak was red-shifted to 635 nm and the green spot in the dark-field image of $Au/SrTiO_3$ was changed to a faint yellow halo surrounding the green spot. The dark-field results provided further evidence for the existence of strong interactions between the Au core and the CdS shell.

The selected individual particles of the scattering spectra are represented by red circles in the dark-field images of a large-field view (**Figure 3.11**). The low contrast of the dark-field images could be attributed to the reflection of white light by $SrTiO_3$ which is much stronger than light scattered by Au nanoparticles.

The photosynthetic rate of production of H_2 by Au@CdS/Pt/$SrTiO_3$ was also investigated under irradiation by visible light at various wavelengths (**Figure 3.10d**). The rate of H_2 production when 0.05 g of the catalyst Au@CdS/Pt/$SrTiO_3$ was used significantly decreased with an increase in the cut-off wavelength from 400 nm to 550 nm due to a decrease in the photocatalytic activity of the CdS shell. The rate of H_2 production increased slightly in the wavelength range of 550 to 630 nm (expanded inset) by the sole operation of plasmon-induced hot electrons where the amount of H_2 produced was similar to that of Au/$SrTiO_3$. The results of wavelength-dependent H_2 production were in good agreement with the absorbance spectrum of the Au@CdS/$SrTiO_3$, indicating that the hot electrons are excited due to the LSPR characteristics of the Au core in the CdS shell.

3.3.5 Photoelectrochemical Performance

The previous sections focused on the conversion of visible light to chemical energy, H_2. Photoexcited electrons of the Au@CdS/$SrTiO_3$ nanostructure can be also used to directly generate electrical energy in a PEC cell. The components of the Au@CdS/Pt/$SrTiO_3$ nanoparticulate system were

reconfigured in order to produce a PEC device, using Au@CdS/$SrTiO_3$ as the photoanode and a Pt plate as the cathode. First, chronoamperometric current–time (*I*–*t*) curves were measured at an applied potential of 0 V under irradiation by visible light ($\lambda \geq 400$ nm) with 30 s on/off cycles. Bare $SrTiO_3$, Au/$SrTiO_3$, and CdS/$SrTiO_3$, as shown in the expanded inset of **Figure 3.12a** generated photocurrent densities of ~0.8, ~1.2, and ~8 μA cm^{-2}, respectively. It is noteworthy that a significant enhancement in the photocurrent density of ~200 μA cm^{-2} was observed when Au@CdS/$SrTiO_3$ was used as a photoanode. However, the obtained photocurrent density of Au@CdS/$SrTiO_3$ was less than that of the expected photocurrent density. As shown in the schematic diagram of **Figure 3.13**, when the photoanode is prepared by a doctor blade, the photoexcited electrons pass through numerous $SrTiO_3$ nanoparticles to reach the ITO circuit. However, a fraction of the electrons participate in side reactions with H^+ ions that are adsorbed at the surface of $SrTiO_3$ to produce H_2 gas in the course of a 3D random walk. For further characterization of the designed photoelectrodes, I carried out EIS measurements at an applied potential of 0 V under irradiation by visible light ($\lambda \geq 400$ nm), presented in the form of Nyquist plots (**Figure 3.12b**). An equivalent circuit for the PEC reaction was designed with a serial combination of the bulk electrolyte resistance, R_Ω, and the interfacial reaction impedance that is represented by a parallel combination of double-layer capacitance, C_{dl}, and the charge-transfer resistance, R_{ct}, as shown in **Figure 3.14**. In this circuit, the constant phase element (CPE) can replace C_{dl} at the electrode–electrolyte interface. The impedance of the CPE, Z_{CPE}, is given as follows:

$$Z_{CPE} = \frac{1}{Q_0 (jw)^n} \quad (3\text{-}5)$$

where Q_0 is the admittance magnitude of the CPE and n is the exponent related to the phase angle φ by $\varphi = n(\pi/2)$. The kinetic parameters extracted from the impedance measurements were calculated with the equivalent circuit, and the results are summarized in **Table 3.6**. The R_{ct} of bare $SrTiO_3$ decreased by a factor of 1/16 after the formation of Au@CdS core-shell structures on the $SrTiO_3$ (87.7 kΩ → 5.3 kΩ). The significantly reduced R_{ct} clearly explains why the Au@CdS/$SrTiO_3$ displays an excellent photocurrent in the visible-light region.

3.3.6 Adverse Effects of Au@CdS/$SrTiO_3$ Nanostructure

Some adverse effects of the Au@CdS/$SrTiO_3$ nanostructure were observed on the photocatalytic activities. A common problem is the shading effect. An excess amount (more than 1 wt%) of Au core on the surface of $SrTiO_3$ resulted in the formation of large aggregations of CdS shells (**Figure 3.15**). This aggregation reduced, not only the specific surface area of the CdS shell, but also disrupted the absorption of light by the Au core. The Pt nanoparticles as a co-catalyst also competed with Au@CdS core-shell to occupy the limited surface of the $SrTiO_3$ and, as a result, the use of more than 1 wt% Pt hindered the light absorption of the Au@CdS core-shell structures. I optimized the photocatalyst preparation conditions, such as the pH of the $SrTiO_3$ suspension for Au deposition and the amount of Au and Pt nanoparticles loaded on the

surface of the $SrTiO_3$ (**Figure 3.16a–c**). Another point is the stability of the CdS shell. In order to check the stability of Au@CdS/Pt/$SrTiO_3$, H_2 production was performed for 20 h. The Au@CdS/Pt/$SrTiO_3$ suspension had a high durability during the recycling experiments in the presence of sacrificial ions (**Figure 3.16d**).

3.4 Conclusion

I demonstrated an enhancement in hot electron transfer of a Au core by the strong electronic coupling to a CdS shell that is in direct contact with perovskite $SrTiO_3$ NPs for the effective conversion of visible light to clean H_2 or to electricity. The enhanced H_2 production can mainly be attributed to the synergistic effect of the following three features: (1) The plasmonic photosensitization of Au@CdS core-shell generated more active electron–hole pairs. (2) Band bending between the Au core and $SrTiO_3$ enabled hot electrons to be easily ejected from the Au core into the CB of $SrTiO_3$. (3) Perovskite $SrTiO_3$ played an important role as a high-performance electron filter, better than TiO_2, and has a sufficiently high CB to produce H_2. Consequently, the Au@CdS/$SrTiO_3$ nanostructure provided a favorable electron pathway, CdS → Au → $SrTiO_3$ for the efficient separation of electron–hole pairs, although Au with a large work function, was sandwiched in the middle of the $SrTiO_3$ and CdS. The designed nanostructure achieved a remarkable photocatalytic H_2 production and electron harvest at various wavelengths of visible light.

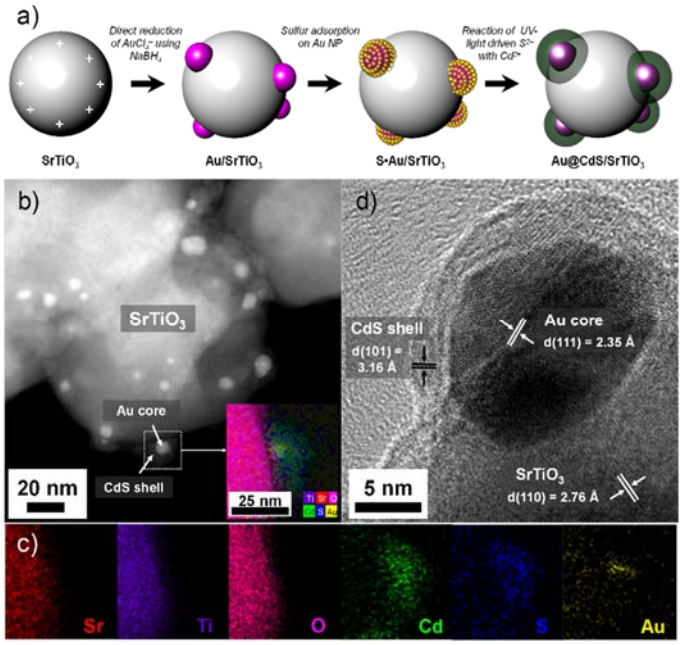

Figure 3.1 Morphology and composition of $Au@CdS/SrTiO_3$ nanostructures using microscopy techniques. (a) Scheme (upper row) for the preparation of $Au@CdS/SrTiO_3$ nanostructure. The first image (left) indicates the surface state of a $SrTiO_3$ NP with positive charges in an aqueous suspension at pH 4. The second image illustrates the deposition of Au NPs on the surface of $SrTiO_3$ by direct reduction of $AuCl_4^-$ using $NaBH_4$. Third, sulfur molecules are adsorbed onto the surface of the Au NPs due to their affinity to Au. Finally, sulfur molecules are reduced to S^{2-} ions which instantly react with Cd^{2+} to form CdS shells under irradiation of UV. (b) HAADF-STEM image of Au@CdS core-shell structures distributed on the surface of a $SrTiO_3$ NP. (c) 2D atomic mapping of Sr, Ti, O, Cd, S, and Au obtained by using analytical STEM-EDS. (d) HRTEM image taken at the interface region of $SrTiO_3$ and Au@CdS.

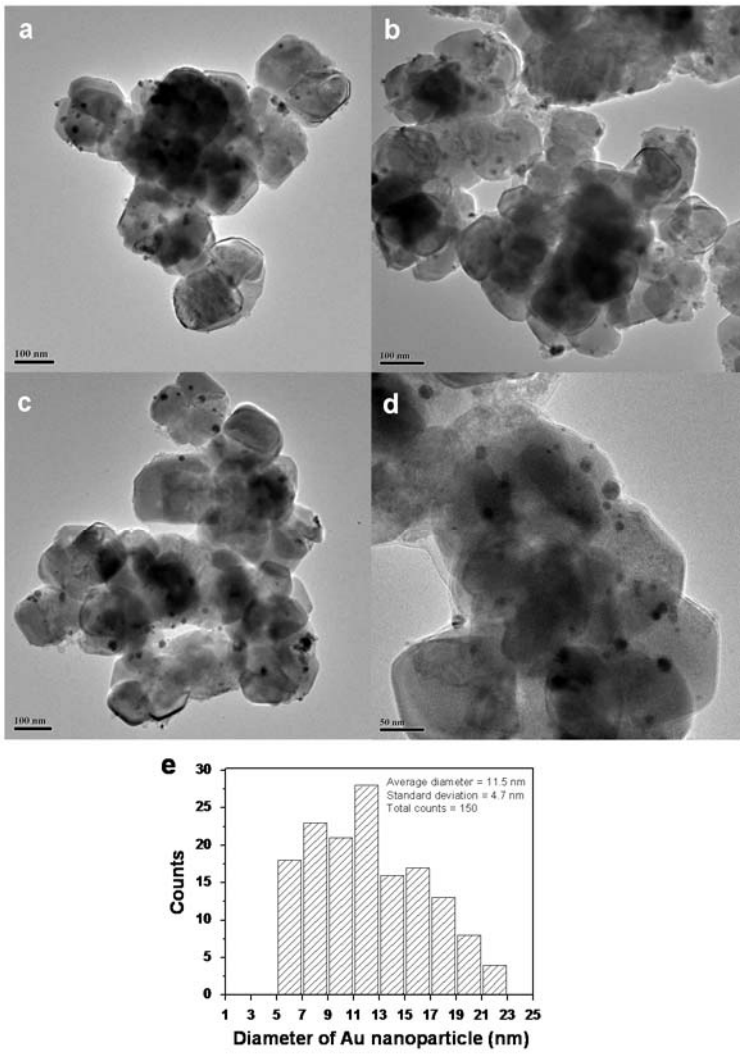

Figure 3.2 Size distribution of Au nanoparticles in Au@CdS/$SrTiO_3$ nanostructure. (a−d) TEM images and (e) the corresponding size distribution. The average diameter (±standard deviation) of Au nanoparticles is 11.5(±4.7) nm, calculated by counting the diameter of 150 individual Au nanoparticles from the TEM images.

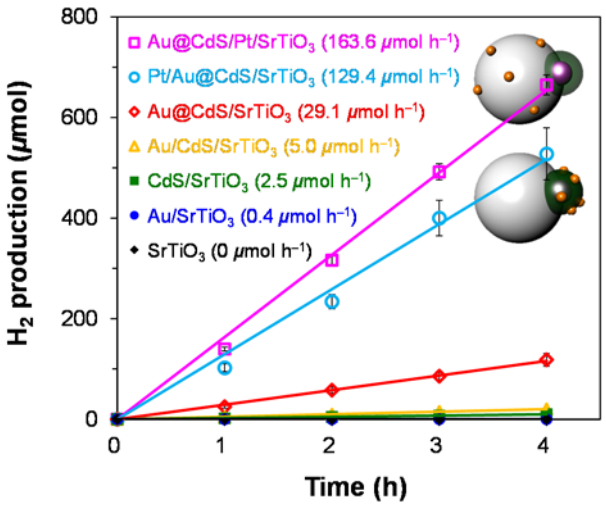

Figure 3.3 Photocatalytic H_2 production as a function of time under visible-light irradiation ($\lambda \geq 400$ nm).

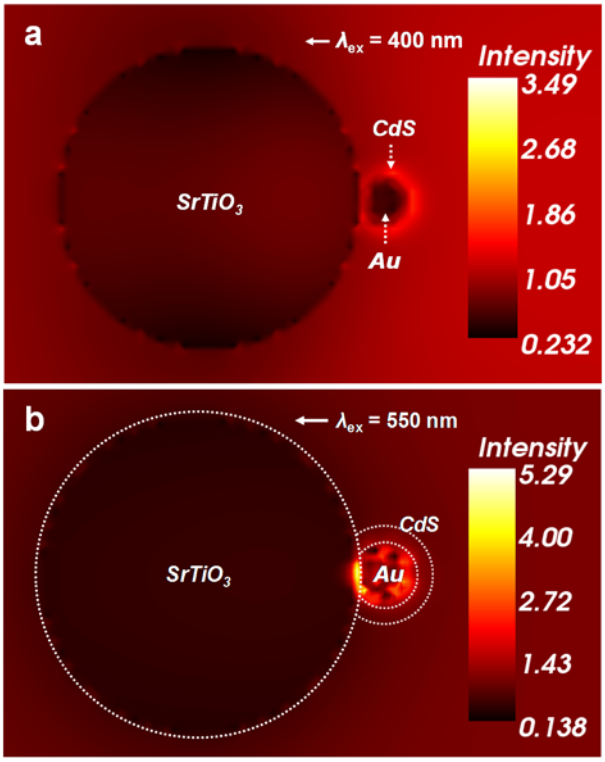

Figure 3.4. Electric field strength of Au@CdS/$SrTiO_3$ calculated by DDA simulations for incident light at a wavelength of (a) 400 nm and (b) 550 nm.

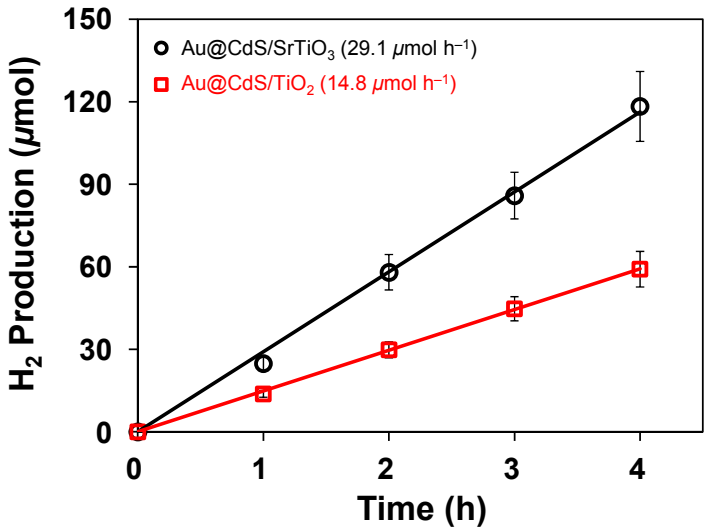

Figure 3.5 Electron-filter dependent photocatalytic activities. H_2 production as a function of time. Reaction conditions: 0.15 g of catalyst, 100 mL of water containing 0.05 M Na_2S and 0.1 M Na_2SO_3, and 300 W Xe lamp with a 400 nm cut-off filter.

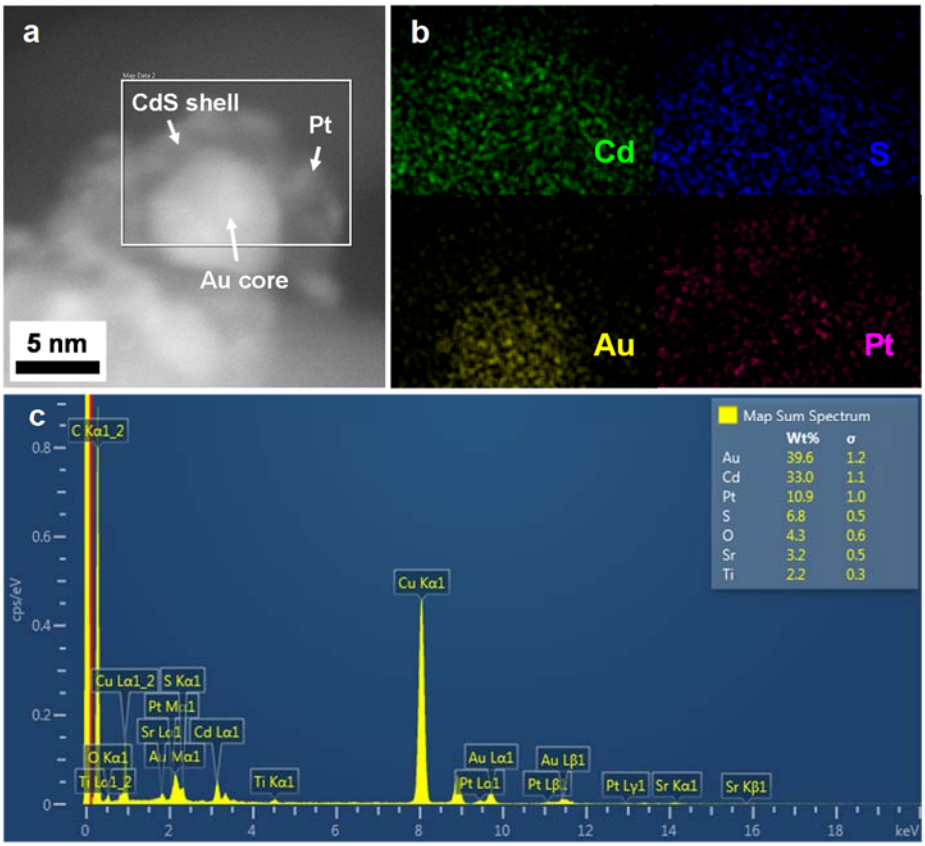

Figure 3.6 Morphological and compositional information of Pt/Au@CdS/$SrTiO_3$ nanostructure. (a) HAADF-STEM image of Pt/Au@CdS/$SrTiO_3$ nanostructure, showing that Pt nanoparticles are expensively dispersed on the surface of a CdS shell. (b) 2D atomic mapping of Cd, S, Au, and Pt in the selected area. (c) EDS spectrum of the Pt/Au@CdS/$SrTiO_3$ nanostructure.

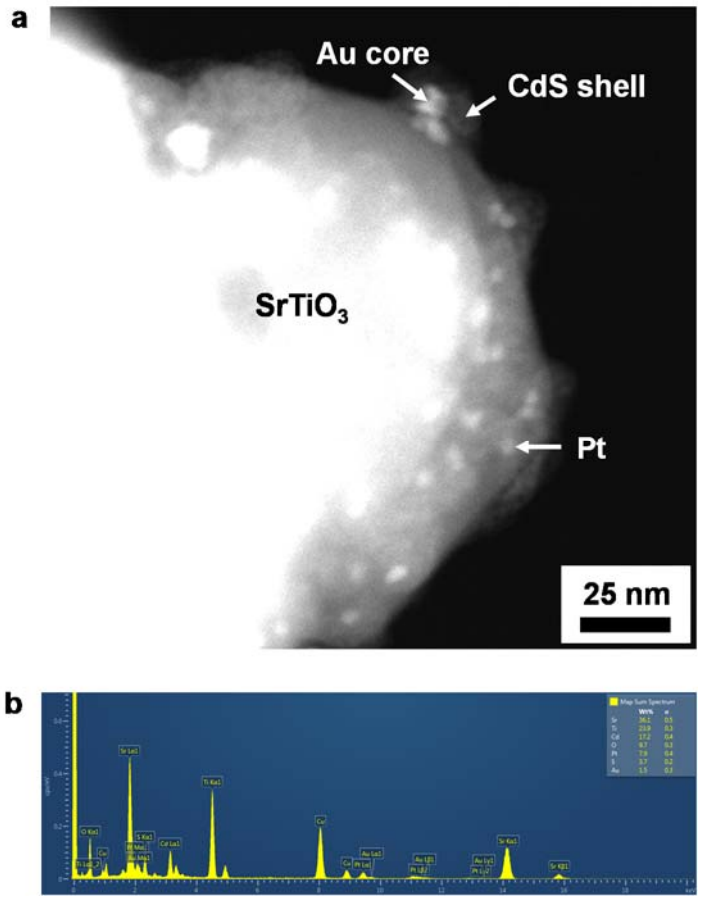

Figure 3.7 Morphological and compositional information of Au@CdS/Pt/$SrTiO_3$ nanostructure. (a) HAADF-STEM image of Au@CdS/Pt/$SrTiO_3$ nanostructure for which Pt nanoparticles were deposited on the surface of $SrTiO_3$, and (b) corresponding EDS spectrum.

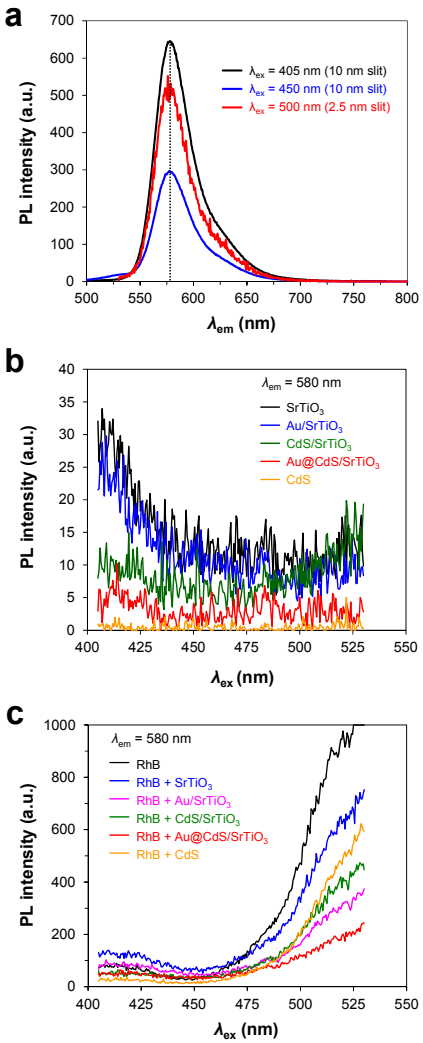

Figure 3.8 Steady-state PL spectra. (a) PL emission of 1 μM RhB where the excitation wavelength was at 405, 450, and 500 nm. (b) PL emission of the prepared samples in the absence of RhB solution as a function of the excitation wavelength. (c) PL emission of an aqueous solution of 1 μM RhB in the presence of each sample as a function of excitation wavelength where the emission wavelength is 580 nm.

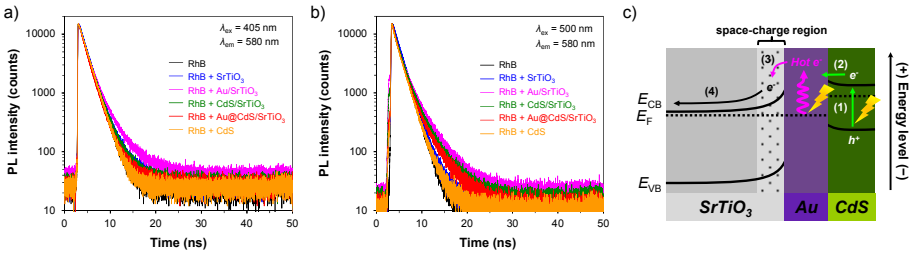

Figure 3.9 Visible-light-driven mechanism of the Au@CdS/$SrTiO_3$ nanostructure. Time-resolved PL spectra of 1 μM RhB in the presence of each sample with (a) excitation at 405 nm and (b) excitation at 500 nm where the emission wavelength is 580 nm. (c) Schematic energy band diagram of Au@CdS/$SrTiO_3$, showing the proposed electron-transfer processes across the three components responsible for H_2 production. The numbered arrows indicate the following individual electron-transfer steps: (1) Excitation of electrons in the CdS shell, (2) Electron injection from the CB of the CdS shell to Fermi level of the Au core, (3) Plasmon-induced hot electron injection from the Au core to the CB of $SrTiO_3$, (4) Migration of the hot electrons to active sites at the surface of $SrTiO_3$.

Table 3.1 Kinetic parameters extracted from the fitted results of time-resolved PL spectra of 1 μM RhB in the presence of each sample with 405 nm excitation.[a]

Entry in RhB	A_1	τ_1 (ns)	A_2	τ_2 (ns)	χ^2
None	12885.5	1.711	-	-	1.014
$SrTiO_3$	9335.9	1.608	713.1	3.568	1.033
$Au/SrTiO_3$	8521.5	1.505	1998.3	3.521	1.007
$CdS/SrTiO_3$	8907.0	1.384	3747.7	2.450	1.028
$Au@CdS/SrTiO_3$	10091.0	1.367	1928.6	2.661	1.001
CdS	11897.4	1.690	-	-	1.067

[a] The parameters were calculated using the software FluoFit.

Table 3.2 Kinetic parameters extracted from the fitted results of time-resolved PL spectra of 1 μM RhB in the presence of each sample with 500 nm excitation.[a]

Entry in RhB	A_1	τ_1 (ns)	A_2	τ_2 (ns)	χ^2
None	8255.4	1.711	-	-	1.061
$SrTiO_3$	8333.4	1.624	421.4	3.452	1.027
$Au/SrTiO_3$	5359.5	1.365	2813.5	3.334	1.039
$CdS/SrTiO_3$	6915.0	1.426	1899.4	3.404	1.013
$Au@CdS/SrTiO_3$	8134.0	1.235	2122.9	3.229	1.035
CdS	7834.1	1.704	-	-	1.055

[a] The parameters were calculated using the software FluoFit.

Table 3.3 Charge transfer models when the excitation wavelength is 405 nm.

Entry	Schematic charge transfer	Governing equations and solutions
RhB	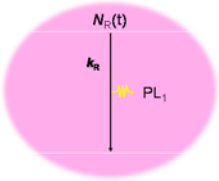	(1) $\frac{dN_R}{dt} = -k_R N_R$ $\rightarrow N_R = N_{R0} e^{-k_R t}$
RhB + $SrTiO_3$	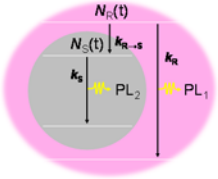	(1) $\frac{dN_R}{dt} = -(k_R + k_{R\rightarrow S}) N_R$ $\rightarrow N_R = N_{R0} e^{-(k_R + k_{R\rightarrow S})t}$ (2) $\frac{dN_S}{dt} = k_{R\rightarrow S} N_R - k_S N_S$ $\rightarrow N_S = C_1 e^{-(k_R + k_{R\rightarrow S})t} + C_2 e^{-k_S t}$ where $C_1 = \frac{k_{R\rightarrow S}}{k_S - (k_R + k_{R\rightarrow S})} \cdot N_{R0}$ and $C_2 = N_{S0} - C_1$
RhB + Au/$SrTiO_3$	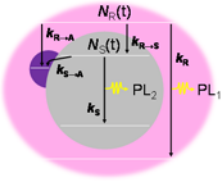	(1) $\frac{dN_R}{dt} = -(k_R + k_{R\rightarrow S} + k_{R\rightarrow A}) N_R$ $\rightarrow N_R = N_{R0} e^{-(k_R + k_{R\rightarrow S} + k_{R\rightarrow A})t}$ (2) $\frac{dN_S}{dt} = k_{R\rightarrow S} N_R - (k_S + k_{S\rightarrow A}) N_S$ $\rightarrow N_S = C_3 e^{-(k_R + k_{R\rightarrow S} + k_{R\rightarrow A})t} + C_4 e^{-(k_S + k_{S\rightarrow A})t}$ where $C_3 = \frac{k_{R\rightarrow S}}{(k_S + k_{S\rightarrow A}) - (k_R + k_{R\rightarrow S} + k_{R\rightarrow A})} \cdot N_{R0}$ and $C_4 = N_{S0} - C_3$
RhB + CdS/$SrTiO_3$	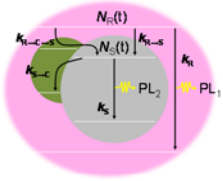	(1) $\frac{dN_R}{dt} = -(k_R + k_{R\rightarrow S} + k_{R\rightarrow C\rightarrow S}) N_R$ $\rightarrow N_R = N_{R0} e^{-(k_R + k_{R\rightarrow S} + k_{R\rightarrow C\rightarrow S})t}$ (2) $\frac{dN_S}{dt} = (k_{R\rightarrow S} + k_{R\rightarrow C\rightarrow S}) N_R - (k_S + k_{S\rightarrow C}) N_S$ $\rightarrow N_S = C_5 e^{-(k_R + k_{R\rightarrow S} + k_{R\rightarrow C\rightarrow S})t} + C_6 e^{-(k_S + k_{S\rightarrow C})t}$ where $C_5 - \frac{k_{R\rightarrow S} + k_{R\rightarrow C\rightarrow S}}{(k_S + k_{S\rightarrow C}) - (k_R + k_{R\rightarrow S} + k_{R\rightarrow C\rightarrow S})} \cdot N_{R0}$ and $C_6 = N_{S0} - C_5$
RhB + Au@CdS/$SrTiO_3$	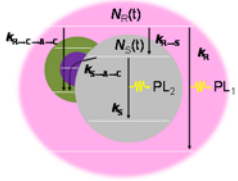	(1) $\frac{dN_R}{dt} = -(k_R + k_{R\rightarrow S} + k_{R\rightarrow C\rightarrow A\rightarrow C}) N_R$ $\rightarrow N_R = N_{R0} e^{-(k_R + k_{R\rightarrow S} + k_{R\rightarrow C\rightarrow A\rightarrow C})t}$ (2) $\frac{dN_S}{dt} = k_{R\rightarrow S} N_R - (k_S + k_{S\rightarrow A\rightarrow C}) N_S$ $\rightarrow N_S = C_7 e^{-(k_R + k_{R\rightarrow S} + k_{R\rightarrow C\rightarrow A\rightarrow C})t} + C_8 e^{-(k_S + k_{S\rightarrow A\rightarrow C})t}$ where $C_7 = \frac{k_{R\rightarrow S}}{(k_S + k_{S\rightarrow A\rightarrow C}) - (k_R + k_{R\rightarrow S} + k_{R\rightarrow C\rightarrow A\rightarrow C})} \cdot N_{R0}$ and $C_8 = N_{S0} - C_7$
RhB + CdS	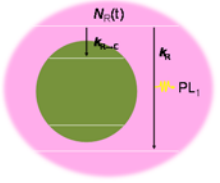	(1) $\frac{dN_R}{dt} = -(k_R + k_{R\rightarrow C}) N_R$ $\rightarrow N_R = N_{R0} e^{-(k_R + k_{R\rightarrow C})t}$

Table 3.4 Charge transfer models when the excitation wavelength is 500 nm.

Entry	Schematic charge transfer	Governing equations and solutions
RhB	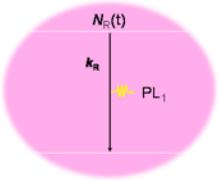	(1) $\frac{dN_R}{dt} = -k_R N_R$ $\rightarrow N_R = N_{R0} e^{-k_R t}$
RhB + $SrTiO_3$	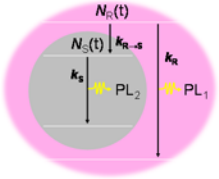	(1) $\frac{dN_R}{dt} = -(k_R + k_{R\rightarrow S}) N_R$ $\rightarrow N_R = N_{R0} e^{-(k_R + k_{R\rightarrow S})t}$ (2) $\frac{dN_S}{dt} = k_{R\rightarrow S} N_R - k_S N_S$ $\rightarrow N_S = C_1 e^{-(k_R + k_{R\rightarrow S})t} + C_2 e^{-k_S t}$ where $C_1 = \frac{k_{R\rightarrow S}}{k_S - (k_R + k_{R\rightarrow S})} \cdot N_{R0}$ and $C_2 = N_{S0} - C_1$
RhB + Au/$SrTiO_3$	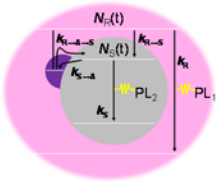	(1) $\frac{dN_R}{dt} = -(k_R + k_{R\rightarrow S} + k_{R\rightarrow A\rightarrow S}) N_R$ $\rightarrow N_R = N_{R0} e^{-(k_R + k_{R\rightarrow S} + k_{R\rightarrow A\rightarrow S})t}$ (2) $\frac{dN_S}{dt} = (k_{R\rightarrow S} + k_{R\rightarrow A\rightarrow S}) N_R - (k_S + k_{S\rightarrow A}) N_S$ $\rightarrow N_S = C_3 e^{-(k_R + k_{R\rightarrow S} + k_{R\rightarrow A\rightarrow S})t} + C_4 e^{-(k_S + k_{S\rightarrow A})t}$ where $C_3 = \frac{k_{R\rightarrow S} + k_{R\rightarrow A\rightarrow S}}{(k_S + k_{S\rightarrow A}) - (k_R + k_{R\rightarrow S} + k_{R\rightarrow A\rightarrow S})} \cdot N_{R0}$ and $C_4 = N_{S0} - C_3$
RhB + CdS/$SrTiO_3$	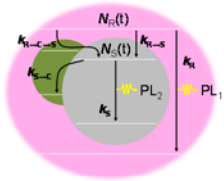	(1) $\frac{dN_R}{dt} = -(k_R + k_{R\rightarrow S} + k_{R\rightarrow C\rightarrow S}) N_R$ $\rightarrow N_R = N_{R0} e^{-(k_R + k_{R\rightarrow S} + k_{R\rightarrow C\rightarrow S})t}$ (2) $\frac{dN_S}{dt} = (k_{R\rightarrow S} + k_{R\rightarrow C\rightarrow S}) N_R - (k_S + k_{S\rightarrow C}) N_S$ $\rightarrow N_S = C_5 e^{-(k_R + k_{R\rightarrow S} + k_{R\rightarrow C\rightarrow S})t} + C_6 e^{-(k_S + k_{S\rightarrow C})t}$ where $C_5 = \frac{k_{R\rightarrow S} + k_{R\rightarrow C\rightarrow S}}{(k_S + k_{S\rightarrow C}) - (k_R + k_{R\rightarrow S} + k_{R\rightarrow C\rightarrow S})} \cdot N_{R0}$ and $C_6 = N_{S0} - C_5$
RhB + Au@CdS/$SrTiO_3$	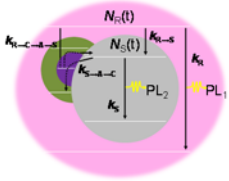	(1) $\frac{dN_R}{dt} = -(k_R + k_{R\rightarrow S} + k_{R\rightarrow C\rightarrow A\rightarrow S}) N_R$ $\rightarrow N_R = N_{R0} e^{-(k_R + k_{R\rightarrow S} + k_{R\rightarrow C\rightarrow A\rightarrow S})t}$ (2) $\frac{dN_S}{dt} = (k_{R\rightarrow S} + k_{R\rightarrow C\rightarrow A\rightarrow S}) N_R - (k_S + k_{S\rightarrow A\rightarrow C}) N_S$ $\rightarrow N_S = C_7 e^{-(k_R + k_{R\rightarrow S} + k_{R\rightarrow C\rightarrow A\rightarrow S})t} + C_8 e^{-(k_S + k_{S\rightarrow A\rightarrow C})t}$ where $C_7 = \frac{k_{R\rightarrow S} + k_{R\rightarrow C\rightarrow A\rightarrow S}}{(k_S + k_{S\rightarrow A\rightarrow C}) - (k_R + k_{R\rightarrow S} + k_{R\rightarrow C\rightarrow A\rightarrow S})} \cdot N_{R0}$ and $C_8 = N_{S0} - C_7$
RhB + CdS	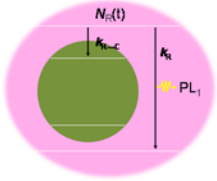	(1) $\frac{dN_R}{dt} = -(k_R + k_{R\rightarrow C}) N_R$ $\rightarrow N_R = N_{R0} e^{-(k_R + k_{R\rightarrow C})t}$

Table 3.5 Rate constants for charge transfer with 405 nm and 500 nm excitation.

Rate constants	405 nm excitation	500 nm excitation
k_{R}	$5.84 \times 10^{8}\ s^{-1}$	$5.84 \times 10^{8}\ s^{-1}$
$k_{R\rightarrow S}$	$0.38 \times 10^{8}\ s^{-1}$	$0.32 \times 10^{8}\ s^{-1}$
$k_{R\rightarrow A}$ (405 nm)	$0.42 \times 10^{8}\ s^{-1}$	-
$k_{R\rightarrow A\rightarrow S}$ (500 nm)	-	$1.17 \times 10^{8}\ s^{-1}$
$k_{R\rightarrow C\rightarrow S}$	$1.01 \times 10^{8}\ s^{-1}$	$0.85 \times 10^{8}\ s^{-1}$
$k_{R\rightarrow C\rightarrow A\rightarrow C}$ (405 nm)	$1.10 \times 10^{8}\ s^{-1}$	-
$k_{R\rightarrow C\rightarrow A\rightarrow S}$ (500 nm)	-	$1.94 \times 10^{8}\ s^{-1}$
$k_{R\rightarrow C}$	$0.08 \times 10^{8}\ s^{-1}$	$0.03 \times 10^{8}\ s^{-1}$
k_{S}	$2.80 \times 10^{8}\ s^{-1}$	$2.90 \times 10^{8}\ s^{-1}$
$k_{S\rightarrow A}$	$0.04 \times 10^{8}\ s^{-1}$	$0.10 \times 10^{8}\ s^{-1}$
$k_{S\rightarrow C}$	$1.28 \times 10^{8}\ s^{-1}$	$0.04 \times 10^{8}\ s^{-1}$
$k_{S\rightarrow A\rightarrow C}$	$0.96 \times 10^{8}\ s^{-1}$	$0.20 \times 10^{8}\ s^{-1}$

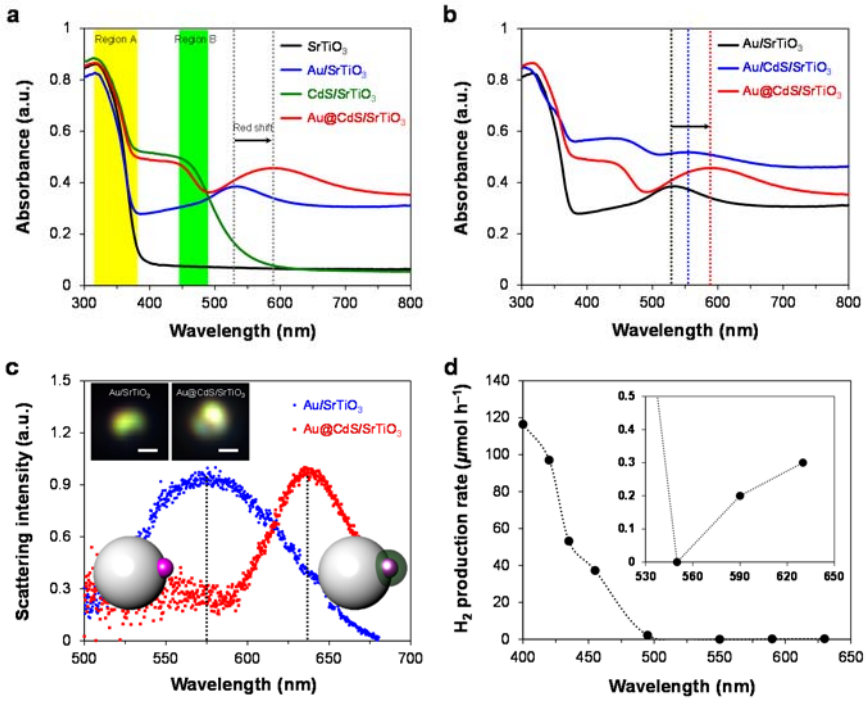

Figure 3.10 Optical properties and wavelength-dependent H_2 production. (a) UV-vis absorbance where two shoulders at Region A (yellow) and Region B (green) are attributed to bare $SrTiO_3$ and the CdS shell, respectively. The broad peaks result from LSPR of Au nanoparticles. (b) UV-vis absorbance of the samples containing Au nanoparticles. Three vertical lines at 530, 550, and 590 nm indicate Au plasmon band of $Au/SrTiO_3$, $Au/CdS/SrTiO_3$, and $Au@CdS/SrTiO_3$, respectively. Red-shift of Au plasmon band for $Au/CdS/SrTiO_3$ is less than that for $Au@CdS/SrTiO_3$. (c) Dark-field scattering spectra and the corresponding typical dark-field images in which the scale bar represents 250 nm. (d) H_2 production rate using 0.05 g of the $Au@CdS/Pt/SrTiO_3$ catalyst as a function of wavelength. The inset shows the H_2 production rate in the wavelength range of 550 to 630 nm.

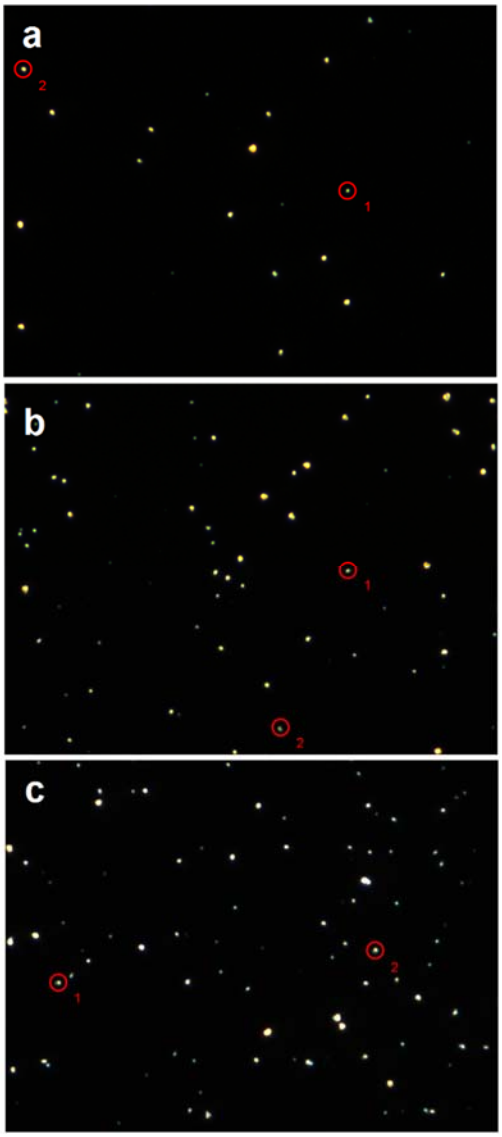

Figure 3.11 Dark-field scattering images. A large field of view (88 μm × 66 μm) for (a) bare $SrTiO_3$, (b) Au/$SrTiO_3$, and (c) Au@CdS/$SrTiO_3$. Red circles indicate the selected spots to obtain the scattering spectra.

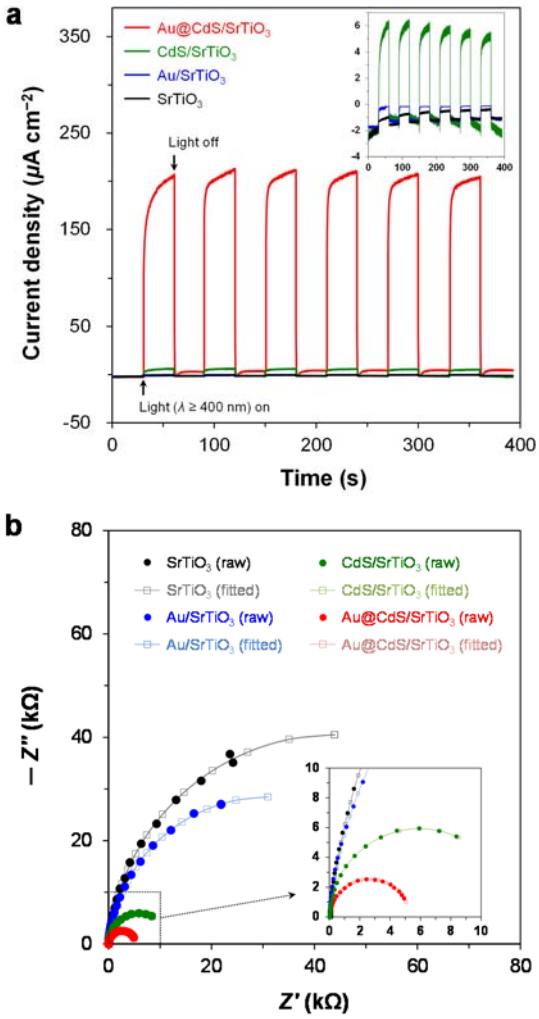

Figure 3.12 Photoelectrochemical performance of the Au@CdS/$SrTiO_3$ photoanode. (a) Chronoamperometric *I–t* curves at an applied potential of 0 V under irradiation by visible light ($\lambda \geq 400$ nm) with 30 s on/off cycles of the light. (b) Nyquist plots obtained by applying a sine wave with an amplitude of 5 mV over the frequency range from 1 MHz to 50 mHz.

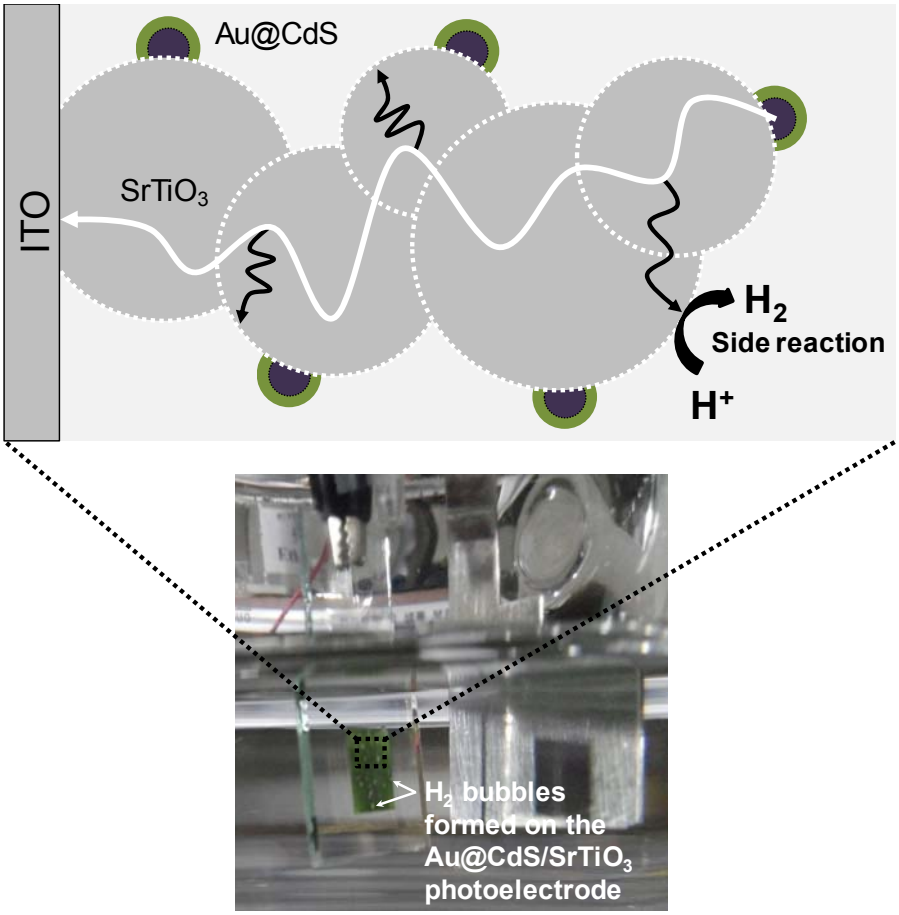

Figure 3.13 Schematic drawing of the electron pathways through nanoparticulate Au@CdS/$SrTiO_3$ on the ITO circuit. A 3D random walk of electrons increases the possibility to react with H^+ (side reaction, $2H^+ + 2e^- \rightarrow H_2$) on the surface of $SrTiO_3$, and as result decreasing the electron collection at the ITO circuit.

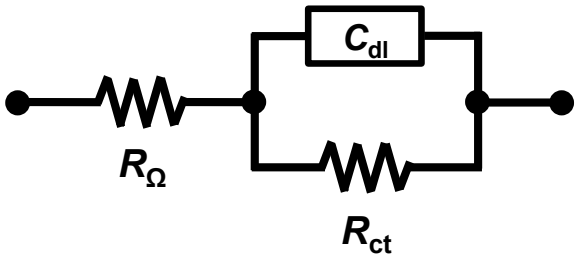

Figure 3.14 Electrochemical impedance spectroscopy. An equivalent circuit for interface between photoanode and electrolyte which described the electrical response of the electrode. R_{Ω}: bulk electrolyte resistance, C_{dl}: double-layer capacitance, R_{ct}: charge-transfer resistance.

Table 3.6 Kinetic parameters extracted from fitted results of EIS spectra.[a]

	R_{Ω} (Ω)	Q_0 ($Ssec^n$)	n	R_{ct} (kΩ)
$SrTiO_3$	83.9	3.4×10^{-5}	0.950	87.7
$Au/SrTiO_3$	15.8	4.8×10^{-5}	0.947	61.9
$CdS/SrTiO_3$	24.6	4.7×10^{-5}	0.970	11.0
$Au@CdS/SrTiO_3$	31.4	6.2×10^{-5}	0.976	5.3

[a] The parameters were calculated using the software ZMAN 2.2.

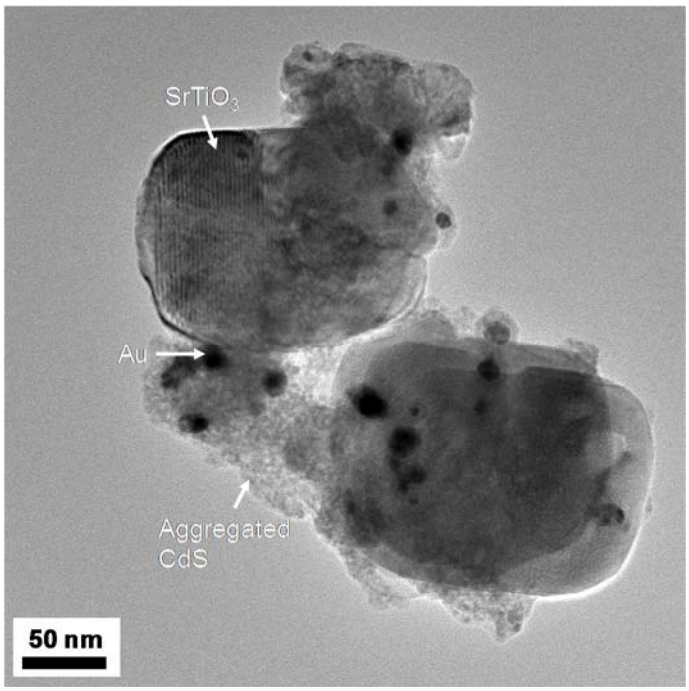

Figure 3.15 Shading effect. TEM image of 2 wt% Au loaded Au@CdS/$SrTiO_3$ shows that CdS shell was aggregated around the Au cores.

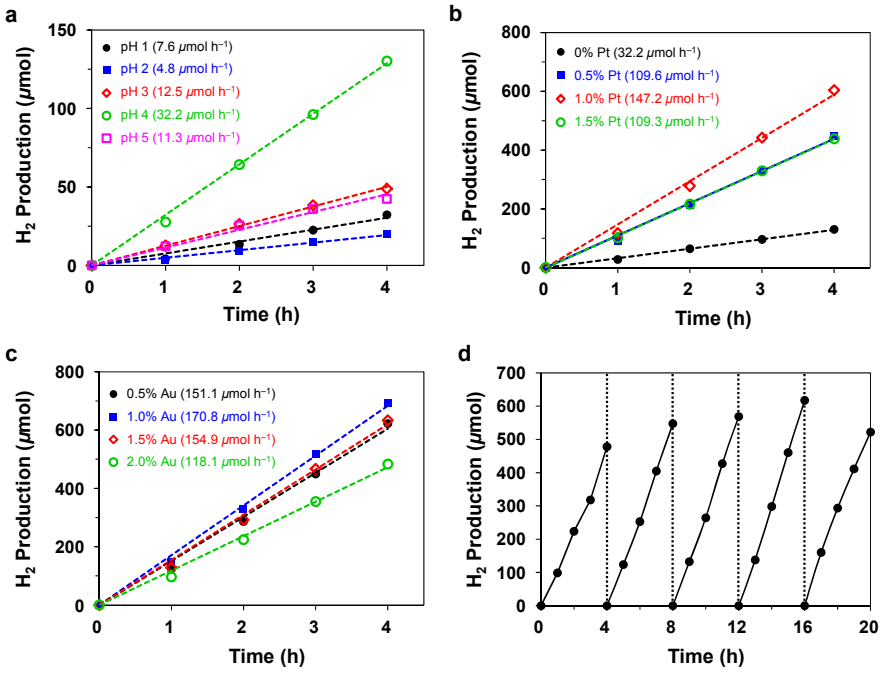

Figure 3.16 Optimization for preparation conditions of Au@CdS/Pt/$SrTiO_3$ nanostructure and photocatalytic stability. Photocatalytic H_2 production as a function of (a) the pH of $SrTiO_3$ suspension when 1 wt% Au cores were deposited on $SrTiO_3$, (b) Pt concentrations when Pt nanoparticles were deposited on $SrTiO_3$ at pH 4, (c) Au concentrations when Au cores were deposited on 1 wt% Pt/$SrTiO_3$ at pH 4. (d) Recycled H_2 production of the Au@CdS/Pt/$SrTiO_3$ under irradiation of a wavelength longer than 400 nm for 20 h.

Chapter 4. Energy Conversion of Sub-Band-Gap Light using Carbon Nanodots and Rhodamine B

4.1 Introduction

Fluorescent carbon nanodots (C-dots) have emerged as an effective spectral upconverter due to their fascinating features such as excitation wavelength, λ_{ex}, dependent PL behavior, quantum-confinement effect, physicochemical stability, biocompatibility, and water solubility [84–86]. The origin of the PL emission of C-dots has been assigned to two classes of fluorescence emission: (1) sp^2 carbon domains embedded in an sp^3 carbon matrix have a suitable emission bandgap and thus can emit PL in the UV to visible range or even NIR by radiative recombination of electron–hole pairs [87–89]; (2) the radiative recombination of excitons located at surface energy traps that arise from surface defective sites produces PL emission [90,91]. As-synthesized C-dots are extensively used in conjunction with semiconductor-based photocatalysts for applications in environmental and energy areas [92–101]. The hybrid materials not only enhance optical absorption in the UV–visible region, but also suppress the recombination of photoexcited electron–hole pairs, thereby increasing the overall

photocatalytic activity. However, photon upconversion efficiency using C-dots is still too low to effectively harvest the full spectrum of sunlight.

Herein, I report on an effective fluorescence system consisting of three components so as to manipulate frequencies of sub-band-gap light via a fluorescence resonance energy transfer (FRET)-assisted upconversion process. In this system, RhB with a high molar extinction coefficient was coupled to naked C-dots (NC-dots) as an electron/energy-transfer mediator. The spectral overlap between the emission of RhB and the absorption of NC-dots caused the FRET from the excited RhB to the NC-dots, thereby increasing the upconverted PL intensity of the NC-dots. The upconverted photons were subsequently consumed to sensitize Ag_3PO_4 particles, which was used as an acceptor of the upconverted light in this fluorescence system due to its proper bandgap, E_g, and band structure. The findings were fundamentally confirmed by steady-state and time-resolved PL spectroscopies.

4.2 Experimental

4.2.1 Sample Preparation

$AgNO_3$ (0.6 g, Sigma-Aldrich) was dissolved in DI water of 10 mL. A 30 mL aliquot of an ethanol solution of oleic acid (0.03 M, Samchun) was then mixed with the aqueous solution of $AgNO_3$. After stirring for 1 h, 50 mL of a 0.1 M Na_2HPO_4 aqueous solution was slowly added to the mixture to form the yellow Ag_3PO_4 and then stirred for 3 h. The resulting mixture was placed in a Teflon-lined autoclave and heated at 150 °C for 12 h. The yellow precipitate was isolated by centrifugation, washed several times with DI water, and then dried at 60 °C overnight. For the formation of NC-dots on the surface of the Ag_3PO_4, the resulting powder was placed in a furnace under an N_2 atmosphere at 220 °C (5 °C min^{-1}) and calcined for 10 min. Bare Ag_3PO_4 as a control sample was prepared by an ion-exchange method. $AgNO_3$ (0.6 g) was dissolved in DI water of 30 mL, and then 50 mL of 0.1 M Na_2HPO_4 aqueous solution was added dropwise into the $AgNO_3$ solution. A yellow Ag_3PO_4 powder was obtained after stirring for 3 h followed by centrifugation.

4.2.2 Sample Characterization

Particle sizes and surface morphology were observed by field emission scanning electron microscope (FESEM, Auriga, Carl Zeiss) after a sputter

deposition process to cover a specimen with a thin layer of Pt and transmission electron microscopy (TEM, Tecnai F20, Philips) operating at 200 kV. The crystal structures were examined by X-ray diffractometer (XRD, D/Max-2500, Rigaku) with Cu Kα radiation (λ = 0.154 nm) as the incident beam at 50 kV and 100 mA. Absorbance spectra were obtained by a UV-vis spectrophotometer (V670, Jasco) in diffuse reflectance mode with $BaSO_4$ as a reference. C 1s and Ag 3d spectra of bare Ag_3PO_4 and NC-dots/Ag_3PO_4 nanoparticles were obtained by XPS (Sigma Probe, Thermo) where the binding energy was corrected with reference to the C 1s peak of 284.5 eV for each sample. The carbon content was determined by CHNS elemental analyzer (TruSpec Micro CHNS, LECO). The thermogravimetric analysis (TGA) was performed with simultaneous DSC/TGA (Q600, TA instruments) at a heating rate of 10 °C min^{-1} from room temperature to 700 °C in N_2 flow of 100 mL min^{-1} where all the samples (50 mg) were preheated at 120 °C for 2 h to remove physisorbed water. FTIR spectra were acquired using a Nicolet 6700 spectrophotometer (Thermo Scientific) using an attenuated total reflectance (ATR). Raman spectroscopy was performed on a T64000-HORIABA Jobin Yvon equipped with a multichannel charge-coupled device (CCD) detector where excitation source used a 514 nm Ar laser.

4.2.3 Photoluminescence Spectroscopy

Steady-state PL was measured with a PerkinElmer LS55 spectrophotometer (PerkinElmer Ltd., Beaconsfield) equipped with a Xe

lamp where cut-off filters were inserted into the fluorimeter to remove the normal fluorescence excited by the leaking component from the second diffraction of the excitation source. The measurements were replicated three times in total to obtain average values. Time-resolved PL decay curves were obtained via time-correlated single photon counting (TCSPC) methods using a Fluo-Time 200 instrument (Picoquant, Germany). The excitation sources used a 500 nm pulsed diode laser (pulse energy = 10 pJ; FWHM < 54 ps) with the repetition rate of 80 MHz, and a 550 nm cut-off filter was placed between the monochomator and the sample to eliminate the second-order diffraction light. The signals were collected at the excitonic emission of 0.1 μM RhB (Sigma, for fluorescence, λ_{em} = 580 nm). The temperature of quartz cuvette was maintained at 20 °C by circulating water through an external temperature control device during the PL measurements. The efficiency, η, of the FRET process was estimated from lifetime measurements of the donor in the absence and presence of an acceptor using the following equation [102],

$$\eta\,(\%) = \left(1 - \frac{\tau_{DA}}{\tau_D}\right) \times 100 \qquad (4\text{-}1)$$

where τ_{DA} is the lifetime of the donor in the presence of an acceptor, and τ_D is the lifetime of the donor in the absence of an acceptor. The presence of an acceptor results in a decrease in the lifetime of the donor.

4.2.4 Photocatalytic Activities

Photocatalytic activity was evaluated by analyzing the degradation of 10 ppm RhB and 10 ppm methylene blue (MB) after adding the photocatalyst (0.15 g) to a 100 mL solution. The photodegradation tests were carried out by using a 300 W Xe lamp with a 500 nm longpass filter. Before irradiation, RhB and MB solutions in the presence of photocatalyst was stirred in the dark for 1 h to be reached adsorption–desorption equilibrium. The reaction temperature was maintained by circulating a coolant connected to a water-jacketed reservoir at 20 °C. A 1 mL aliquot of the suspension was filtered using a disposable syringe filter at hourly intervals. The degree of photodegradation was calculated by measuring the maximum absorbance of RhB and MB at 554 nm and 665 nm, respectively.

4.2.5 Photoelectrochemical Performance Characterization

Chronoamperometric measurements were performed on the computer-controlled potentiostat (ZIVE SP2, WonATech) using a two-electrode cell. The powdered photocatalysts were immobilized on a stainless steel plate (2.5 cm × 2.0 cm) using a doctor blade. A Pt plate was used as the counter electrode in an aqueous solution of 0.1 M $NaClO_4$ as a supporting electrolyte and 0.1 μM RhB at $\lambda_{ex} > 500$ nm. EIS experiments were conducted with an applied potential of 0 V under an ac perturbation signal of 5 mV over the frequency range of 1 MHz to 30 mHz. The impedance spectra were interpreted using commercial software ZMAN 2.2. The temperature in PEC system was maintained at 20 °C by circulating coolant through an external

temperature control device during the PEC experiments. The external quantum efficiency (EQE), the ratio of the number of collected electrons to the number of incident photons, was calculated using the following equation,

$$\text{EQE}\ (\%) = \frac{J / e}{I / h\nu} \times 100 \qquad (4\text{-}2)$$

where J is the current density in A cm^{-2}, e is the charge of one electron (1.602×10^{-19} C), and I is the incident photon power density (1 mW cm^{-2}) which is measured by an optical power meter (Nova, Ophir) in the wavelength range of 500 to 800 nm. $h\nu$ is the energy of one photon (3.056×10^{-19} J) at average wavelength, 650 nm. All photons are assumed to be absorbed in the photocatalyst. The spectral distribution of the 300W Xe lamp (model 6258, Newport Corporation) without any filter is nearly featureless over the entire visible range [72].

4.3 Results and Discussion

4.3.1 Catalyst Characterization

Ag_3PO_4 material was used as a support of NC-dots to absorb the upconverted light and generate electrons in this study. NC-dots were grown on the surface of the Ag_3PO_4 through a bottom-up synthetic route, which is schematically shown in **Figure 4.1a**. The detailed experimental procedures are given in the Experimental Section. Briefly, Ag_3PO_4 was prepared by a modified ion-exchange method in the presence of oleic acid, as the source of NC-dots (**Figure 4.1b**). The negatively charged carboxyl groups of oleic acid were adsorbed on the positively charged surface of the Ag_3PO_4 below its potential of zero charge (PZC), pH 6.65 (**Figure 4.1c**) [103]. Hydrothermal carbonization at 150 °C transformed the oleic acid into C-dots on the Ag_3PO_4 surface (**Figure 4.1d**). Finally, the resulting powder was annealed at 220 °C for 10 min in a flow of N_2, leading to the formation of NC-dots through the thermal decomposition of the residual organics on the surface of Ag_3PO_4 which also increased the population of NC-dots (**Figure 4.1e**). The contents of the NC-dots were determined to be 2 wt % by a CHNS elemental analyzer. The annealing temperature used to form NC-dots on the Ag_3PO_4 surface was determined by TGA as a function of increasing temperature in a N_2 flow. As shown in **Figure 4.2**, the adsorbed oleic acid thermally decomposes into NC-dots, which begin to be formed at 220 °C and are burned out with the lattice oxygen of Ag_3PO_4 at an elevated

temperature (> 320 °C). **Figure 4.3** reveals FTIR spectra of the prepared samples at each step. After the hydrothermal carbonization, the hydrocarbon chains of the oleic acid remained on the surface of the Ag_3PO_4, as evidenced by the large C–H stretching peaks observed at 2922 and 2851 cm^{-1}. These structures were largely removed from the surface by thermal decomposition in the N_2 flow, as evidenced by the disappearance of C–H, C=O, and C–O–H stretching peaks. The crystalline structure of Ag_3PO_4 was well maintained in the absence of any other crystalline phases, even after the hydrothermal and annealing procedures, as confirmed from XRD patterns (**Figure 4.4a**). **Figure 4.4b** indicates the existence of two binding energies for Ag 3d5/2 and Ag 3d3/2 photoelectrons at 367.8 and 373.8 eV, with a difference of 6.0 eV, which is in agreement with reported values for Ag^+ [104,105]. The TEM image of **Figure 4.1f** shows NC-dots with a diameter of 3.4 ± 0.9 nm (see **Figure 4.5**) where the NC-dots were obtained by selectively melting the Ag_3PO_4 of the NC-dots/Ag_3PO_4 using HNO_3. The HRTEM image of a NC-dot in **Figure 4.1g** shows a high degree of crystallinity with a hexagonal honeycomb structure containing zigzag and armchair edges of sp^2 graphitic carbon. The angle between two adjacent edges is equal to 90°. Note that the angles between the zigzag and armchair edges can be 30°, 90°, or 150° [106]. In the line intensity profiles along each axis (**Figures 4.6a,b**), the average distances between the two peaks are 0.233 nm and 0.145nm, consistent with literature values for interatomic distances between the two next-nearest carbon atoms along the zigzag orientation (0.24 nm) and the nearest-neighbor carbon atoms along the armchair orientation (0.14 nm),

respectively [107–109]. The fast Fourier transform (FFT) pattern, inset, of the HRTEM image also confirms the existence of a graphitic structure and the bond lengths of the NC-dots. The red lines connecting the symmetrical pairs of dots on the inner circle were perpendicular to the zigzag direction, and the blue lines on the outer circle were perpendicular to the armchair direction. The existence of a graphitic structure was further confirmed by an sp^2 carbon fraction observed in the C 1s XPS spectrum as well as by the low intensity ratio (I_D/I_G = 0.59) of the D band at 1338 cm^{-1} and G band at 1577 cm^{-1} in Raman spectra (**Figures 4.7a,b**).

4.3.2 Optical Properties

The as-synthesized NC-dots/Ag_3PO_4 nanocomposite exhibits a substantial enhancement in the absorption of UV and even visible light as compared to bare Ag_3PO_4, which has an E_g of 2.5 eV (**Figure 4.8a**). The spectrum shows one shoulder and a long tail absorption band. One shoulder, observed at around 500 nm, is assigned to bare Ag_3PO_4, and the long tail absorption in the entire visible range is attributed to the presence of NC-dots. UV–vis absorption spectrum of NC-dots suspended in water also shows a tail extending into the visible range, with two characteristic peaks centered at 227 nm and 300 nm for a $\pi \rightarrow \pi^*$ transition of aromatic sp^2 domains and for an $n \rightarrow \pi^*$ transition of C=O, respectively [110,111]. The aqueous solution of RhB molecules with a high molar extinction coefficient ($\varepsilon = 8.7 \times 10^4$ M^{-1} cm^{-1} at 554 nm) absorbs in the wavelength range of 450–600 nm, and

strongly emit PL in the wavelength range of 500–700 nm at λ_{ex} = 500 nm [112]. The spectral overlap between the emission of RhB and the absorption of NC-dots permits the generation of FRET from the excited RhB to the NC-dots when the RhB/NC-dots fluorescence system is irradiated by λ_{ex} > 500 nm. **Figure 4.8b** represents an attractive feature of NC-dots in which its PL emission peaks shift to 150 nm longer wavelengths (downconversion region) as the λ_{ex} increases from 400 nm to 650 nm, and shift to 150 nm shorter wavelengths (upconversion region) as the λ_{ex} increases from 500 nm to 750 nm. In these PL results, the second-order diffraction light was excluded by using cut-off filters, which eliminate intrinsic normal PL. Whereas the peak emission of RhB is at 580 nm regardless of λ_{ex}, its PL intensity depends on λ_{ex} (see **Figure 4.9**). In particular, the PL intensity of RhB increases exponentially at λ_{ex} > 500 nm. Therefore, when the RhB/NC-dots fluorescence system is irradiated with λ_{ex} > 500 nm, the NC-dots can additionally absorb the strong PL emission of RhB molecules through FRET and then emit the upconverted light with a wavelength longer than 350 nm. Furthermore, the FRET effect increases the upconverted light intensity of the NC-dots due to the FRET property that leads to a reduction in the fluorescence emission of the donor and an increase in the fluorescence emission intensity of the acceptor. For these reasons, the RhB/NC-dots fluorescence system was combined with Ag_3PO_4 as an absorber of the upconverted light. The Ag_3PO_4 photocatalyst hardly uses light longer than 500 nm. However, it exhibits extremely high activities with ~80% of the apparent quantum efficiency in the visible region of 400–480 nm [113].

4.3.3 FRET-Assisted Upconversion Enhancement

Figure 4.8c shows plots of the concentration of 10 ppm MB and 10 ppm RhB as a function of time at λ_{ex} > 500 nm, from which it is possible to observe the synergistic effect of RhB molecules and NC-dots. Note that RhB is well known to be a more non-degradable dye than MB because it contains more aromatic rings and alkyl groups than MB. The NC-dots/Ag_3PO_4 system decomposed MB at a rate of 0.19 h^{-1}, which was twice as fast as the rate (0.1 h^{-1}) determined for bare Ag_3PO_4 due mainly to the enhanced charge separation caused by the excitation of NC-dots. Although the PL of MB in the range of 650–800 nm is upconverted to 500–650 nm through NC-dots, the energy of upconverted PL is beyond its capacity to work Ag_3PO_4. Notably, the NC-dots/Ag_3PO_4 system showed an impressive degradation rate (0.18 h^{-1}) for RhB, which was 9 times faster than the rate (0.02 h^{-1}) for bare Ag_3PO_4 and was even similar to the decomposition rate of MB using NC-dots/Ag_3PO_4. This remarkable increase was responsible for the FRET-assisted upconversion process. That is, highly luminescent RhB molecules absorb the incident light and then transfer their energy to NC-dots via FRET. The FRET effect helps NC-dots generate additional electron–hole pairs, thus increasing their fluorescence emission intensity. As a result, the NC-dots emit light with a wavelength longer than 350 nm as a result of the enhanced upconversion by FRET, and these upconverted photons are consumed by Ag_3PO_4 particles for sensitization. In addition, NC-dots promoted the

adsorption of RhB molecules through strong π–π stacking and anion–cation interactions between the aromatic rings of RhB and sp^2-hybridized carbons (**Figure 4.10**) [114], facilitating the FRET from RhB molecules to NC-dots. In contrast, the C-dots/Ag_3PO_4 catalyst prepared by hydrothermal carbonization has an adverse effect on the adsorption of RhB molecules and eventually slows down reaction rate for its decomposition due to the presence of insulating molecules on the surface of catalyst (**Figure 4.11**). The gradual wavelength shift toward the blue region of the RhB absorption band depicted in **Figure 4.12** is caused by the successive de-ethylation of RhB because of attack by one of the reactive oxygen species on the N-ethyl group. This result indicates that heterogeneous photocatalysis occurs simultaneously with the photosensitization process [115,116].

Figures 4.13a,b display the steady-state PL spectra of RhB and MB solutions in the presence of Ag_3PO_4 and NC-dots/Ag_3PO_4 as a function of λ_{ex} where the PL contribution of Ag_3PO_4 is excluded. As shown in **Figures 4.14a,b**, the PL of bare Ag_3PO_4 suspended in water exhibits a broad emission at around the λ_{ex} range of 500–600 nm, which originates from the surface oxygen vacancies [117,118]. The emission intensity of the NC-dots/Ag_3PO_4 suspended in water is obviously quenched as compared with that of bare Ag_3PO_4, indicating that the incorporation of NC-dots can inhibit the recombination of charge carriers. The quenching effect can be explained in terms of the interfacial charge transfer between NC-dots and Ag_3PO_4. Therefore, the introduction of NC-dots into Ag_3PO_4 particles is favorable for separating photoexcited electron–hole pairs. The enhanced charge separation

lengthens the lifetime of the charge carriers, thereby improving photocatalytic performance. The second-order diffraction light was also eliminated by inserting a cut-off filter into the fluorimeter. The colloidal Ag_3PO_4 in the RhB solution caused a depression in the peak emission of RhB due to the electron transfer from the excited RhB to the CB of Ag_3PO_4. The PL emission of RhB was more severely quenched after NC-dots were deposited on the surface of Ag_3PO_4, indicating that the photoexcited electrons of RhB were transferred to the CB of Ag_3PO_4 and further to the LUMO level of the excited NC-dots. The PL emission of the MB solution also was suppressed by Ag_3PO_4, and it was more pronounced by NC-dots/Ag_3PO_4 nanocomposite. However, the PL quenching behaviors of RhB and MB showed a distinct difference at $\lambda_{ex} > 500$ nm. While the gap for the PL quenching of RhB between bare Ag_3PO_4 and NC-dots/Ag_3PO_4 gradually became wider with increasing λ_{ex} in this range, the gap of MB became narrowing even after introduction of NC-dots on Ag_3PO_4. The improved quenching of RhB by NC-dots/Ag_3PO_4 can be attributed to a favorable charge transfer between the two interfaces of RhB, NC-dots, and Ag_3PO_4. Specifically, the excited RhB transferred its energy to the NC-dots via FRET, followed by the upconverted light emission of NC-dots with the sensitization of Ag_3PO_4, thereby forming an energy cascade for a favorable electron transfer, RhB → NC-dots → Ag_3PO_4, consequently improving the charge separation.

4.3.4 Energy Conversion of Sub-Band-Gap Light

The RhB/NC-dots/Ag_3PO_4 system was used for photon-to-electron conversion in a PEC cell (**Figure 4.8d**). No photocurrent was recorded for the bare Ag_3PO_4 and RhB/Ag_3PO_4 system at an applied potential of 0 V under irradiation of $\lambda_{ex} > 500$ nm because Ag_3PO_4 can only be excited by $\lambda_{ex} < 500$ nm. A photocurrent response of ~35 nA cm^{-2} (EQE = 0.007%) was observed on NC-dots/Ag_3PO_4 photoanode, despite the poor sensitivity of Ag_3PO_4 to $\lambda_{ex} > 500$ nm. The photocurrent density of the NC-dots/Ag_3PO_4 photoanode increased by around 18 times (~630 nA cm^{-2}, EQE = 0.12%) after RhB was added to the electrode system, indicating that the separation efficiency of electron–hole pairs was improved through the electronic interaction between the RhB and the NC-dots. The starting current gradually decreased to ~60% of the initial current upon light on, which can be attributed to the oxidative degradation of RhB molecules in the vicinity of the NC-dots/Ag_3PO_4 photoanode through the photosensitizing process.

To further characterize the designed photoelectrodes, I carried out EIS measurements at $\lambda_{ex} > 500$ nm, which are shown in the form of Nyquist plots (**Figure 4.15**). An equivalent circuit for the PEC reaction was designed with a serial combination of the bulk electrolyte resistance, R_Ω, and the interfacial reaction impedance that is represented by a parallel combination of double layer capacitance, C_{dl}, and the charge-transfer resistance, R_{ct}, as shown in the inset. In this circuit, the CPE can replace C_{dl} at the electrode–electrolyte interface. The impedance of the CPE, Z_{CPE}, is given as follows [11],

$$Z_{CPE} = \frac{1}{Q_0(jw)^n} \tag{4-3}$$

where Q_0 is the admittance magnitude of the CPE, and n is the exponent related to the phase angle φ by $\varphi = n(\pi/2)$. The kinetic parameters extracted from the impedance measurements were calculated with the equivalent circuit, and the results are summarized in **Table 4.1**. The R_{ct} of NC-dots/Ag_3PO_4 decreased by a factor of ~0.6 after RhB was added into the electrode system (14.6 kΩ → 8.3 kΩ). The reduced R_{ct} explains why the RhB/NC-dots/Ag_3PO_4 system increases the photocurrent density in the long visible-light region.

4.3.5 Insights into the FRET-Assisted Upconversion Process

Time-resolved PL measurements were performed to investigate the electron-transfer kinetics of the RhB/NC-dots/Ag_3PO_4 system in which 500 nm laser pulses were used to excite the RhB with NC-dots, and a 550 nm cut-off filter was inserted to remove the second-order diffraction light. The PL decay traces were collected at 580 nm, a wavelength that contains the PL emission of RhB and Ag_3PO_4. Note that NC-dots hardly emit PL at 580 nm when irradiated by λ_{ex} = 500 nm. **Figure 4.16a** shows PL lifetime decay curves for RhB in the presence of Ag_3PO_4 and the NC-dots/Ag_3PO_4. The resulting decay curves were fitted with a following multi-exponential model,

$$I(t) = \sum_{i=1}^{n} A_i e^{-t/\tau_i} \tag{4-4}$$

where A_i and τ_i indicate the amplitude and the decay time of *i* component, respectively. *n* is the number of individual fluorescence. The intensity is assumed to be the sum of the individual single exponential decays. Kinetic parameters were extracted from the fitting results of the time-resolved PL curves and equation 5-4, and the resulting parameters are summarized in **Table 4.2**. The value of χ^2 was used to judge the goodness-of-fit. The intensity decay of pure RhB was found to be a single exponential function (*n* = 1). The decay traces for RhB containing Ag_3PO_4 could be fit to a bi-exponential function (*n* = 2) because the PL emission at 580 nm is attributed to both RhB and Ag_3PO_4. The obtained time-resolved spectra can be a sum of PL_R (PL of RhB) and PL_A (PL of Ag_3PO_4). Therefore, the pre-exponential factors A_i can be considered as the fractional contribution of PL_R and PL_A. The A_1 value for pure RhB decreased by 16.8% and by 36.8% in the presence of Ag_3PO_4 and NC-dots/Ag_3PO_4, respectively. After the introduction of NC-dots, the A_2 value was 4.6 times higher than that of bare Ag_3PO_4. This is consistent with the FRET property that simultaneously increases the emission intensity of acceptor and the emission quenching of donor. The τ_1 and τ_2 in the exponential terms describe the decay time of $N_R(t)$ and $N_A(t)$ on the obtained time-resolved PL spectra, respectively. $N_R(t)$ and $N_A(t)$ refer to the time-dependent electron populations in the LUMO of RhB and the CB of Ag_3PO_4, respectively. As shown in **Figures 4.17a–c**, decay pathways of the excited electrons were constructed, based on the results of the steady-state PL spectroscopy, in an attempt to understand the kinetics of the process. In the schematic, R, A, and C denote RhB, Ag_3PO_4, and NC-dots,

respectively. Corresponding differential equations were developed as a charge-transfer model to calculate the rate constants, and these equations are summarized in **Table 4.3**. The rate constants for interfacial electron transfer and charge recombination can be calculated by comparing the exponents, k, of the model equations with the kinetic parameters τ_i [11,35]. The resulting rate constants are summarized in **Table 4.4**. For example, the recombination rate constant of pure RhB, k_R, was expressed by a reciprocal of τ_1 (1.722 ns). Its value was found to be 5.81×10^8 s^{-1}, which was quite close to the previously reported values [11,35]. RhB in the presence of Ag_3PO_4 revealed two fitted components of τ_1 (1.673 ns) and τ_2 (3.036 ns). Since the short decay time was a reciprocal of $k_R + k_{R\rightarrow A}$ where $k_{R\rightarrow A}$ is the rate constant for the interfacial electron transfer from the LUMO of RhB to the CB of Ag_3PO_4, $k_{R\rightarrow A}$ was obtained by subtracting the k_R from the reciprocal of τ_1 (1.673 ns). The resulting value was 0.07×10^8 s^{-1}. The long decay time is responsible for the dynamic quenching of Ag_3PO_4. The recombination rate constant for Ag_3PO_4, k_A, was represented by a reciprocal of τ_2 (3.036 ns), and the value was estimated to be 3.29×10^8 s^{-1}. When the NC-dots/Ag_3PO_4 nanostructure was suspended in the RhB solution, the photoexcited electrons of RhB were injected into the CB of the Ag_3PO_4 as well as the LUMO of the NC-dots. The electrons injected into Ag_3PO_4 can be recombined with the existing holes in the HOMO of the NC-dots where the rate constant, $k_{A\rightarrow C}$, was determined to be 0.01×10^8 s^{-1}. The other electrons, injected into the LUMO of the NC-dots, are assumed to be sequentially transferred to the CB of Ag_3PO_4, because the NC-dots emit only negligible PL at 580 nm at λ_{ex} = 500

nm. Its corresponding rate constant was denoted by $k_{R\rightarrow C\rightarrow A}$, and the value was determined to be 1.63×10^8 s^{-1}. This process was 23 times faster than $k_{A\rightarrow C}$, leading to an efficient quenching of the holes left in the HOMO of NC-dots. Consequently, the presence of NC-dots remarkably facilitated the interfacial charge transfer from the RhB to the Ag_3PO_4 particles. The efficiency of the FRET process was also estimated from lifetime measurements of the donor in the absence and presence of an acceptor (see the Experimental Section), and the FRET efficiency increased by 8-fold after NC-dots were added to the system (2.8% → 22.6%).

Based on the experimental results, we propose that following mechanism for the RhB/NC-dots/Ag_3PO_4 system under irradiation with sub-band-gap light (**Figure 4.16b**). Highly luminescent RhB molecules absorb the incident light (λ_{ex} > 500 nm) and then transfer their energy to the NC-dots via FRET, which helps the NC-dots to create additional electron–hole pairs and increase its upconverted PL intensity. In turn, the NC-dots emit light with a wavelength longer than 350 nm as a result of the enhanced upconversion, and these upconverted photons are then consumed by the Ag_3PO_4 particles for sensitization. Moreover, the excited RhB transiently produces electrons, and a fraction of the electrons is injected into the CB of Ag_3PO_4 through the NC-dots. Finally, the electrons diffuse to the electrode to produce electrical current.

4.4 Conclusion

3.4 nm diameter NC-dots were highly dispersed on the surface of Ag_3PO_4 through the thermal decomposition of oleic acid, which increased the density of NC-dots and simultaneously removed the insulating long chain molecules on the nanocomposite. The resulting NC-dots showed hydrophilic interaction, sp^2 graphitic characteristics, and λ_{ex}-dependent PL behavior without any surface passivation. It is noteworthy that the NC-dots had upconversion properties emitting 150 nm shorter wavelength light when irradiated by λ_{ex} > 500 nm. These properties could be utilized for the effective energy conversion of sub-band-gap light into electricity on the Ag_3PO_4 particles by combining with highly luminescent RhB molecules. The enhanced photocurrent generation was mainly attributed to the synergistic effects of the following three features: (1) π–π interactions between the conjugated structure of the NC-dots and RhB molecules increased the adsorption of RhB on the surface of the NC-dots/Ag_3PO_4 nanocomposites, contributing to a more effective energy and electron transfer; (2) the FRET effect between NC-dots and RhB molecules helped the NC-dots create additional electron–hole pairs, and increased the upconverted light emission intensity of the NC-dots; (3) these upconverted photons were used to sensitize Ag_3PO_4 particles to form electron–hole pairs, resulting in the outstanding charge separation. Consequently, the designed fluorescence system showed an enhanced photocurrent generation on Ag_3PO_4 particles having an E_g of 2.5 eV at long visible-light wavelengths.

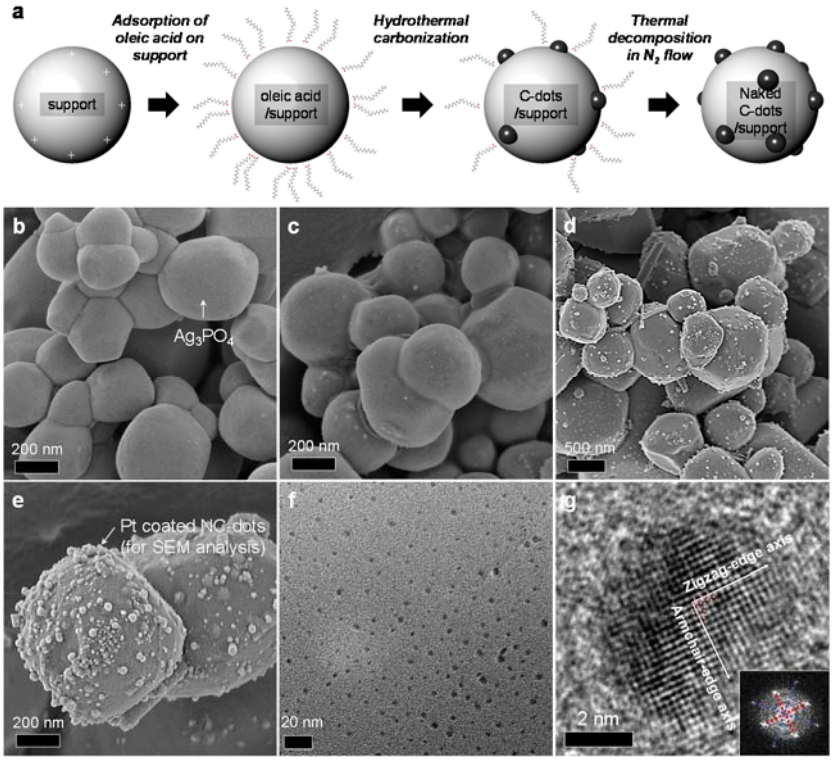

Figure 4.1 Morphology and composition of the NC-dots/Ag_3PO_4 nanocomposite using microscopy techniques. (a) Preparation of the NC-dots highly dispersed on support material. The support material was first prepared with positive surface charges in an aqueous suspension below its potential of zero charge. The carboxyl groups of oleic acid with negative charge are then adsorbed on the surface of the support. Third, a certain number of C-dots are formed on the surface of the support by hydrothermal carbonization. Finally, NC-dots are produced by removing the residual organics on the surface of the Ag_3PO_4 through thermal decomposition, which also leads to an increase in the population of the NC-dots. (b–e) SEM images of bare Ag_3PO_4, oleic acid/Ag_3PO_4, C-dots/Ag_3PO_4 prepared by hydrothermal carbonization, and

NC-dots/Ag_3PO_4 nanocomposites. (f) TEM image of the NC-dots after selectively melting down Ag_3PO_4 of the NC-dots/Ag_3PO_4 in dilute acidic solution. (g) HRTEM image of an NC-dot showing a hexagonal honeycomb structure containing zigzag and armchair edges of sp^2 graphitic carbon. Inset is a corresponding FFT pattern where the red lines connecting the symmetrical pairs of dots on the inner circle are perpendicular to the zigzag direction, and the blue lines on the outer circle are perpendicular to the armchair direction.

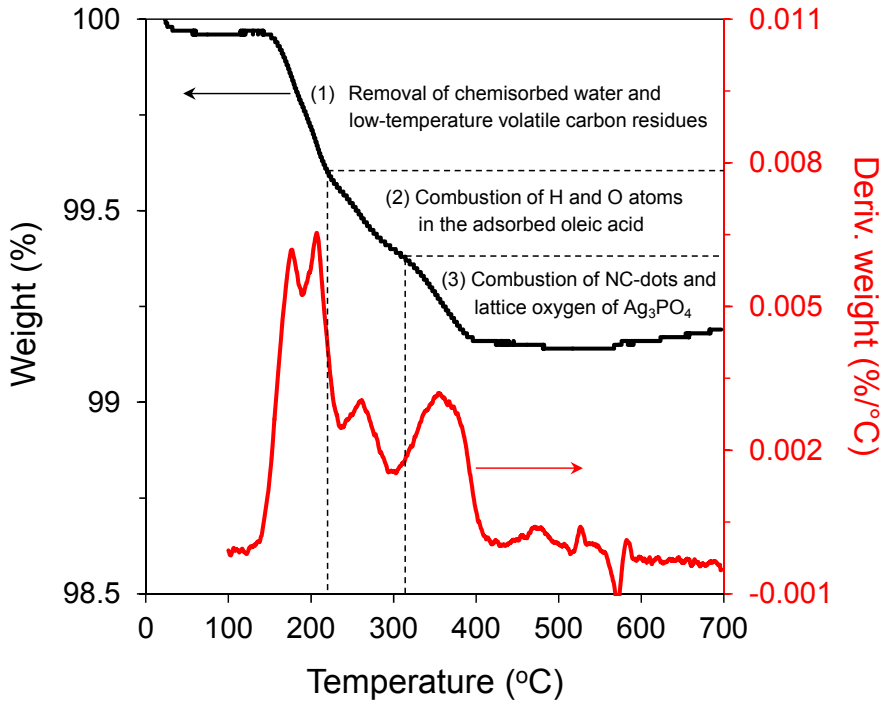

Figure 4.2 DTA/TGA profiles in N_2 flow of the C-dots/Ag_3PO_4 powders prepared by hydrothermal carbonization. Three weight loss zones can be categorized as follows. (1) Evaporation of chemisorbed water and some low-temperature volatile carbon residues (100–220 °C); (2) Reaction of hydrogen and oxygen atoms in the oleic acid to form water which then escapes from the surface of the nanocomposites (220–320 °C); (3) Weight loss from the high-temperature pyrolytic carbon species, that is, combustion of the NC-dots and lattice oxygen of Ag_3PO_4 (> 320 °C).

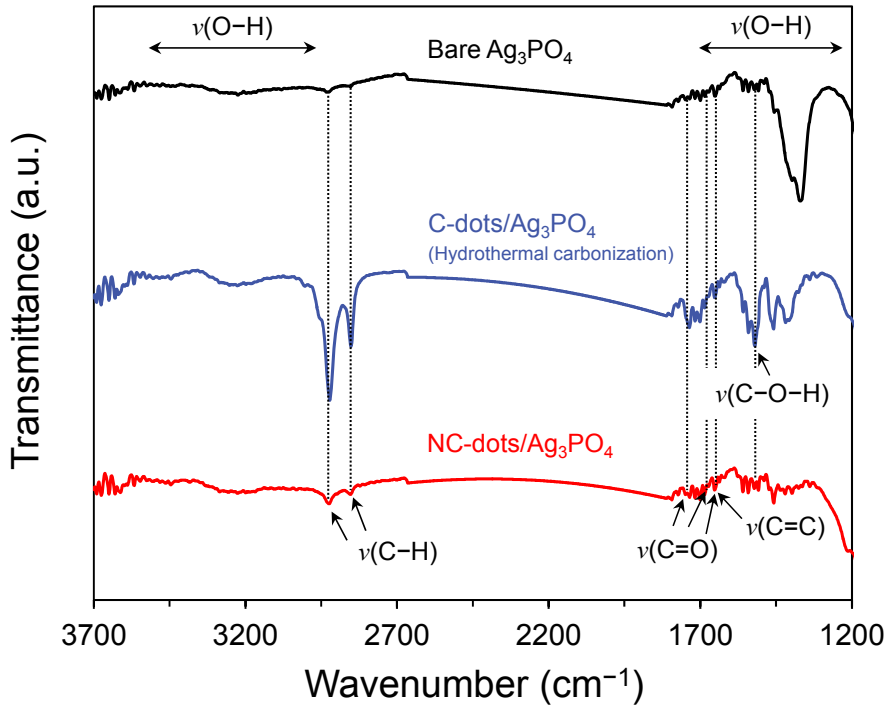

Figure 4.3 FTIR spectra of the samples at each step of the preparation of the NC-dots/Ag_3PO_4 nanocomposite. The broad bands in the region of 3500–3000 cm^{-1} and 1700–1200 cm^{-1} correspond to O–H stretching. The peaks at 2922 and 2851 cm^{-1} are assigned to C–H stretching bands of both alkyl and aromatic groups. The characteristic peak at 1650 cm^{-1} is associated with C=C stretch of polycyclic aromatic hydrocarbons. Carbonyl stretching C=O at 1760–1690 cm^{-1} and C–O–H stretching at 1517 cm^{-1} are assigned to the presence of carboxylic groups.

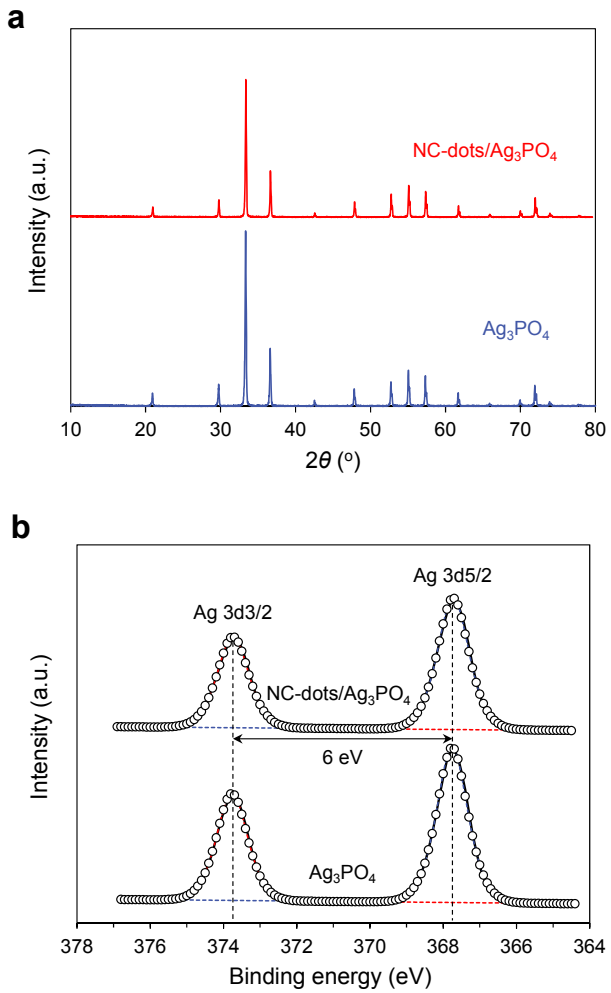

Figure 4.4 Stability of Ag_3PO_4 phase after the synthesis of NC-dots/Ag_3PO_4 nanocomposite. (a) XRD patterns of bare Ag_3PO_4 and NC-dots/Ag_3PO_4 nanocomposite. (b) Ag 3d XPS spectra of bare Ag_3PO_4 and NC-dots/Ag_3PO_4 where two peaks at 367.8 and 373.8 eV are indexed to Ag 3d5/2 and Ag 3d3/2 of Ag^+, respectively. Experimental data are shown as continuous lines, and the deconvoluted components are shown as dashed lines (blue: Ag 3d5/2, red: Ag 3d3/2). Open circles represent the sum of the individual fitted components.

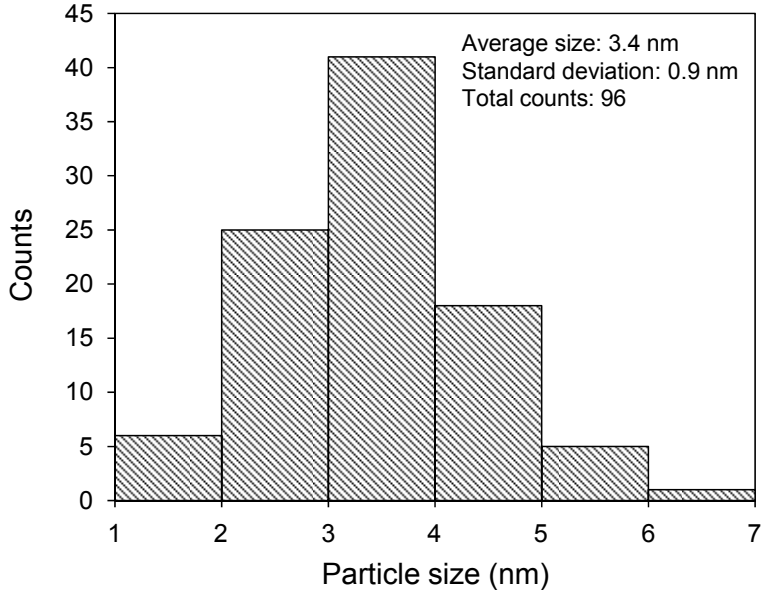

Figure 4.5 Size distribution of the NC-dots. The average diameter ($\pm$ standard deviation) of the NC-dots was 3.4($\pm$0.9) nm, calculated by counting the diameter of 96 individual NC-dots from TEM images.

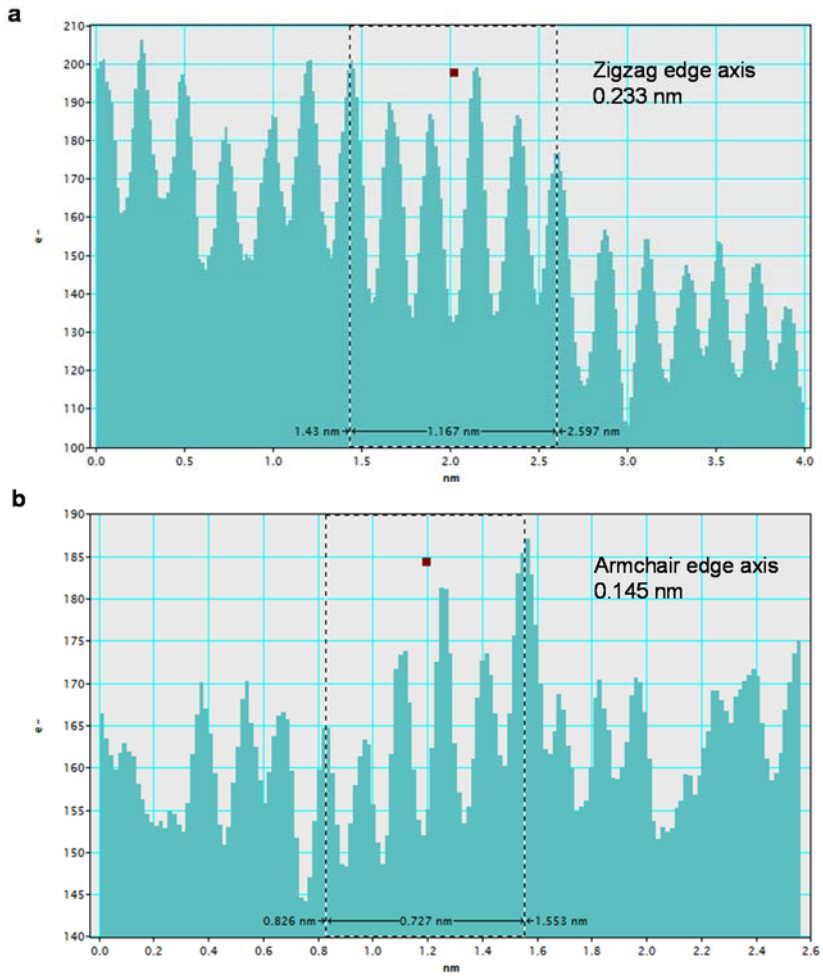

Figure 4.6 Characterization of the edge structures in a NC-dot. The line intensity profiles along the zigzag and armchair edges of Fig. 1g show that the average distances between the two peaks are (a) 0.233 nm and (b) 0.145 nm, respectively.

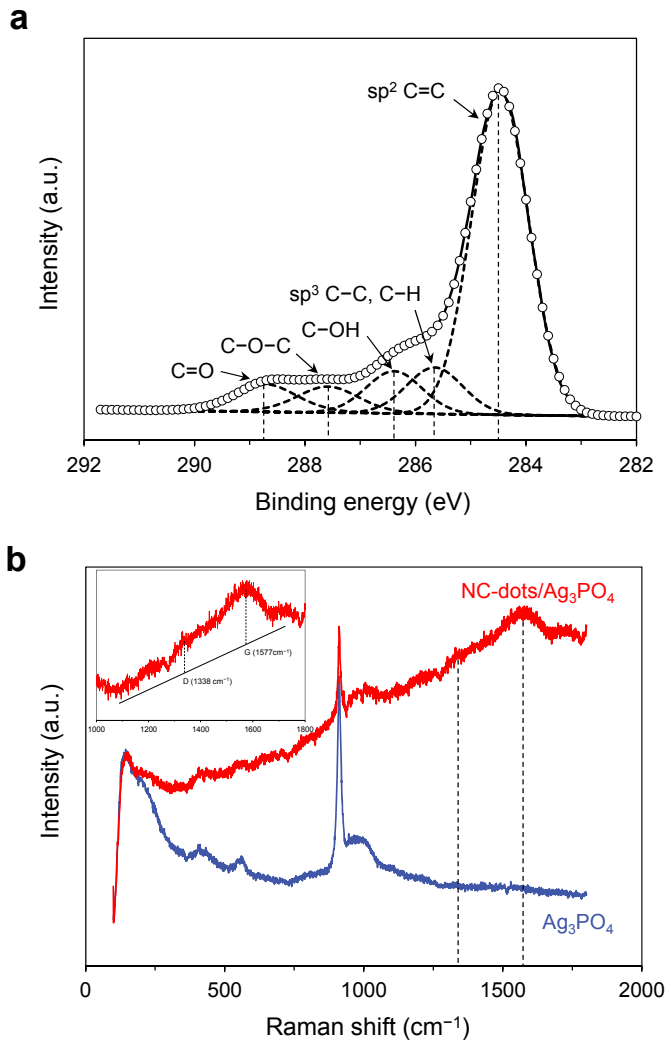

Figure 4.7 Chemical composition and structure of the NC-dots. (a) C 1s XPS spectrum of the NC-dots/Ag_3PO_4 which can be deconvoluted into five peaks centered at 284.5, 285.6, 286.4, 287.6 and 288.8 eV, corresponding to sp^2 C=C, sp^3 C–C/C–H, C–OH, C–O–C, and C=O, respectively. (b) Raman spectra of bare Ag_3PO_4 and the NC-dots/Ag_3PO_4 nanocomposite obtained using a 514 nm Ar laser. The G band at 1577 cm^{-1} corresponds to the E_{2g}

mode of graphite and is related to the vibration of sp^2-bonded carbon atoms in a 2D hexagonal lattice. The D band at around 1338 cm^{-1} is associated with the vibrations of carbon atoms with dangling bonds in the termination plane of disordered graphite or glassy. The rising background in the spectrum of NC-dots/Ag_3PO_4 is due to the PL emission of NC-dots.

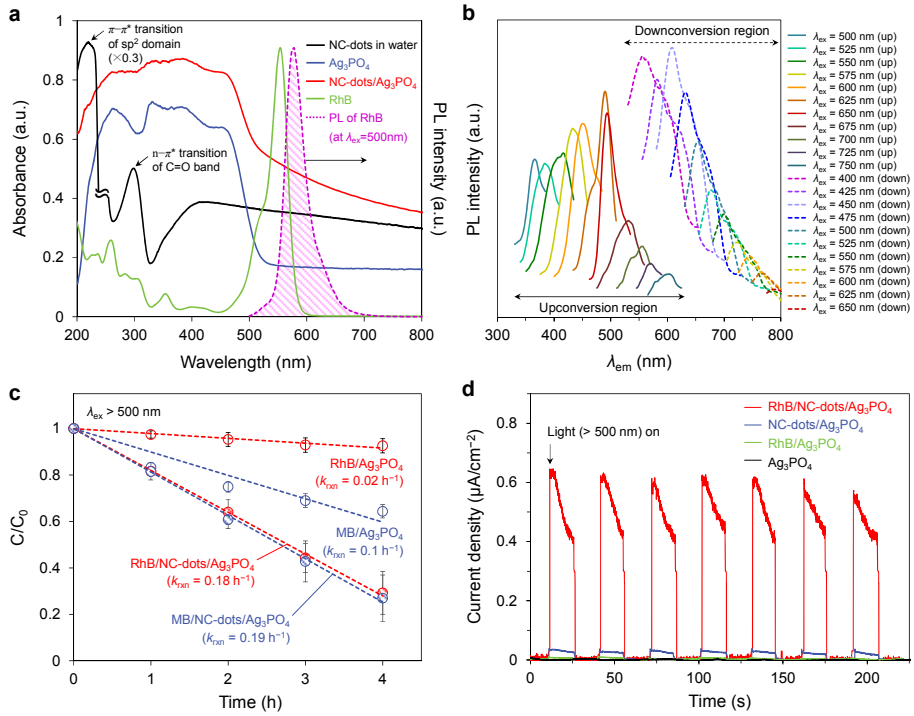

Figure 4.8 Optical properties and FRET-assisted upconversion enhancement. (a) UV-vis absorption spectra of the NC-dots dispersed in water, bare Ag_3PO_4, NC-dots/Ag_3PO_4, and RhB solution where dashed line represents PL emission of RhB at λ_{ex} = 500 nm. (b) Steady-state PL spectra of the NC-dots dispersed in water as a function of λ_{ex} where the solid line and dashed line refer to the upconversion and downconversion regions, respectively. (c) Photocatalytic degradation of 10 ppm RhB and 10 ppm MB in the presence of Ag_3PO_4 and NC-dots/Ag_3PO_4 at λ_{ex} > 500 nm. (d) Transient photocurrent responses at an applied potential of 0 V under irradiation by λ_{ex} > 500 nm with 30 s on/off cycles of the light.

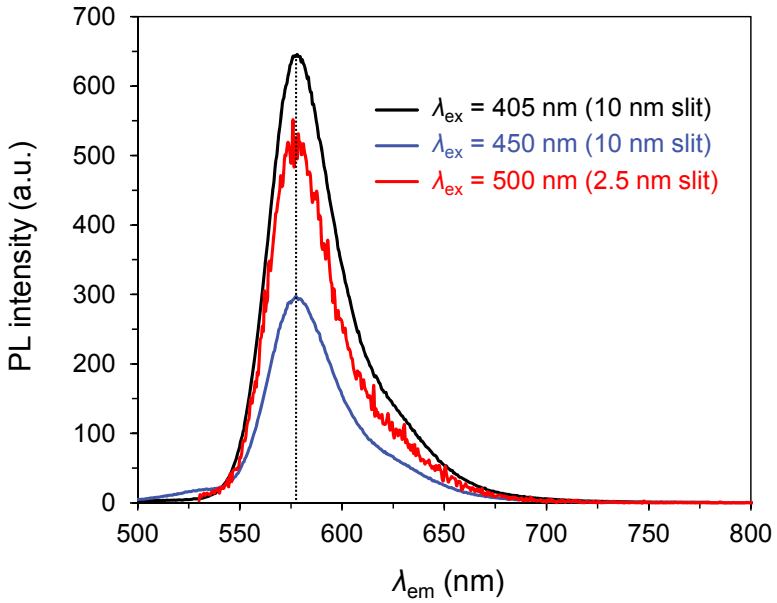

Figure 4.9 Fluorescence characteristics of the RhB molecules. Steady-state PL spectra of the RhB solution as a function of the emission wavelength, λ_{em}, where the excitation wavelengths, λ_{ex}, are 405, 450, and 500 nm.

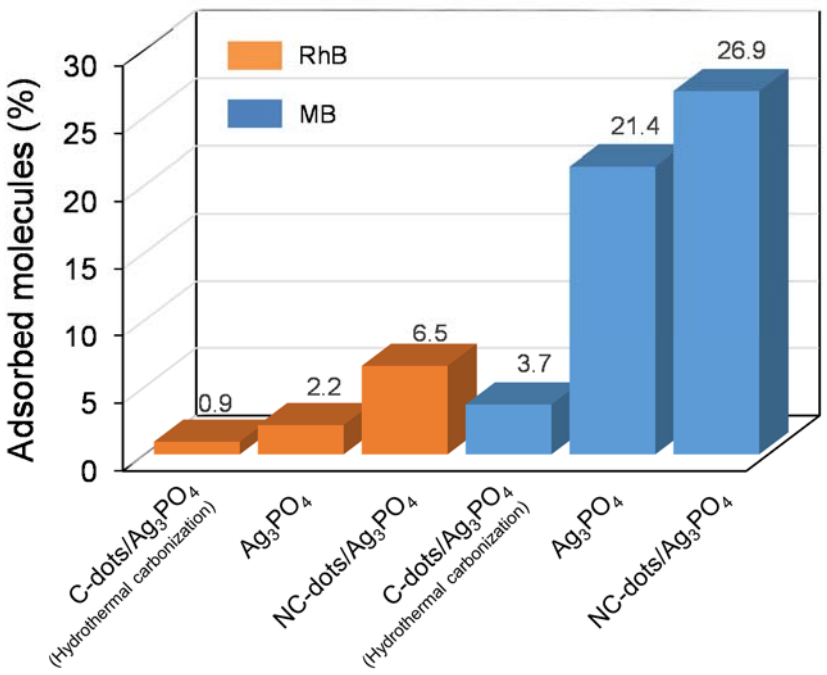

Figure 4.10 Dye adsorption experiments. Amounts of RhB and MB molecules absorbed on bare Ag_3PO_4, C-dots/Ag_3PO_4 prepared by hydrothermal carbonization, and NC-dots/Ag_3PO_4 nanocomposites after adsorption–desorption equilibrium.

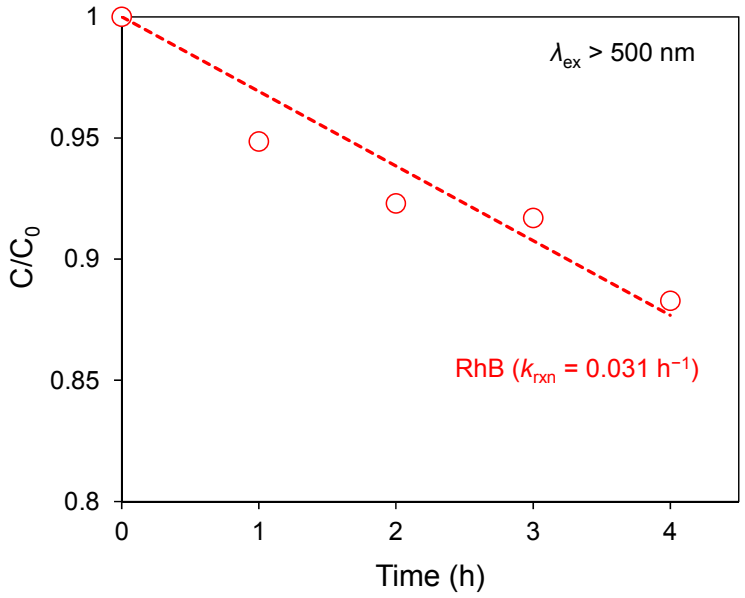

Figure 4.11 Adverse effect of insulating molecules on photocataytic activity. Photocatalytic degradation of 10 ppm RhB over the C-dots/Ag_3PO_4 catalyst prepared by hydrothermal carbonization at $\lambda_{ex} > 500$ nm.

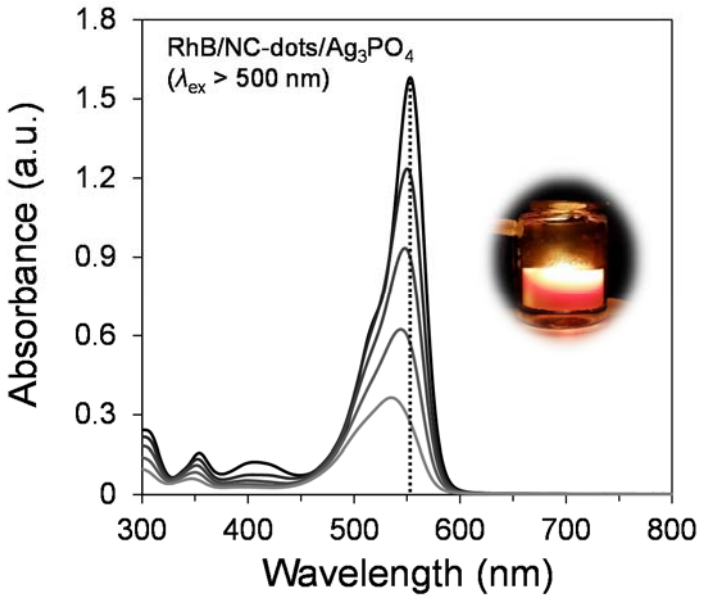

Figure 4.12 Photocatalytic degradation of RhB. UV–vis spectral changes of 10 ppm RhB at hourly intervals where the NC-dots/Ag_3PO_4 nanocomposite was used as a photocatalyst. Inset is a picture taken during the reaction under irradiation of λ_{ex} > 500 nm.

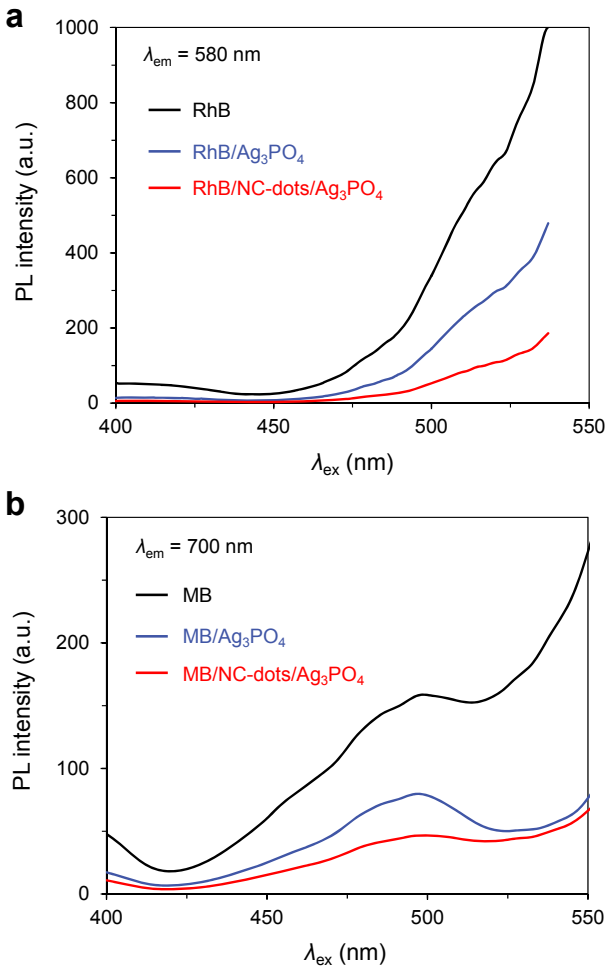

Figure 4.13 Steady-state PL spectra of (a) the RhB solutions and (b) the MB solutions in the presence of each sample as a function of λ_{ex} where λ_{em} is 580 nm and 700 nm, respectively. A 515 nm cut-off filter was placed between the monochromator and the sample to eliminate the second-order diffraction light of wavelength $\lambda/2$ coexisting in the excitation light.

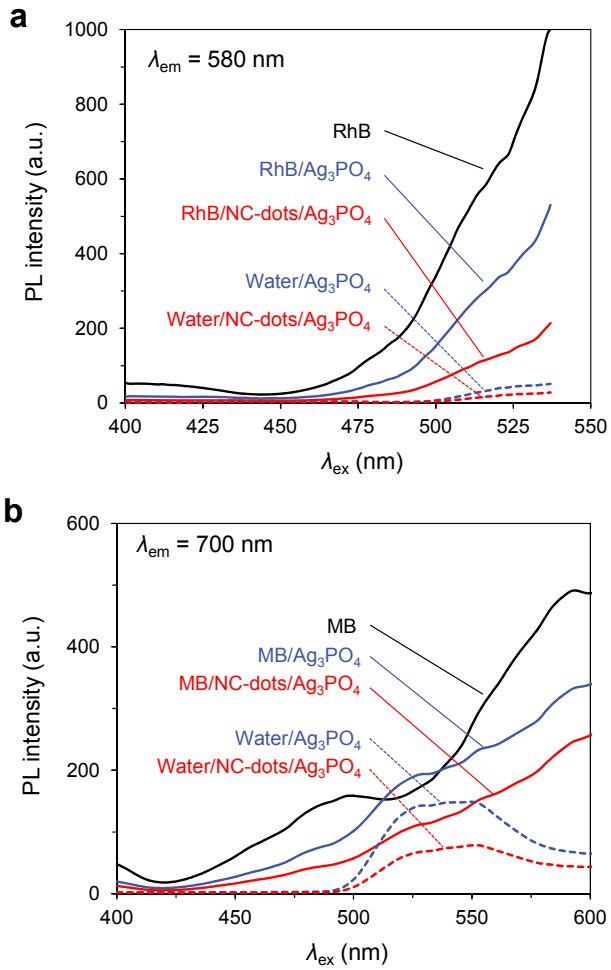

Figure 4.14 Steady-state PL spectra. Solid lines represent the PL emission of (a) RhB and (b) MB solutions in the presence of bare Ag_3PO_4 and the NC-dots/Ag_3PO_4 nanocomposite. Dashed lines indicate the PL emission of bare Ag_3PO_4 and the NC-dots/Ag_3PO_4 suspended in water as a function of excitation wavelength, λ_{ex}. The emission wavelengths, λ_{em}, of RhB and MB are 580 nm and 700 nm, respectively.

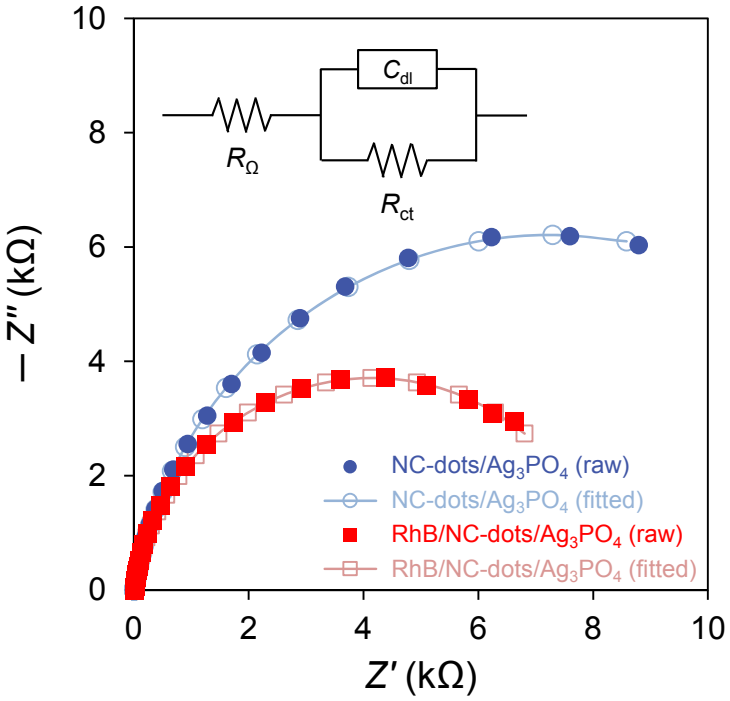

Figure 4.15 Nyquist plots of the NC-dots/Ag_3PO_4 photoanode in an aqueous solution of 0.1 M $NaClO_4$ as a supporting electrolyte with or without RhB molecules at λ_{ex} > 500 nm. Inset is an equivalent circuit for the interface between the photoanode and electrolyte where R_{Ω} is the bulk electrolyte resistance, C_{dl} is the double-layer capacitance, and R_{ct} is the charge-transfer resistance.

Table 4.1 Kinetic parameters extracted from fitting results of EIS spectra.[a]

	R_{Ω} (Ω)	Q_0 ($Ssec^n$)	n	R_{ct} (kΩ)
NC-dots/Ag_3PO_4	10.3	2.4×10^{-4}	0.900	14.6
RhB/NC-dots/Ag_3PO_4	13.1	2.3×10^{-4}	0.932	8.3

[a] The parameters were calculated using the ZMAN 2.2 software.

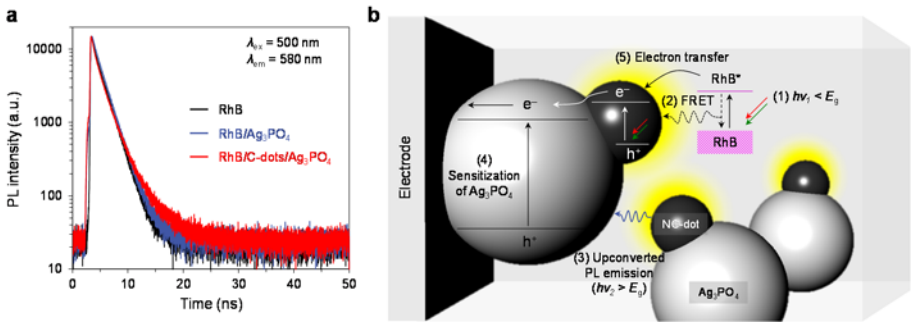

Figure 4.16 Kinetics and mechanism of the FRET-assisted upconversion process. (a) Time-resolved PL spectra of the RhB solutions in the presence of each sample with 500 nm excitation where λ_{em} is 580 nm. (b) Schematic energy band diagram of the RhB/NC-dots/Ag_3PO_4 nanocomposite, showing the FRET-assisted upconversion process across the three components. The numbered arrows indicate the following individual steps: (1) Excitation of the RhB molecules by the absorption of sub-band-gap light, (2) FRET from the excited RhB to nearby NC-dots, (3) Upconverted PL emission of the NC-dots, (4) Sensitization of Ag_3PO_4 particles to form an electron–hole pair, (5) Electron transfer from the LUMO of excited RhB to the CB of Ag_3PO_4 through the NC-dots.

Table 4.2 Kinetic parameters extracted from the fitting results of time-resolved PL spectra of RhB in the presence of each sample with 500 nm excitation.[a]

Entry	A_1	τ_1 (ns)	A_2	τ_2 (ns)	χ^2
RhB	11755.6	1.722	-	-	1.019
RhB + Ag_3PO_4	9780.6	1.673	484.9	3.036	0.998
RhB + NC-dots/Ag_3PO_4	7431.0	1.332	2252.9	3.032	1.111

[a] The parameters were calculated using the FluoFit software.

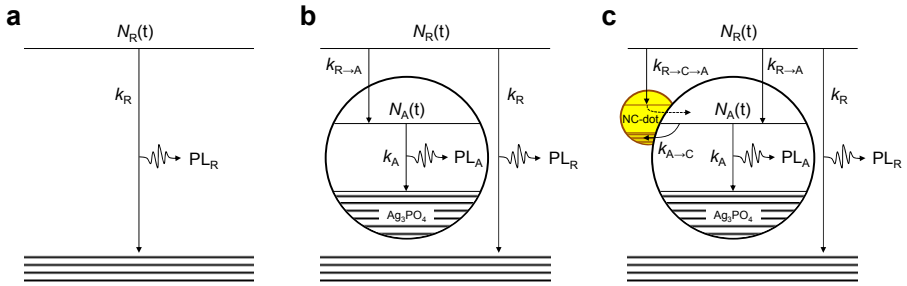

Figure 4.17 Decay pathways of the excited electrons when irradiated by λ_{ex} > 500 nm. The RhB solution contains (a) none, (b) Ag_3PO_4, and (c) NC-dots/Ag_3PO_4 nanocomposite where R, A, and C denote RhB, Ag_3PO_4, and NC-dots, respectively. $N_R(t)$ and $N_A(t)$ refer to the time-dependent electron populations in the LUMO of RhB and the CB of Ag_3PO_4, respectively. *k* represents the rate constant for electron transfer or charge recombination corresponding to its subscript. The excitation processes are not shown in this schematic diagram.

Table 4.3 Charge-transfer models when the excitation wavelength is 500 nm.

Entry	Balance equations for $N_R(t)$	Balance equations for $N_A(t)$
RhB (See Figure 4.17a)	$\frac{dN_R}{dt} = -k_R N_R$ $N_R = N_{R0} e^{-k_R t}$	-
RhB/Ag_3PO_4 (See Figure 4.17b)	$\frac{dN_R}{dt} = -(k_R + k_{R\to A}) N_R$ $N_R = N_{R0} e^{-(k_R + k_{R\to A})t}$	$\frac{dN_A}{dt} = k_{R\to A} N_R - k_A N_A$ $N_A = C_1 e^{-(k_R + k_{R\to A})t} + C_2 e^{-k_A t}$ [a]
RhB/NC-dots/Ag_3PO_4 (See Figure 4.17c)	$\frac{dN_R}{dt} = -(k_R + k_{R\to A} + k_{R\to C\to A}) N_R$ $N_R = N_{R0} e^{-(k_R + k_{R\to A} + k_{R\to C\to A})t}$	$\frac{dN_A}{dt} = (k_{R\to A} + k_{R\to C\to A}) N_R - (k_A + k_{A\to C}) N_A$ $N_A = C_3 e^{-(k_R + k_{R\to A} + k_{R\to C\to A})t} + C_4 e^{-(k_A + k_{A\to C})t}$ [b]

[a] $C_1 = \frac{k_{R\to A}}{k_A - (k_R + k_{R\to A})} \cdot N_{R0}$ and $C_2 = N_{A0} - C_1$ where N_{R0} and N_{A0} are constant.

[b] $C_3 = \frac{k_{R\to A} + k_{R\to C\to A}}{(k_A + k_{A\to C}) - (k_R + k_{R\to A} + k_{R\to C\to A})} \cdot N_{R0}$ and $C_4 = N_{A0} - C_3$.

Table 4.4 Calculated rate constants when the excitation and emission wavelengths are 500 nm and 580 nm, respectively.

Entry	Rate constants ($\times 10^8$ s^{-1})
k_R	5.81
$k_{R\rightarrow A}$	0.07
$k_{R\rightarrow C\rightarrow A}$	1.63
k_A	3.29
$k_{A\rightarrow C}$	0.01

Chapter 5. Summary and Prospectives

A visible-light-responsive nanocomposite was developed by combining Au@CdS core-shell and $TiO_{1.96}C_{0.04}$ for efficiently generating clean H_2 gas. The photocatalyst produced H_2 molecules at a rate of 433.2 μmol h^{-1}, which corresponds to QE of 23.6%. Spectroscopic tools were also developed for interrogating the electron-transfer processe of the photocatalytic system. The decay pathways of photoexcited electrons were constructed on the basis of the steady-state PL specta. The rate constants for interfacial electron transfer and charge recombination were calculated by comparing the exponents, k, of the model equations with the kinetic parameters τ_i. These calculated rate constants successfully explaned Z-schematic electron transfer, $TiO_{1.96}C_{0.04}$ → Au → CdS. In addition, the DFT calculation results of H_2 production energy on the surfaces of CdS and $TiO_{1.96}C_{0.04}$ showed that H_2 molecules prefered being formed on the CdS surface and the Z-schematic process of Au@CdS/$TiO_{1.96}C_{0.04}$ was also superior to the heterojunction of CdS/$TiO_{1.96}C_{0.04}$ for H_2 production. The findings also offer a novel approach to investigate the kinetic and thermodynamic role of hetero-interface in developing the efficient photocatalysts.

Based on the kinetic and mechanistic insights into the all-solid-state Z-schematic system, the Z-schematic charge transfer direction was entirely reversed by using perovskite $SrTiO_3$ nanoparticles (NPs) as a high performance electron filter instead of the PS II material, $TiO_{1.96}C_{0.04}$. As a

result, hot electron transfer of a Au core was enhanced by the strong electronic coupling to a CdS shell. As determined by the excitation-wavelength-dependent spectroscopic tools, the Au@CdS/$SrTiO_3$ nanostructure showed a favorable electron pathway, CdS → Au → $SrTiO_3$. This electron transfer led to the synergistic effects as following steps. The Au@CdS core-shell produced more electron–hole pairs with hot electrons through plasmonic photosensitization. The hot electrons were then easily injected from Au core into the CB of $SrTiO_3$ due to the Schottky junction of Au and $SrTiO_3$. The injected electrons diffused on perovskite $SrTiO_3$ with more negative CB than a reduction potential of H^+, and subsequently convert visible light to clean H_2 or to electricity. Consequently, the plasmonic core-shell nanostructure achieved a considerable H_2 production of 163.6 μmol h^{-1} (QE = 12.4%) and electron harvest at various wavelengths of visible light. The findings from this study will be informative for the design of not only plasmonic photocatalysts but also of PEC cells, such as photovoltaic and water splitting devices.

A FRET-assisted upconversion process across three components were introduced as an alternative to a significantly wasted portion of the sunlight. In this process, a highly luminescent RhB made a FRET pair with NC-dots of 3.4 nm. The FRET effect between NC-dots and RhB made the NC-dots create more electron–hole pairs, and increased the upconverted light emission intensity of the NC-dots. In addition, π–π interactions of the NC-dots with RhB increased the adsorption amount of RhB on the surface of the NC-dots/Ag_3PO_4 nanocomposites, leading to the enhanced energy and electron

transfer. These upconverted photons are subsequently used to sensitize Ag_3PO_4 particles with bandgap of 2.5 eV, cimproving the charge separation. Thus, the FRET-assisted upconversion process generate 18 times higher photocurrent at λ_{ex} > 500 nm than before adding the RhB molecules. The reason for increase in photocurrent generation is fundamentally unveiled by steady-state and time-resolved photoluminescence spectroscopies. The findings provide a new approach for the utilization of light energy in the visible and infrared region.

Figure 5.1 simply illustrates a sustainable H_2 energy society based on power plant for solar water splitting where clean H_2 can be safely produced and used for a basic synthetic component for various chemicals. This vision can be realized with assistance of other renewable energy sources such as wind and tidal, which can reduce operating costs by working the power plant with sunlight.

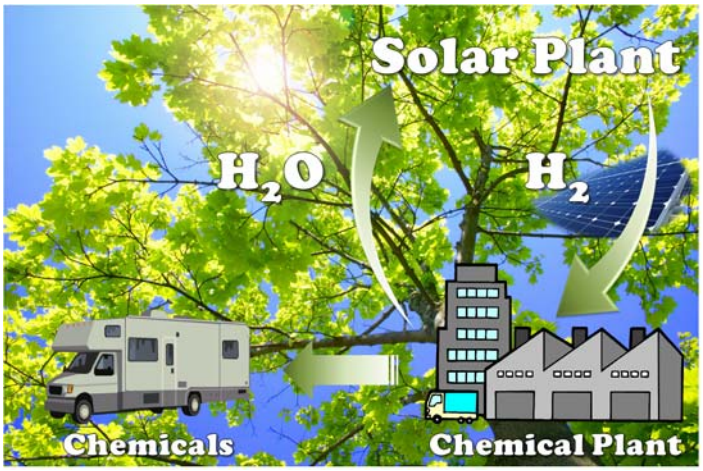

Figure 5.1 Schematic illustration of a sustainable H_2 energy society based on artificial photosynthesis.

Bibliography

[1] U.S. Energy Information Administration, International Energy Outlook 2013.

[2] L. N. Altork, J. R. Busby, *Technol. Eng. Teach.* **2010**, *70*, 22–27.

[3] P. V. Kamat, *J. Phys. Chem. C.* **2007**, *111*, 2834–2860.

[4] H. Tada, T. Mitsui, T. Kiyonaga, T. Akita, K. Tanaka, *Nat. Mater.* **2006**, *5*, 782–786.

[5] P. Zhou, J. Yu, M. Jaroniec, *Adv. Mater.* **2014**, *26*, 4920–4935.

[6] A. Kudo, Y. Miseki, *Chem. Soc. Rev.* **2009**, *38*, 253–278.

[7] H. Zhu, B. Yang, J. Xu, Z. Fu, M. Wen, T. Guo, S. Fu, J. Zuo, S. Zhang, *Appl. Catal., B* **2009**, *90*, 463–469.

[8] H. J. Yun, H. Lee, N. D. Kim, D. M. Lee, S. Yu, J. Yi, *ACS Nano* **2011**, *5*, 4084–4090.

[9] C. D. Chang, *Catal. Rev.* **1983**, *25*, 1–118.

[10] N. Gaponik, A. L. Rogach, *Phys. Chem. Chem. Phys.* **2010**, *12*, 8685–8693.

[11] S. Yu, H. J. Yun, Y. H. Kim, J. Yi, *Appl. Catal., B* **2014**, *144*, 893–899.

[12] S. U. M. Khan, M. Al-Shahry, W. B. Ingler Jr., *Science* **2002**, *297*, 2243–2245.

[13] X. Chen, L. Liu, P. Y. Yu, S. S. Mao, *Science* **2011**, *331*, 746–750.

[14] K. Iwashina, A. Kudo, *J. Am. Chem. Soc.* **2011**, *133*, 13272–13275.

[15] B.-S. Huang, E.-C. Su, M.-Y. Wey, *Chem. Eng. J.* **2013**, *223*, 854–859.

[16] M. Xu, P. Da, H. Wu, D. Zhao, G. Zheng, *Nano Lett.* **2012**, *12*, 1503–1508.

[17] J. H. Park, S. Kim, A. J. Bard, *Nano Lett.* **2006**, *6*, 24–28.

[18] R. Asahi, T. Morikawa, T. Ohwaki, K. Aoki, Y. Taga, *Science* **2001**, *293*, 269–271.

[19] M. R. Hoffmann, S. T. Martin, W. Choi, D. W. Bahneman, *Chem. Rev.* **1995**, *95*, 69–96.

[20] J. Zhang, C. Tang, J. H. Bang, *Electrochem. Commun.* **2010**, *12*, 1124–1128.

[21] G. Wang, X. Yang, F. Qian, J. Z. Zhang, Y. Li, *Nano Lett.* **2010**, *10*, 1088–1092.

[22] J. Hensel, G. Wang, Y. Li, J. Z. Zhang, *Nano Lett.* **2010**, *10*, 478–483.

[23] W. J. Youngblood, S.-H. A. Lee, Y. Kobayashi, E. A. Hernandez-Pagan, P. G. Hoertz, T. A. Moore, A. L. Moore, D. Gust, T. E. Mallouk, *J. Am. Chem. Soc.* **2009**, *131*, 926–927.

[24] R. Jiang, B. Li, C. Fang, J. Wang, *Adv. Mater.* **2014**, *26*, 5274–5309.

[25] S. K. Dutta, S. K. Mehetor, N. Pradhan, *J. Phys. Chem. Lett.* **2015**, *6*, 936–944.

[26] Y.-P. Yuan, L.-W. Ruan, J. Barber, S. C. J. Loo, C. Xue, *Energy Environ. Sci.* **2014**, *7*, 3934–3951.

[27] R. Marschall, *Adv. Funct. Mater.* **2014**, *24*, 2421–2440.

[28] H. Tong, S. Ouyang, Y. Bi, N. Umezawa, M. Oshikiri, J. Ye, *Adv. Mater.* **2012**, *24*, 229–251.

[29] Y. Tachibana, L. Vayssieres, J. R. Durrant, *Nat. Photonics* **2012**, *6*, 511–518.

[30] Y.-C. Pu, W.-H. Lin, Y.-J. Hsu, *Appl. Catal., B* **2015**, *163*, 343–351.

[31] K.-H. Lin, C.-Y. Chuang, Y.-Y. Lee, F.-C. Li, Y.-M. Chang, *J. Phys. Chem. C* **2012**, *116*, 1550–1555.

[32] Y.-C. Chen, Y.-C. Pu, Y.-J. Hsu, *J. Phys. Chem. C* **2012**, *116*, 2967–2975.

[33] T.-T. Yang, W.-T. Chen, Y.-J. Hsu, K.-H. Wei, T.-Y. Lin, T.-W. Lin, *J. Phys. Chem. C* **2010**, *114*, 11414–11420.

[34] Y.-F. Lin, Y.-J. Hsu, *Appl. Catal., B* **2013**, *130–131*, 93–98.

[35] S. Yu, Y. H. Kim, S. Y. Lee, H. D. Song, J. Yi, *Angew. Chem., Int. Ed.* **2014**, *53*, 11203–11207.

[36] G. Kresse, J. Furthmüller, *Phys. Rev. B* **1996**, *54*, 11169–11186.

[37] J. P. Perdew, K. Burke, M. Ernzerhof, *Phys. Rev. Lett.* **1996**, *77*, 3865–3868.

[38] P. E. Blöchl, *Phys. Rev. B* **1994**, *50*, 17953–17979.

[39] G. Henkelman, H. Jónsson, *J. Chem. Phys.* **2000**, *113*, 9978–9985.

[40] G. Henkelman, B. P. Uberuaga, H. A Jónsson, *J. Chem. Phys.* **2000**, *113*, 9901–9904.

[41] H. J. Yun, H. Lee, J. B. Joo, N. D. Kim, M. Y. Kang, J. Yi, *Appl. Catal., B* **2010**, *94*, 241–247.

[42] Y. Park, W. Kim, H. Park, T. Tachikawa, T. Majima, W. Choi, *Appl. Catal., B* **2009**, *91*, 355–361.

[43] I. Luciu, R. Bartali, N. Laidani, *J. Phys. D: Appl. Phys.* **2012**, *45*, 345302.

[44] K. Wu, W. E. Rodríguez-Córdoba, Y. Yang, T. Lian, *Nano Lett.* **2013**, *13*, 5255–5263.

[45] C. Li, J. Yuan, B. Han, L. Jiang, W. Shangguan, *Int. J. Hydrogen Energ.* **2010**, *35*, 7073–7079.

[46] A. Deshpande, N. M. Gupta, *Int. J. Hydrogen Energ.* **2010**, *35*, 3287–3296.

[47] S. V. Awate, S. S. Deshpande, K. Rakesh, P. Dhanasekaran, N. M. Gupta, *Phys. Chem. Chem. Phys.* **2011**, *13*, 11329–11339.

[48] H. J. Yun, H. Lee, J. B. Joo, N. D. Kim, J. Yi, *Electrochem. Commun.* **2010**, *12*, 769–772.

[49] J. S. Jang, H. G. Kim, P. H. Borse, J. S. Lee, *Int. J. Hydrogen Energ.* **2007**, *32*, 4786–4791.

[50] J. S. Jang, S. M. Ji, S. W. Bae, H. C. Son, J. S. Lee, *J. Photochem. Photobiol. A* **2007**, *188*, 112–119.

[51] V. M. Daskalaki, M. Antoniadou, G. L. Puma, D. I. Kondarides, P. Lianos, *Environ. Sci. Technol.* **2010**, *44*, 7200–7205.

[52] U. Aschauer, A. Selloni, *Phys. Chem. Chem. Phys.* **2012**, *14*, 16595–16602.

[53] J. Shi, J. Chen, Z. Feng, T. Chen, Y. Lian, X. Wang, C. Li, *J. Phys. Chem. C* **2007**, *111*, 693–699.

[54] X. Wang, Z. Feng, J. Shi, G. Jia, S. Shen, J. Zhou, C. Li, *Phys. Chem. Chem. Phys.* **2010**, *12*, 7083–7090.

[55] J. R. Lakowicz, *Principles of Fluorescence Spectroscopy*, 3rd ed., Springer, NewYork, 2006.

[56] A. Deshpande, G. Madras, N. M. Gupta, *Mater. Chem. Phys.* **2011**, *126*, 546–554.

[57] Y.-G. Lin, Y.-K. Hsu, Y.-C. Chen, S.-B. Wang, J. T. Miller, L.-C. Chen, K.-H. Chen, *Energy Environ. Sci.* **2012**, *5*, 8917–8922.

[58] Z. Liu, W. Hou, P. Pavaskar, M. Aykol, S. B. Cronin, *Nano Lett.* **2011**, *11*, 1111–1116.

[59] Y. Tian, T. Tatsuma, *J. Am. Chem. Soc.* **2005**, *127*, 7632–7637.

[60] J. Lee, S. Mubeen, X. Ji, G. D. Stucky, M. Moskovits, *Nano Lett.* **2012**, *12*, 5014–5019.

[61] S. Mubeen, J. Lee, N. Singh, S. Krämer, G. D. Stucky, M. Moskovits, *Nat. Nanotech.* **2013**, *8*, 247–251.

[62] X. Zhang, Y. L. Chen, R.-S. Liu, D. P. Tsai, *Rep. Prog. Phys.* **2013**, *76*, 046401–046443.

[63] S. C. Warren, E. Thimsen, *Energy Environ. Sci.* **2012**, *5*, 5133–5146.

[64] S. A. Maier, *Plasmonics: Fundamentals and Applications*, Spinger, New York, 2007.

[65] J. Hohlfeld, S.-S. Wellershoff, J. Güdde, U. Conrad, V. Jähnke, E. Matthias, *Chem. Phys.* **2000**, *251*, 237–258.

[66] H. Inouye, K. Tanaka, *Phys. Rev. B* **1998**, *57*, 11334–11340.

[67] J. H. Hodak, I. Martini, G. V. Hartland, *J. Phys. Chem. B* **1998**, *102*, 6958–6967.

[68] M. A. Yurkin, A. G. Hoekstra, *J. Quant. Spectrosc. Radiat.* **2007**, *106*, 558–589.

[69] B. T. Draine, *J. Opt. Soc. Am. A* **1994**, *11*, 1491–1499.

[70] E. D. Palik, *Handbook of Optical Constants of Solids*, ELSEVIER SCIENCE, USA, 1991.

[71] M. J. Weber, *Handbook of Optical Materials*, CRC PRESS: Boca Raton, FL, 2003.

[72] http://search.newport.com/?q=*&x2=sku&q2=6258

[73] A. J. Bard, L. R. Faulkner, *Electrochemical Methods: Fundamentals and Applications*, Vol. 2, Wiley, NY, 2001.

[74] B. G. Streetman, S. K. Banerjee, *Solid State Electronic Devices*, Vol. 6, Pearson Prentice Hall, NY, 2006.

[75] T. K. Townsend, N. D. Browning, F. E. Osterloh, *ACS Nano* **2012**, *6*, 7420–7426.

[76] P. Reunchan, S. Ouyang, N. Umezawa, H. Xu, Y. Zhang, J. Ye, *J. Mater. Chem. A* **2013**, *1*, 4221–4227.

[77] W. Xu, J. Yang, W. Bai, K. Tang, Y. Zhang, X. Tang, *J. Appl. Phys.* **2013**, *114*, 154106.

[78] R. Leonelli, J. L. Brebner, *Phys. Rev. B* **1986**, *33*, 8649–8656.

[79] M. Capizzi, A. Frova, *Phys. Rev. Lett.* **1970**, *25*, 1298–1302.

[80] M. W. Knight, H. Sobhani, P. Nordlander, N. J. Halas, *Science* **2011**, *332*, 702–704.

[81] Y. K. Lee, C. H. Jung, J. Park, H. Seo, G. A. Somorjai, J. Y. Park, *Nano Lett.* **2011**, *11*, 4251–4255.

[82] S. Mubeen, G. Hernandez-Sosa, D. Moses, J. Lee, M. Moskovits, *Nano Lett.* **2011**, *11*, 5548–5552.

[83] Y. Yang, W. Rodríguez-Córdoba, X. Xiang, T. Lian, *Nano Lett.* **2012**, *12*, 303–309.

[84] S. N. Baker, G. A. Baker, *Angew. Chem., Int. Ed.* **2010**, *49*, 6726–6744.

[85] H. Li, X. He, Z. Kang, H. Huang, Y. Liu, J. Liu, S. Lian, C. H. A. Tsang, X. Yang, S.-T. Lee, *Angew. Chem., Int. Ed.* **2010**, *49*, 4430–4434.

[86] S. Qu, X. Wang, Q. Lu, X. Liu, L. Wang, *Angew. Chem., Int. Ed.* **2012**, *51*, 12215–12218.

[87] G. Eda, Y.-Y. Lin, C. Mattevi, H. Yamaguchi, H.-A. Chen, I-S. Chen, C.-W. Chen, M. Chhowalla, *Adv. Mater.* **2010**, *22*, 505–509.

[88] K. P. Loh, Q. Bao, G. Eda, M. Chhowalla, *Nat. Chem.* **2010**, *2*, 1015–1024.

[89] S. Srivastava, N. S. Gajbhiye, *ChemPhysChem* **2011**, *12*, 2624–2632.

[90] Y.-P. Sun, B. Zhou, Y. Lin, W. Wang, K. A. S. Fernando, P. Pathak, M. J. Meziani, B. A. Harruff, X. Wang, H. Wang, P. G. Luo, H. Yang, M. E. Kose, B. Chen, L. M. Veca, S.-Y. Xie, *J. Am. Chem. Soc.* **2006**, *128*, 7756–7757.

[91] D. Pan, J. Zhang, Z. Li, M. Wu, *Adv. Mater.* **2010**, *22*, 734–738.

[92] J. Briscoe, A. Marinovic, M. Sevilla, S. Dunn, M. Titirici, *Angew. Chem., Int. Ed.* **2015**, *54*, 4463–4468.

[93] H. Zhang, H. Huang, H. Ming, H. Li, L. Zhang, Y. Liu, Z. Kang, *J. Mater. Chem.* **2012**, *22*, 10501–10506.

[94] Z. Ma, Y.-L. Zhang, L. Wang, H. Ming, H. Li, X. Zhang, F. Wang, Y. Liu, Z. Kang, S.-T. Lee, *ACS Appl. Mater. Interfaces* **2013**, *5*, 5080–5084.

[95] J. Di, J. Xia, Y. Ge, H. Li, H. Ji, H. Xu, Q. Zhang, H. Li, M. Li, *Appl. Catal., B* **2015**, *168–169*, 51–61.

[96] C. Wang, X. Wu, X. Li, W. Wang, L. Wang, M. Gu, Q. Li, *J. Mater. Chem.* **2012**, *22*, 15522–15525.

[97] P. Zhang, C. Shao, Z. Zhang, M. Zhang, J. Mu, Z. Guo, Y. Sun, Y. Liu, *J. Mater. Chem.* **2011**, *21*, 17746–17753.

[98] M. Sun, S. Qu, W. Ji, P. Jing, D. Li, L. Qin, J. Cao, H. Zhang, J. Zhao, D. Shen, *Phys. Chem. Chem. Phys.* **2015**, *17*, 7966–7971.

[99] X. Zhang, H. Huang, J. Liu, Y. Liu, Z. Kang, *J. Mater. Chem. A* **2013**, *1*, 11529–11533.

[100] J. Pan, Y. Sheng, J. Zhang, J. Wei, P. Huang, X. Zhang, B. Feng, *J. Mater. Chem. A* **2014**, *2*, 18082–18086.

[101] J. Tian, Y. Leng, Z. Zhao, Y. Xia, Y. Sang, P. Hao, J. Zhan, M. Li, H. Liu, *Nano Energy* **2015**, *11*, 419–427.

[102] Y. Lee, I. Yang, J. E. Lee, S. Hwang, J. W. Lee, S.-S. Um, T. L. Nguyen, P. J. Yoo, H. Y. Woo, J. Park, S. K. Kim, *J. Phys. Chem. C* **2013**, *117*, 3298–3307.

[103] P. Amornpitoksuk, K. Intarasuwan, S. Suwanboon, J. Baltrusaitis, *Ind. Eng. Chem. Res.* **2013**, *52*, 17369–17375.

[104] A. Barrie, N. E. Christensen, *Phys. Rev. B* **1976**, *14*, 2442–2447.

[105] B. J. Murray, Q. Li, J. T. Newberg, E. J. Menke, J. C. Hemminger, R. M. Penner, *Nano Lett.* **2005**, *5*, 2319–2324.

[106] X. Jia, M. Hofmann, V. Meunier, B. G. Sumpter, J. Campos-Delgado, J. M. Romo-Herrera, H. Son, Y.-P. Hsieh, A. Reina, J. Kong, M. Terrones, M. S. Dresselhaus, *Science* **2009**, *323*, 1701–1705.

[107] L. Lin, S. Zhang, *Chem. Commun.* **2012**, *48*, 10177–10179.

[108] C. Cong, K. Li, X. X. Zhang, T. Yu, *Sci. Rep.* **2013**, *3*, 1195.

[109] J. Peng, W. Gao, B. K. Gupta, Z. Liu, R. Romero-Aburto, L. Ge, L. Song, L. B. Alemany, X. Zhan, G. Gao, S. A. Vithayathil, B. A. Kaipparettu, A. A. Marti, T. Hayashi, J.-J. Zhu, P. M. Ajayan, *Nano Lett.* **2012**, *12*, 844–849.

[110] L. Tang, R. Ji, X. Cao, J. Lin, H. Jiang, X. Li, K. S. Teng, C. M. Luk, S. Zeng, J. Hao, S. P. Lau, *ACS Nano* **2012**, *6*, 5102–5110.

[111] H. Nie, M. Li, Q. Li, S. Liang, Y. Tan, L. Sheng, W. Shi, S. X.-A. Zhang, *Chem. Mater.* **2014**, *26*, 3104–3112.

[112] A. Martínez-de la Cruz, U. M. García Pérez, *Mater. Res. Bull.* **2010**, *45*, 135–141.

[113] Z. Yi, J. Ye, N. Kikugawa, T. Kako, S. Ouyang, H. Stuart-Williams, H. Yang, J. Cao, W. Luo, Z. Li, Y. Liu, R. L. Withers, *Nat. Mater.* **2010**, *9*, 559–564.

[114] J. N. Tiwari, K. Mahesh, N. H. Le, K. C. Kemp, R. Timilsina, R. N. Tiwari, K. S. Kim, *Carbon* **2013**, *56*, 173–182.

[115] A. Martínez-de la Cruz, U. M. García Pérez, *Mater. Res. Bull.* **2010**, *45*, 135–141.

[116] T. Wu, G. Liu, J. Zhao, H. Hidaka, N. Serpone, *J. Phys. Chem. B* **1998**, *102*, 5845–5851.

[117] Q. Liang, Y. Shi, W. Ma, Z. Li, X. Yang, *Phys. Chem. Chem. Phys.* **2012**, *14*, 15657–15665.

[118] B. Chai, J. Li, Q. Xu, *Ind. Eng. Chem. Res.* **2014**, *53*, 8744–8752.

국 문 초 록

산업화 이후 화석연료의 사용량 급증으로 인해 환경오염과 지구온난화가 심각해지고 있고, 이에 따라 물과 태양광을 활용한 친환경에너지 생산에 관심이 집중되고 있다. 지속가능한 사회를 위한 차세대기술로서 인공광합성기술은 물의 태양광 분해를 통해 온실가스나 불순물이 전혀 포함되어 있지 않은 무한청정수소 연료를 별도의 분리공정을 거치지 않고 생산할 수 있으며, 유사한 메커니즘을 이용해 수소연료 대신 태양광으로부터 친환경적으로 전기도 생산할 수 있다. 그러나 현재까지의 반도체기반 광촉매를 이용한 청정수소제조기술은 효율이 낮아 경제성을 갖지 못하고 있으며, 상용화된 태양전지 역시 효율이 낮고 비싼 가격 때문에 널리 사용되고 있지 못하는 실정이다.

이 학위논문은 자연계 광합성작용을 모방하는 반도체 기반 나노입자의 물리·화학적 특성과 나노계면에서 일어나는 미시적 현상들에 대한 근본적인 이해를 바탕으로 가시광 에너지를 효과적으로 변환할 수 있는 광촉매 나노물질의 개발에 대하여 다룬다. 이를 위해 태양광의 대부분(약 44.4%)을 차지하는 가시광선에서 녹색식물의 광합성을 그대로 모방한 코어-쉘 구조의 Pt/Au@CdS/$TiO_{1.96}C_{0.04}$ 인공광합성 무기나노입자를 합성하였으며, 기존의 연구성과에 비해 5 배 이상 많은 양의 수소를

생산하였다. 그러나 현재까지 반도체-금속-반도체와 같은 복잡한 구조의 3 성분계 나노시스템에서 전자이동을 규명할 수 있는 연구방법이 밝혀지지 않아 개발한 나노입자 내에서의 전자이동속도 및 메커니즘에 대한 이해가 부족하였다. 이 연구에서는 피코초(1 조분의 1 초) 수준에서의 형광 측정을 통해 나노입자 내에서의 전자이동속도와 양자역학적 제 1 원리 계산을 통해 표면반응 메커니즘을 밝혔다. 이 연구결과는 미시적 관점에서 태양광에 효율적으로 작동할 수 있는 신소재의 합리적인 설계에 필요한 새로운 방식의 속도론적, 열역학적 접근 방법을 제시하였다.

전자이동속도 및 메커니즘에 대한 이해로부터 상기 인공광합성 나노입자 시스템은 수소생산에는 유리하지만, 알파벳 Z 모양의 전자전달방향 때문에 전기에너지 생산에는 불리하다는 사실을 밝혔다. 세 성분 중 $TiO_{1.96}C_{0.04}$ 을 고성능의 전자필터 역할을 할 수 있는 페로브스카이트 결정구조를 갖는 $SrTiO_3$ 로 교체해줌으로써 기존 Z-scheme 전자전달방향을 완전히 반대방향으로 바꿨다. 이로 인해 금 입자에서 발생하는 플라즈모닉 열전자의 수명을 획기적으로 향상시켜 기존의 금 촉매에 비해 무려 74 배 많은 양의 수소를 생산했으며, 물에서 수소뿐만 아니라 전기에너지도 얻는데 성공했다. 이 연구결과는 기존의 에너지 생산 시스템을 혁신하여 청정에너지기반 산업에 기여할 수 있을 것으로 기대될 뿐만 아니라, 향후 이 기술의 시스템화와 함께

에너지저장기술이 더 발전되면 외부로부터 전기나 연료주입 없이 가전기기나 더 나아가 자동차도 물만으로 작동시킬 수 있을 것으로 전망한다.

대부분의 광촉매 물질들은 2.5 eV 이상의 밴드갭 특성을 보인다. 따라서, 500 nm 보다 긴 파장대의 광자는 이러한 물질들을 여기시키기에 충분하지 않은 에너지를 가지고 있기 때문에 태양광의 상당 부분이 활용되지 못하고 있는 실정이다. 업컨버젼(upconversion)은 일종의 반스토크스(anti-stokes) 현상으로서 최소한 두 개의 광자에서 하나의 더 높은 에너지를 갖는 광자를 만든다. 이 현상은 광범위한 태양 스펙트럼의 효과적인 활용을 가능하게 하고, 최근 태양전지 및 태양광 에너지 전환 분야에서 광활성 물질의 밴드갭보다 작은 에너지의 빛을 흡수하게 함으로써 시스템의 효율 향상을 위한 수단으로 적극 활용되고 있다. 이 연구에서는 형광 공명 에너지 전달(fluorescence resonance energy transfer, FRET)을 응용함으로써 궁극적으로 시스템의 업컨버젼 효율을 향상시켰다. 이를 위해 3.4 nm 크기의 탄소 양자점 소재를 어떠한 절연 분자 및 표면개질과정 없이 개발하였고, 이 소재는 여기 파장에 따른 업컨버젼 거동을 보였다. 특히, 500 nm 보다 긴 파장의 빛을 조사하였을 때, 탄소 양자점은 여기 파장보다 150 nm 짧은 파장의 형광을 방출하였다. 탄소 양자점은 강한 발광물질인 로다민 B 와 함께 FRET 쌍을 이루어 탄소 양자점에서 발생하는 형광의 세기와 들뜬 전자의 수를

증가시켰다. 업컨버젼된 광자는 2.5 eV 의 밴드갭을 갖는 광활성 물질을 작동시키는데 충분한 에너지를 보였다. 결과적으로 로다민 B, 탄소 양자점, Ag_3PO_4 의 세 성분으로 구성된 시스템에 2.5 eV 보다 작은 에너지의 빛을 조사하였을 때, 로다민 B 가 없었을 경우보다 18 배 높은 광전류가 생성되었다. 이 연구에서의 전자전달 메커니즘은 형광분석을 통해 밝혀졌으며, FRET 과 업컨버젼 현상을 응용한 연구는 향후 가시광-근적외선 영역의 빛을 효과적으로 활용할 수 있는 방안을 제시하였다.

주요어: 태양광 에너지 전환, 광촉매, 나노입자, 가시광선, 전자 전달, 수소

학 번: 2010-24097

List of publications

International Peer-Reviewed Papers

1. H. N. Umh,* **S. Yu**,* Y. H. Kim, S. Y. Lee, J. Yi (*co-first author), "Tuning the Structural Color of a 2D Photonic Crystal using a Bowl-Like Nanostructure", ***Small***, submitted.
2. **S. Yu**, S. Y. Lee, H. N. Umh, J. Yi, "Energy Conversion of Sub-Band-Gap Light using Naked Carbon Nanodots and Rhodamine B", ***ACS Nano***, submitted.
3. **S. Yu**, S. Y. Lee, J. Yeo, J. W. Han, J. Yi, "Kinetic and Mechanistic Insights into the All-Solid-State Z-Schematic System", ***The Journal of Physical Chemistry C***, **2014**, 118(51), 29583−29590.
4. **S. Yu**, Y. H. Kim, S. Y. Lee, H. D. Song, J. Yi, "Hot-Electron-Transfer Enhancement for the Efficient Energy Conversion of Visible Light", ***Angewandte Chemie-International Edition***, **2014**, 53(42), 11203−11207.
5. **S. Yu**, H. J. Yun, Y. H. Kim, J. Yi, "Carbon-Doped TiO_2 Nanoparticles Wrapped with Nanographene as a High Performance Photocatalyst for Phenol Degradation under Visible Light Irradiation", ***Applied Catalysis B: Environmental***, **2014**, 144, 893−899.
6. **S. Yu**, H. J. Yun, D. M. Lee, J. Yi, "Preparation and Characterization of Fe-Doped TiO_2 Nanoparticles as a Support for a High Performance CO Oxidation Catalyst", ***Journal of Materials Chemistry***, **2012**, 22(25), 12629−12635.
7. S. Bae, I. Nam, S. Park, Y. G. Yoo, **S. Yu**, J. M. Lee, J. W. Han, and J. Yi, Interfacial Adsorption and Redox Coupling of $Li_4Ti_5O_{12}$ with Nano-graphene for High-Rate Lithium Storage, ***ACS Applied Materials & Interfaces***, **2015**, 7(30), 16565−16572.

8. M. Lee, H. J. Yun, **S. Yu**, J. Yi, "Enhancement in Photocatalytic Oxygen Evolution via Water Oxidation under Visible Light on Nitrogen-Doped TiO_2 Nanorods with Dominant Reactive {102} Facets", ***Catalysis Communications***, **2014**, 43, 11−15.
9. H. J. Yun, D. M. Lee, **S. Yu**, J. Yoon, H.-J. Park, J. Yi, "Effect of Valence Band Energy on the Photocatalytic Performance of N-Doped TiO_2 for the Production of O_2 via the Oxidation of Water by Visible Light", ***Journal of Molecular Catalysis A: Chemical***, **2013**, 378, 221−226.
10. M. Y. Kang, H. J. Yun, **S. Yu**, W. Kim, N. D. Kim, J. Yi, "Effect of TiO_2 Crystalline Phase on CO Oxidation over CuO Catalysts Supported on TiO_2", ***Journal of Molecular Catalysis A: Chemical***, **2013**, 368−369, 72−77.
11. D. M. Lee, H. J. Yun, **S. Yu**, S. J. Yun, S. Y. Lee, S. H. Kang, J. Yi, "Design of an Efficient Photocatalytic Reactor for the Decomposition of Gaseous Organic Contaminants in Air", ***Chemical Engineering Journal***, **2012**, 187, 203−209.
12. H. J. Yun, H. Lee, N. D. Kim, D. M. Lee, **S. Yu**, J. Yi, "A Combination of Two Visible-Light Responsive Photocatalysts for Achieving the Z-Scheme in the Solid State", ***ACS Nano***, **2011**, 5(5), 4084−4090.

Patent Application

1. J. Yi, **S. Yu**, Y. H. Kim, S. Y. Lee, H. D. Song, "Plasmonic Core-Shell Structure with Three Component System for Visible Light Energy Conversion and Method for Synthesizing Thereof", Korean Patent Application No. 10-2014-0175186 (2014.12.08)

International Conferences

1. **S. Yu**, S. Y. Lee, J. Yi, "Z-Schematic Electron-Transfer Kinetics of the All-Solid-State Photocatalyst Working at Visible Light", 27th International Conference on Photochemistry, Jeju island, Korea, June 28−July 3, 2015 **(Poster & Short Oral Presentation)**
2. **S. Yu**, Y. H. Kim, S. Y. Lee, H. D. Song, H. N. Umh, J. Yi, "Plasmon-Enhanced Solar Energy Conversion to Chemical and Electrical Energy", 248th American Chemical Society National Meeting & Exposition, San Francisco, CA, USA, August 10−14, 2014 **(Poster)**
3. **S. Yu**, Y. H. Kim, E. H. Kim, S. Y. Lee, J. Yi, "Facile Preparation and Characterization of Graphene-Modified Carbon-Doped TiO_2 Nanoparticles for a Highly Visible Light Responsive Photocatalysis", 247th American Chemical Society National Meeting & Exposition, Dallas, TX, USA, March 16−20, 2014 **(Poster)**
4. **S. Yu**, E. H. Kim, S. Y. Lee, Y. H. Kim, J. Yi, "Au Nanocatalyst Supported on the Fe-Doped TiO_2 Particles for High Activity in the CO Oxidation Reaction by a Mars-van Krevelen Mechanism", 2013 MRS Fall Meeting Program & Exhibit, Boston, MA, USA, December 1−6, 2013 **(Poster)**
5. **S. Yu**, E. H. Kim, J. Yeo, J. Yi, "Valence Band Control of N-Doped TiO_2 Nanoparticles and Its Photocatalytic O_2 Evolution", 9th World Congress of Chemical Engineering, Seoul, Korea, August 18−23, 2013 **(Poster)**
6. E. H. Kim, **S. Yu**, J. Yeo, S. Y. Lee, Y. H. Kim, J. Yi, "Analysis of Cocatalyst on Oxidative Characteristics of Visible-Light Responsive Carbon-Doped TiO_2 Photocatalyst", The 14th Japan-Korea Symposium on Catalysis, Nagoya, Japan, July 1−3, 2013 **(Poster)**

7. **S. Yu**, Y. H. Kim, J. Yi, "Preparation and Characterization of Carbon-Doped TiO_2 Nanoparticles Wrapped with Nano-Sized Graphene Working under Visible Light Irradiation", The 6th WCU International Symposium on Chemical Convergence for Energy and Environment, Incheon, Korea, June 17−18, 2013 **(Poster)**
8. H. J. Yun, **S. Yu**, J. Yi, "Photocatalytic Hydrogen Production from Sunlight via Tuning the Band Gaps using Impurities-Doping Techniques", 222nd ECS Meeting 2012 Fall Meeting of The Electrochemical Society of Japan, Honolulu, Hawaii, USA, October 7−12, 2012 **(Oral)**
9. **S. Yu**, H. J. Yun, E. H. Kim, J. Yeo, J. Yi, "Enhancement of Photocatalytic O_2 Evolution on TiO_2 Nanoparticles by Controlling the Valence Band", 19th International Conference on Photochemical Conversion and Storage of Solar Energy, Pasadena, CA, USA, July 29 − August 3, 2012 **(Poster)**
10. H. J. Yun, H. Lee, D. M. Lee, **S. Yu**, J. Yi, "Hydrogen Evolution via Water Splitting on Pt/CdS/Au/$TiO_{1.96}O_{0.04}$", PAC RIM 9, Carins, Australia, July 10−14, 2011 **(Poster)**
11. H. J. Yun, H. Lee, N. D. Kim, M. Lee, **S. Yu**, J. Baek, Y. Choi, J. Yi, "Facile Adjustment of Doping Level in Carbon Doped TiO_2 Nanoparticle", 218th ECS Meeting, Las Vegas, NV, USA, October 10−15, 2010 **(Oral)**
12. H. J. Yun, H. Lee, N. D. Kim, M. Lee, **S. Yu**, J. Yi, "Preparation and Characterization of $TiO_{2-x}C_x$ Nanoparticle for the High Performance Photo-Catalyst", IPS-18, Seoul, Korea, July 25−30, 2010 **(Poster)**

Domestic Conferences

1. **유성주**, 이수영, 김용화, 엄하늬, 이종협, “물로부터 청정연료 수소생산을 위한 광촉매의 반응기작”, 2015 년 한국청정기술학회 춘계 학술발표회, 부여 롯데리조트, 3. 26–27 (2015) **(포스터)**
2. **유성주**, 김용화, 이수영, 엄하늬, 이종협, “물로부터 수소와 전기 생산을 위한 청정기술 개발”, 2015 년 한국청정기술학회 춘계 학술발표회, 부여 롯데리조트, 3. 26–27 (2015) **(포스터)**
3. **유성주**, 김용화, 이수영, 박수민, 유영근, 박종석, 이종협, “플라즈몬 유도 열전자를 이용한 효율적 태양광 에너지 전환”, 한국화학공학회 2014 년도 가을 총회 및 학술대회, 대전컨벤션센터, 10. 23-24 (2014) **(구두)**
4. 이수영, **유성주**, 엄하늬, 남인호, 배성준, 한정우, 이종협, “인공광합성 시스템하에서의 전하 이동 및 표면 반응 메커니즘”, 한국화학공학회 2014 년도 가을 총회 및 학술대회, 대전컨벤션센터, 10. 23-24 (2014) **(포스터)**
5. **유성주**, 김용화, 이수영, 송현돈, 이종협, “가시광의 효율적 에너지 전환을 위한 플라즈모닉 코어-쉘 나노구조체”, 2014 년 한국청정기술학회 춘계 학술발표회, 여수경도리조트, 3. 27-28 (2014) **(포스터)**
6. 김경학, **유성주**, 이종협, 한정우, “Density Functional Theory Study for the Evaluation of M-doped TiO_2(101) (M=Cr, Mn, Fe, Co and Ni) over CO Oxidation”, 한국화학공학회 2013 년도 가을 총회 및 학술대회, 대구 EXCO, 10. 23-25 (2013) **(포스터)**
7. **유성주**, 김용화, 김혜선, 이수영, 이종협, “그래핀/탄소도핑 TiO_2 나노복합체 합성 및 이를 이용한 페놀분해”, 한국화학공학회 2013 년도 가을 총회 및 학술대회, 대구 EXCO, 10. 23-25 (2013) **(구두) (포스터)**

8. **유성주**, 이민재, 김혜선, 이수영, 김용화, 이종협, “물 산화반응에 적합한 표면구조의 질소도핑 TiO_2 나노입자 개발”, 2013 년 한국청정기술학회 추계 학술발표회, 제주 한화리조트, 9. 25-27 (2013) **(포스터)**
9. **유성주**, 김혜선, 여정은, 이수영, 김용화, 이종협, “TiO_2 나노입자의 가전자대 위치에 따른 물 산화반응”, 한국화학공학회 2013 년 봄 총회 및 학술대회, 광주 김대중컨벤션센터, 4. 24-26 (2013) **(포스터)**
10. 김혜선, **유성주**, 여정은, 이수영, 김용화, 이종협, “C-TiO_2 가시광 광촉매의 조촉매에 따른 산화특성분석”, 한국화학공학회 2013 년 봄 총회 및 학술대회, 광주 김대중컨벤션센터, 4. 24-26 (2013) **(포스터)**
11. 여정은, 이수영, **유성주**, 김혜선, 김용화, 이종협, “광촉매 내 전자이동 경로의 모델링 및 형광분석을 통한 정량화”, 2013 년 한국청정기술학회 춘계 학술발표회, 여수 경도리조트, 3. 28-29 (2013) **(포스터)**
12. **유성주**, 김혜선, 여정은, 이수영, 김용화, 이종협, “일산화탄소 산화반응의 담체로서 철 도핑 이산화티탄의 도핑 수준에 따른 영향”, 2013 년 한국청정기술학회 춘계 학술발표회, 여수 경도리조트, 3. 28-29 (2013) **(포스터)**
13. **유성주**, 윤형진, 이종협, “저온에서의 일산화탄소 저감을 위한 고성능 산화반응 촉매 개발”, 춘계 한국청정기술학회, 연세대학교, 5.25 (2012) **(포스터)**
14. 이민재, 윤형진, **유성주**, 여정은, 이종협, “질소도핑 TiO_2 가시광 광촉매의 도핑수준이 물산화 반응의 성능에 미치는 영향”, 추계 한국화학공학회, 송도컨벤시아, 10. 26-28 (2011) **(포스터)**
15. **유성주**, 윤형진, 이민재, 이종협, “철 도핑 TiO_2 를 이용한 금 나노촉매의 일산화탄소 산화반응”, 추계 한국화학공학회, 송도컨벤시아, 10. 26-28 (2011) **(포스터)**

16. **유성주**, 윤형진, 이민재, 이종협, “고분자전해질 연료전지의 피독현상 방지를 위한 고성능 일산화탄소 산화촉매 개발”, 추계 한국에너지공학회, 서울대학교 교수회관, 10. 20-21 (2011) **(포스터)**
17. 윤형진, 김남동, 이민재, **유성주**, 여정은, 이종협, “고체 상에서의 Z-Scheme 구현을 통한 물분해 수소생산”, 추계 한국에너지공학회, 서울대학교 교수회관, 10. 20-21 (2011) **(포스터)**
18. 이민재, 윤형진, 이현주, 김남동, **유성주**, 이종협, “Hydrogen Evolution via Water-Splitting by Artificial Z-scheme Photocatalyst under the Irradiation of Visible Light”, The 18th Annual Meeting for Korean Society of Photoscience, 서강대학교, 6. 9-10 (2011) **(포스터)**
19. **유성주**, 윤형진, 이민재, 이종협, “일산화탄소의 산화반응을 위한 Au/Fe-TiO_2 촉매의 제조 및 분석”, 춘계화학공학회,창원컨벤션센터, 4. 27-29 (2011) **(구두)**
20. 윤형진, 이현주, 김남동, 이민재, **유성주**, 이종협, “나노물질기반의 물분해 수소생산을 위한 인공광합성 구현”, 춘계화학공학회, 창원컨벤션센터, 4. 27-29 (2011) **(구두)**
21. 윤형진, 이민재, **유성주**, 백자연, 최영보, 이종협, “다양한 형태의 TiO_2 나노입자 제조 및 광촉매 특성 변화”, 추계한국청정기술학회, 충남대학교, 11. 19 (2010) **(포스터)**
22. 이민재, 윤형진, 이선용, **유성주**, 강상현, 윤성진, 이종협, “UV/TiO_2 광촉매 시스템을 이용한 DMS 기상분해반응”, 추계화학공학회, 대전 컨벤션센터, 10. 20-22 (2010) **(포스터)**
23. 강미영, 윤형진, **유성주**, 이종협, “일산화탄소 선택적 산화반응을 위한 산화구리-타이타니아 촉매의 제조와 분석”, 추계한국에너지공학회, 전북대학교, 10. 13-14 (2010) **(구두)**

24. 강미영, 윤형진, **유성주**, 이종협, “타이타니아에 담지된 산화구리 촉매의 일산화탄소 산화반응 적용”, 춘계화학공학회, 대구 EXCO, 4. 21-23 (2010) **(포스터)**